Higgs Decay into Dark Matter in the CxSM at Next-to-Leading Order

Master's Thesis of

Felix Egle

at the Department of Physics
Institute for Theoretical Physics (ITP)

Reviewer:	Prof. Dr. M. M. Mühlleitner (KIT, Karlsruhe)
Second reviewer:	Prof. Dr. R. Santos (ISEL & U. LISBOA, Lisbon)

02. November 2020 – 04. October 2021

I declare that I have developed and written the enclosed thesis completely by myself, and have not used sources or means without declaration in the text.

Karlsruhe, 04.10.2021

. . . .
(Felix Egle)

Accepted as Master thesis.

Karlsruhe, 04.10.2021

. . . .
(Prof. Dr. M. M. Mühlleitner)

Contents

List of Figures

List of Tables

1. Introduction

The fundamental description of nature in which the scientific field of particle physics plays an essential role, had tremendous success in the 20th century both in theoretical and experimental aspects. The interplay between theory and experiment, especially, played an important part in the achievements of particle physics and is one of the core beauties of it. On one side, there are theoretical models based on mathematical principles and experimental observations, which not only can reproduce the experimental results, but can make new predictions as well. And on the other side stand the experimental observations, which by chance, by experimental ingenuity or by searching for theoretical predictions actually observe new physics phenomena. As an example: With the introduction of the Dirac equation [1] not only relativistic electrons could be described, but also predictions in the form of new particles could be made. The equation allows for a positive electron-like particle with negative energy [2]. Later, this so-called *positron* was actually discovered as the anti-particle of the electron [3].

Moreover, the interplay between theoretical models and experimental observations becomes even more subtle with the occurrence of divergences in higher-order calculations in perturbative quantum field theory and their proper treatment. Divergent parts in a physical theory are not an exclusive feat of quantum field theories. They can be found in many theories and hint at the fact that the theoretical model lacks some fundamental aspect of nature, since divergences cannot occur in observables. The methods to properly treat these divergent parts in quantum field theories are regularization and renormalization [4, 5], which in turn need experimentally measured results as an input. Therefore, theoretical models in particle physics rely on experimental results in order to make precision calculations and the methods to correctly regularize and renormalize a theory are crucial.

With this in mind, one of the key achievements in the 20th century in particle physics was the development of the Standard Model (SM) [6–8]. With the combination of experimental observations and theoretical developements step by step all known elementary particles and forces of nature (except for gravity) could be included. However, one of the key pieces of the SM was not discovered in the 20th century, although it was already proposed in the 1960s: the Higgs boson [9–13]. With the discovery of the $125\,\mathrm{GeV}$ Higgs boson at the Large Hadron Collider (LHC) in 2012 [14, 15], the SM was finally completed from the theoretical point of view. All particles that where predicted by the SM had been found.

Nevertheless, the search for new particles is far from being over and new theories beyond the SM (BSM) are developed to explain so far unanswered questions. To mention two of them, first of all cosmological observations clearly indicate the existence of so-called Dark Matter (DM) in the universe, e.g. [16], which might consist of a new type of particle. In the

SM, however, no suitable candidate can be found. Furthermore, the observable universe possesses a matter-antimatter asymmetry, which has origins in the early universe. The three Sakharov conditions [17] would offer through electroweak (EW) baryogenesis a dynamical solution for this asymmetry. The SM is, in principle, able to fulfill all conditions, but a Higgs boson mass of about 70-80 GeV [18, 19] would be required for the EW phase transition to be of strong first order [20–22], in contrast to the discovery of the 125 GeV Higgs boson, and the CP violation within the SM arising from the Cabibbo-Kobayashi-Maskawa (CKM) matrix is not large enough [23–25]. A possible approach for a BSM theory is to extend the Higgs sector of the SM. The scalar potential of the SM has not been fully measured yet and there is still room for physics beyond the SM. These models introduce new scalar particles, which can be a suitable DM candidate.

The Complex Singlet Extension of the Standard Model (CxSM) [26–39] is one of the many theories which extend the scalar sector of the SM and is able to provide a suitable DM candidate. It is especially interesting, since it is quite simple in its extension. The model only adds, as the name suggests, a complex singlet field to the scalar sector of the SM. Therefore, only the scalar sector receives a significant change with respect to the SM. Within the CxSM, theoretical calculations can be perfomed and compared with experimental results. At the Large Hadron Collider (LHC), the decay of the 125 GeV Higgs boson into invisible particles can be probed for, and there already exist experimental limits [40]. The upcoming LHC run [41] might further improve on this. Thus, from a theoretical point of view it is desirable to perform precision calculations in order to be able to compete with experimental results and further constrain the parameters of the model. In the CxSM, for example, the decay of the 125 GeV Higgs boson into DM particles can be computed at higher order to obtain precise results and to compare them with the aforementioned current and future experimental data. In this thesis the next-to-leading order (NLO) EW corrections to this process will be calculated, and their impact will be analyzed and discussed in detail.

The structure of the thesis is as follows. To start with, an introduction to the CxSM, as well as the key differences to the SM are given in Chapter 2. In addition to the choice of input parameters (Sec. 2.4), the constraints on the model from theoretical requirements and experimental observations are discussed (Sec. 2.5).

Next, the description of the renormalization of the CxSM is presented in Chapter 3. The important parts in renormalizing the model with respect to the later calculated decay process as well as detailed discussions of several renormalization schemes for the different input parameters are presented.

Subsequently, in Chapter 4, the computational tools applied in the calculation of the NLO decay width of the 125 GeV Higgs boson decay into dark matter particles is presented. Furthermore, technical details of the calculation and analytical tests of the result are presented. Next, the numerical analysis with the generated input parameters, that obey the aforementioned theoretical and experimental constraints, is shown in Chapter 5. In particular, the results are presented and discussed in detail.

Finally, the conclusion of the thesis and an outlook on possible further future work is given in Chapter 6.

2. Introduction to the CxSM

In this Chapter an introduction to the CxSM is presented. As already mentioned in the Introduction, the CxSM is a simple extension of the SM, by expanding the scalar sector. The version of the CxSM discussed in this thesis is able to provided a possible DM candidate. Thus, a description of the expanded scalar sector is given (Sec. 2.2). The choice of input parameters is discussed (Sec. 2.4) and theoretical and experimental constraints on the model are presented 2.5.

2.1. The CxSM Lagrangian

In the CxSM the scalar sector is extended beyond the SM by introducing an additional complex singlet $\mathbb{S}$. The singlet does not couple to any gauge bosons and fermions and therefore only changes the scalar sector of the SM Lagrangian. The complete Lagrangian reads

$$\mathcal{L}_{\mathrm{CxSM}} = \mathcal{L}_{\mathrm{YM}} + \mathcal{L}_{\mathrm{F}} + \mathcal{L}_{\mathrm{S}} + \mathcal{L}_{\mathrm{Yuk}} + \mathcal{L}_{\mathrm{GF}} + \mathcal{L}_{\mathrm{FP}}. \tag{2.1}$$

The Yang-Mills Lagrangian $\mathcal{L}_{\mathrm{YM}}$, the fermion Lagrangian $\mathcal{L}_{\mathrm{F}}$, the gauge fixing Lagrangian $\mathcal{L}_{\mathrm{GF}}$ as well as the Fadeev-Popov Lagrangian $\mathcal{L}_{\mathrm{FP}}$ are unchanged with respect to the SM and can be found in the literature, e.g. in Refs. [42, 43]. The third term, $\mathcal{L}_{\mathrm{S}}$, encapsulates the scalar sector of the theory, which is different with respect to the SM and is described in detail in Sec. 2.2. The part $\mathcal{L}_{\mathrm{Yuk}}$ describes the couplings of the fermions to the Higgs boson and can, in general, be different with respect to the SM. In the CxSM, however, this is not the case, as can be seen in Sec. 2.3.

2.2. The Scalar Sector

With the additional singlet $\mathbb{S}$ the scalar potential potential now contains more possible terms. To constrain this potential, a global $U(1)$ symmetry is imposed on $\mathbb{S}$ which is softly broken. The most general renormalizable scalar potential thus reads

$$\begin{aligned} V_{\mathrm{scalar}} = \frac{m^2}{2}\Phi^\dagger\Phi + \frac{\lambda}{4}\left(\Phi^\dagger\Phi\right)^2 + \frac{\delta_2}{2}\Phi^\dagger\Phi|\mathbb{S}|^2 + \frac{b_2}{2}|\mathbb{S}|^2 + \frac{d_2}{4}|\mathbb{S}|^4 \\ + \left(\frac{b_1}{4}\mathbb{S}^2 + a_1\mathbb{S} + c.c.\right), \end{aligned} \tag{2.2}$$

where Φ denotes the doublet field. The soft breaking terms proportional to the couplings b_1 and a_1 are in parentheses. All parameters are, in general, real except for b_1 and a_1. The two fields can be written as

$$\Phi = \begin{pmatrix} G^+ \\ \frac{1}{\sqrt{2}}\left(v + H + iG^0\right) \end{pmatrix}, \quad \mathbb{S} = \frac{1}{\sqrt{2}}(v_S + S + i(v_A + A)), \tag{2.3}$$

where H, S and A are real scalar fields. The G^+ and G^0 fields will form the respective Goldstone bosons for the Z and W^+ bosons similarly as in the SM. The v, v_A and v_S are the vacuum expectation values (vevs) of the corresponding fields and can all be, in general, non-zero which in turn can lead to mixing between all three scalar fields,

$$\begin{pmatrix} h_1 \\ h_2 \\ h_3 \end{pmatrix} = R \begin{pmatrix} H \\ S \\ A \end{pmatrix}, \tag{2.4}$$

with a general rotation matrix R.

This description is still a quite general formulation for the CxSM. In this thesis, a special case was considered by demanding that the real part S and the imaginary part A of the singlet field obey a $\mathbb{Z}_2$ symmetry separately. So the potential has to be invariant under the transformations $S \longrightarrow -S$ and $A \longrightarrow -A$. From this it immediately follows that $a_1 = 0$ and $b_1 \in \mathbb{R}$. Furthermore, without loss of generality, one of the vevs can be chosen to be zero. Here, v_A is be chosen to be zero whereas v_S is non-zero. This means that the scalar field A will obey the $\mathbb{Z}_2$ symmetry, whereas for S the symmetry will be spontaneously broken. Thus, the particle associated with the field A is stable since a decay into particles that do not transform under this symmetry would break it.

With the broken symmetry, S can now mix with H. Thus, the mass eigenstates h_i $(i = 1, 2)$ relate to the gauge eigenstates H and S through

$$\begin{pmatrix} h_1 \\ h_2 \end{pmatrix} = R_\alpha \begin{pmatrix} H \\ S \end{pmatrix}, \tag{2.5}$$

where the rotation matrix is given by

$$R_\alpha = \begin{pmatrix} \cos(\alpha) & \sin(\alpha) \\ -\sin(\alpha) & \cos(\alpha) \end{pmatrix} = \begin{pmatrix} c_\alpha & s_\alpha \\ -s_\alpha & c_\alpha \end{pmatrix}, \tag{2.6}$$

with the abbreviations c_α and s_α for $\cos(\alpha)$ and $\sin(\alpha)$ respectively. The mass matrix for the gauge eigenstates is given by

$$\mathcal{M} = \begin{pmatrix} \frac{v^2\lambda}{2} & \frac{\delta_2 v v_S}{2} \\ \frac{\delta_2 v v_S}{2} & \frac{d_2 v_S^2}{2} \end{pmatrix} + \begin{pmatrix} \frac{T_1}{v} & 0 \\ 0 & \frac{T_2}{v_S} \end{pmatrix}, \tag{2.7}$$

with the tadpole parameters T_1 and T_2. They are defined trough the minimization conditions as

$$\left.\frac{\partial V}{\partial v}\right| \equiv T_1 \;\Rightarrow\; \frac{T_1}{v} = \frac{m^2}{2} + \frac{\delta_2 v_S^2}{4} + \frac{v^2\lambda}{4}, \tag{2.8a}$$

$$\frac{\partial V}{\partial v_S} \equiv T_2 \;\Rightarrow\; \frac{T_2}{v_S} = \frac{b_1 + b_2}{2} + \frac{\delta_2 v^2}{4} + \frac{v_S^2 d_2}{4}, \tag{2.8b}$$

where the expressions in Eq. (2.3) have been inserted into the potential. The mass term for the field A is given by

$$\mathcal{M}_A = \frac{-b_1 + b_2}{2} + \frac{\delta_2 v^2}{4} + \frac{v_S^2 d_2}{4} = -b_1 + \frac{T_2}{v_S}, \tag{2.9}$$

At tree level, the tadpole parameters T_i ($i = 1, 2$) have to be zero to fulfill the minimum conditions. These equations can then be used to express the remaining parameters by the chosen set of input parameters, see also Sec. 2.4.

The minimization conditions can have multiple solutions for possible vev parameters. The desired minimum state that is investigated in this thesis is the configuration with both vevs v and v_S to be non-zero, however there might be other possibilities as well. A detailed discussion on these potential minima will be given in Sec. 2.5.1.

With the rotation matrix R_α the mass matrix can be diagonalized,

$$D^2_{hh} \equiv R_\alpha \mathcal{M} R^T_\alpha. \tag{2.10}$$

The field A is already given in mass basis, thus the mass term reads

$$D^2_A \equiv \mathcal{M}_A. \tag{2.11}$$

The diagonal entries of the mass matrix D^2_{hh} and the mass term D^2_A can be interpreted as the physical masses of the corresponding fields, i.e.

$$D^2_{hh} = diag(m^2_{h_1}, m^2_{h_2}),\ D^2_A = m^2_A. \tag{2.12}$$

With the scalar fields described, the overall scalar Lagrangian reads

$$\mathcal{L}_{\mathrm{S}} = \left(D_\mu \Phi\right)^\dagger (D^\mu \Phi) + \partial_\mu \mathbb{S}^* \partial^\mu \mathbb{S} - V_{\mathrm{Scalar}}, \tag{2.13}$$

where D_μ is the covariant derivative [42, 43],

$$D_\mu = \partial_\mu + ig\frac{\sigma^a}{2} W^a_\mu(x) + ig'\frac{Y}{2} B_\mu(x). \tag{2.14}$$

Since $\mathbb{S}$ is a singlet it does not couple to any gauge bosons and therefore only the partial derivative enters into the Lagrangian, whereas the doublet Φ couples to both the $SU(2)_L$ and $U(1)_Y$ gauge bosons of the SM, with the corresponding coupling constants g and g', the hypercharge Y and the Pauli matrices σ^a ($a = 1, 2, 3$). The W^a_μ and B_μ are the gauge fields of the $SU(2)_L$ and $U(1)_Y$ symmetries, respectively. The doublet structure of the CxSM is identical to the doublet structure of the SM,which means that all relations between the doublet vev v and the gauge boson masses m_W and m_Z remain be unchanged and the photon is still massless.

The couplings of the gauge bosons to the scalar particles change, since the gauge eigenstates have to be rotated to the mass eigenstates. Therefore the CxSM couplings read

$$g_{h_i VV} = g_{H_{\mathrm{SM}} VV} k_i, \quad k_i \equiv \begin{cases} \cos(\alpha), i = 1 \\ -\sin(\alpha), i = 2 \end{cases}, \tag{2.15}$$

where $g_{H_{\mathrm{SM}} VV}$ denotes the SM coupling between the SM Higgs and the massive gauge bosons V ($V = Z, W^\pm$).

2.3. The Yukawa Sector

When introducing additional scalar fields in the SM, the Yukawa Sector can, in general, be altered with respect to the SM. But since in the CxSM only a singlet field is added, which does not couple to the SM particles, the Yukawa sector remains unchanged. Thus the Lagrangian reads

$$\mathcal{L}_{\text{Yuk}} = -\bar{L}_L Y_l \Phi l_R - \bar{Q}_L^{'} Y_d \Phi d_R^{'} - \bar{Q}_L^{'} Y_u \tilde{\Phi} u_R^{'} + \text{h.c.}\,, \tag{2.16}$$

with the left-handed lepton and quark doublets L_L and $Q_L^{'}$ and the general complex 3×3 matrices Y_l, Y_d and Y_u. Here a sum over the generations is implied and

$$\tilde{\Phi} \equiv i\sigma_2 \Phi^*, \tag{2.17}$$

with σ_2 being the second Pauli matrix. To transform the quarks into the mass basis a unitary transformation has to be applied, which eventually leads to the CKM matrix that is already known in the SM (for more details see for example [43]).

The major change with respect to the SM is again similar to the gauge boson part. The couplings receive an additional angular factor from the rotation of the scalar gauge fields into the mass eigenstates. Thus, the couplings between the scalar particles h_i and fermions f reads

$$g_{h_i f\bar{f}} = g_{H_{\text{SM}} f\bar{f}} k_i, \tag{2.18}$$

where $g_{H_{\text{SM}} f\bar{f}}$ denotes the SM coupling between the SM Higgs and the fermions f.

2.4. Choice of Input Parameters

With the introduction of the additional singlet in the CxSM, the scalar potential (Eq. (2.2)) has 8 parameters among which 2 are vevs. However, it is more convenient to use the scalar masses and the scalar mixing angle as inputs. They can be related to the original parameters of the potential by using Eqs. (2.8), (2.10) and (2.11). In total these are 6 equations: 2 minimization conditions, 1 equation from the mass term D_A and 3 equations from the rotation of the mass matrix D_{hh}^2. Thus, all potential parameters except for the vevs can be expressed through scalar masses and the scalar mixing angle. The input parameters read

$$\{v, v_S, \alpha, m_{h_1}, m_{h_2}, m_A, T_1, T_2\}. \tag{2.19}$$

The tadpole parameters T_i are zero at tree level, but they will be important later when the renormalization of the NLO calculation is discussed (see Sec. 3.2).

The other potential parameters can be expressed as

$$\lambda = \frac{m_{h_1}^2 + m_{h_2}^2 + \cos(2\alpha)(m_{h_1}^2 - m_{h_2}^2)}{v^2}, \tag{2.20a}$$

$$d_2 = \frac{m_{h_1}^2 + m_{h_2}^2 + \cos(2\alpha)(m_{h_2}^2 - m_{h_1}^2)}{v_S^2}, \tag{2.20b}$$

$$\delta_2 = \frac{(m_{h_1}^2 - m_{h_2}^2)\sin(2\alpha)}{v v_S}, \tag{2.20c}$$

$$m^2 = \frac{1}{2}\left(\cos(2\alpha)(m_{h_2}^2 - m_{h_1}^2) - \frac{v(m_{h_1}^2 + m_{h_2}^2) + v_S(m_{h_1}^2 - m_{h_2}^2)\sin(2\alpha)}{v}\right), \tag{2.20d}$$

$$b_2 = \frac{1}{2}\left(2m_A^2 - m_{h_1}^2 - m_{h_2}^2 + \cos(2\alpha)(m_{h_1}^2 - m_{h_2}^2) - \frac{v(m_{h_1}^2 - m_{h_2}^2)\sin(2\alpha)}{v_S}\right), \tag{2.20e}$$

$$b_1 = -m_A^2 . \tag{2.20f}$$

In the EW sector of the SM the masses of the gauge bosons and fermions, as well as the electric charge e, can be chosen as input parameters. Further useful relations, which are used in the upcoming calculations, are

$$s_\mathrm{w} \equiv \sin(\Theta_\mathrm{W}),\ c_\mathrm{w} \equiv \cos(\Theta_\mathrm{W}) = \frac{m_W}{m_Z}, \tag{2.21a}$$

$$g' = \frac{e}{c_\mathrm{w}}, \tag{2.21b}$$

$$g = \frac{e}{s_\mathrm{w}}, \tag{2.21c}$$

$$v = \frac{2m_W}{g}, \tag{2.21d}$$

where Θ_W is the weak mixing angle.

2.5. Constraints

In order to investigate the validity of the model, relevant theoretical and experimental constraints have to be considered. Some of them are already fulfilled by the structure of the CxSM, whereas other constraints will give tight limits on certain parameters of the model. The discussion of these constraints here follows earlier works, cf. Refs. [37–39, 44]. All of the described constraints are already implemented in ScannerS [37, 39, 44] which will be used in order to generate viable parameter points that are not yet excluded by theoretical and experimental constraints (see Sec. 5.2).

2.5.1. Theoretical Constraints

The following theoretical constraints have to be taken into account:

- **Boundedness from below**

  The scalar potential has to be bounded from below in order to have a stable minimum around which perturbation theory can be applied. In the SM this is already achieved by requiring that the quartic term of the potential is positive. In the CxSM this is more complicated.

  For the potential to be bounded from below it is sufficient to look at the quartic terms. The replacements $\Phi^\dagger\Phi \equiv x$ and $|\mathbb{S}|^2 \equiv y$ can be made to look at all possible field directions. Now the simplified potential reads

  $$V_{\text{quartic}}(x, y) = \frac{\lambda}{4}x^2 + \frac{\delta_2}{2}xy + \frac{d_2}{4}y^2 = \frac{1}{4}\begin{pmatrix} x & y \end{pmatrix}^{\mathrm{T}} \begin{pmatrix} \lambda & \delta_2 \\ \delta_2 & d_2 \end{pmatrix} \begin{pmatrix} x \\ y \end{pmatrix}. \tag{2.22}$$

  Since x and y are by definition positive, the matrix describing the quartic potential has to be co-positive in order for the potential to be bounded from below [45]. This means that the diagonal elements as well as the determinant have to be positive if the off-diagonal elements are negative and leads to the constraints (at tree level)

  $$\lambda > 0 \wedge d_2 > 0 \wedge (\delta_2^2 < \lambda d_2 \text{ if } \delta_2 < 0). \tag{2.23}$$

  The same result was also obtained in [37].

- **Unitarity constraints**
  As in the SM, the couplings of the CxSM have to satisfy certain relations in order to obey unitarity [46]. In the SM, the processes $V_L V_L \to V_L V_L$ and $f_+ \bar{f}_+ \to V_L V_L$ do not break unitarity at tree level because of the unique coupling of the SM Higgs with the respective particles. Now in the CxSM this also has to be the case.

  As described in the Secs. 2.2 and 2.3 the couplings of the scalar fields to fermions and gauge bosons are such that the relations

  $$\sum_{i=1}^{2} g_{h_i VV}^2 = g_{H_{\text{SM}}VV}^2, \tag{2.24}$$

  $$\sum_{i=1}^{2} g_{h_i VV} g_{h_i f\bar{f}} = g_{H_{\text{SM}}VV} g_{H_{\text{SM}}f\bar{f}}, \tag{2.25}$$

  hold, and the above mentioned processes do not violate unitarity [47].

  Furthermore, the quartic interactions between scalar particles can be used to obtain constraints on the parameters of the potential, as was already described by Lee, Quigg and Thacker for the SM in [48]. These interactions also have to obey unitarity. In the high-energy limit they are proportional to the quartic terms of the potential and the scattering matrix $\mathcal{M}_{2\to 2}$ of all possible two-to-two scalar scattering interactions can be calculated. In order for unitarity to hold, the eigenvalues of this matrix are not allowed to exceed a certain value. Thus, the eigenvalues λ_i have to obey

$$|\lambda_i| < 8\pi. \tag{2.26}$$

This leads to the constraints (cf. Ref [44])

$$\begin{gathered}|\lambda| \leq 16\pi \wedge |d_2| \leq 16\pi \wedge |\delta_2| \leq 16\pi \\ \wedge \left|\frac{3}{2}\lambda + d_2 \pm \sqrt{\left(\frac{3}{2}\lambda - d_2\right)^2 + 2\delta_2^2}\right| \leq 16\pi.\end{gathered} \tag{2.27}$$

- **Stability of the Vacuum**
  In the SM the scalar potential [42] is given by

  $$V_{\mathrm{SM}} = \frac{m^2}{2}\Phi^\dagger\Phi + \frac{\lambda}{4}\left(\Phi^\dagger\Phi\right)^2, \tag{2.28}$$

  with the same parametrization of Φ as in Eq. (2.3). The potential has two extreme values for the vev v, of the Higgs field H: $v = 0$ or $v = \sqrt{\frac{-m^2}{\lambda}}$. In order for the non-zero value to be a stable minimum, λ has to be positive and m^2 negative. With these conditions, the stability of the vacuum at tree level is already assured since no other possible minima exist. The calculated minimum will always be the global minimum.

  In the CxSM the scalar potential is more complex and potentially allows for different minima to exist simultaneously, which in turn could lead to an unstable vacuum state. If the current state is not the global minimum, tunneling may lead to the decay of the vacuum into a deeper minimum which should be avoided. More generally, a tunneling process with a lifetime of the age of the universe would still be allowed. For more details see [49]. In the following, a detailed description of the minima of the CxSM at tree level is given.

  Using the general description

  $$\Phi = \frac{1}{\sqrt{2}}\begin{pmatrix} G_1 + iG_2 \\ H + iG_0 \end{pmatrix}, \quad \mathbb{S} = \frac{1}{\sqrt{2}}\left(S + A\right), \tag{2.29}$$

  the minimization conditions read

  $$\left.\frac{\partial V}{\partial \vec{\phi}}\right|_{\langle\phi_i\rangle = x_i} = 0 \Rightarrow \begin{pmatrix} \frac{m^2}{2}x_H + \frac{\lambda}{4}x_H^3 + \frac{\delta_2}{4}x_H x_S^2 = 0 \\ \frac{b_1+b_2}{2}x_S + \frac{d_2}{4}x_S^3 + \frac{\delta_2}{4}x_S x_H^2 = 0 \\ 0 = 0 \\ 0 = 0 \\ 0 = 0 \\ 0 = 0 \end{pmatrix}, \tag{2.30}$$

with the scalar fields collected in the vector

$$\vec{\phi} = \begin{pmatrix} H & S & A & G_0 & G_1 & G_2 \end{pmatrix}^{\mathrm{T}}, \tag{2.31}$$

and only allowing for non-zero vevs x_H and x_S for the fields H and S. Here, in general, the vev parameters are called x_H and x_S to keep them separate from the input values v and v_S.

The two nontrivial equations lead to 4 possible cases for the vevs:

- $x_H = x_S = 0$:
  This trivially solves the equations and the potential at this point results in

  $$V(0,0) = 0. \tag{2.32}$$

- $x_H = 0,\ x_S \neq 0$:
  This trivially solves the first equation and, since $d_2 \neq 0$, the second equation can be solved for x_S and results in

  $$x_S = \sqrt{\frac{-2(b_1 + b_2)}{d_2}} \equiv x_1, \tag{2.33}$$

  if $b_1 + b_2$ is negative. Inserting this into the potential gives

  $$V(0, x_1) = -\frac{(b_1 + b_2)^2}{4d_2}. \tag{2.34}$$

- $x_H \neq 0,\ x_S = 0$:
  This trivially solves the second equation and, since $\lambda \neq 0$, the first equation can be solved for x_H and results in

  $$x_H = \sqrt{\frac{-2m^2}{\lambda}} \equiv x_2, \tag{2.35}$$

  if m^2 is negative. Inserting this into the potential gives

  $$V(x_2, 0) = -\frac{m^4}{4\lambda}. \tag{2.36}$$

- $x_H = v,\ x_S = v_S$:
  From the above equations it can be seen that only one unique solution is possible. Since both vevs are treated as input values, the minimization conditions can be used to be solved for other parameters. This results in

  $$m^2 = \frac{-1}{2}\left(\lambda v^2 + \delta_2 v_S^2\right),\ b_1 + b_2 = \frac{-1}{2}\left(d_2 v_S^2 + \delta_2 v^2\right). \tag{2.37}$$

  The potential with these input parameters reads

  $$V(v, v_S) = \frac{1}{16}\left(4m^2v^2 + \lambda v^4 + 2\delta_2 v^2 v_S^2 + 4(b_1 + b_2)v_S^2 + d_2 v_S^4\right). \tag{2.38}$$

In this thesis, the minimum with both vevs non-zero is the desired ground state and should be the global minimum. This means that Eq. (2.37) has to hold. Moreover, in order for this vev configuration to be a minimum, the Hesse matrix of the potential has to be positive definite, i.e. the determinant has to be positive. This matrix is identical to the mass matrix in Eq. (2.7). Therefore, the requirement reads

$$\delta_2^2 < \lambda d_2. \tag{2.39}$$

With Eq. (2.37) the values of the potential for the different vev configurations can be simplified and compared. The differences are

$$V(v, v_S) - V(0,0) = -\frac{1}{16}\left(\lambda v^4 + \delta_2 v^2 v_S^2 + d_2 v_S^4\right) < 0, \tag{2.40a}$$

$$V(v, v_S) - V(0,x_1) = -\frac{(d_2\lambda - \delta_2^2)v^4}{16 d_2} < 0, \tag{2.40b}$$

$$V(v, v_S) - V(x_2,0) = -\frac{(d_2\lambda - \delta_2^2)v_S^4}{16 \lambda} < 0. \tag{2.40c}$$

All these inequalities hold because of the requirement (2.39). The parameters λ and d_2 have to be positive for the potential to be bounded from below. Thus, if the vev configuration with only non-zero values is a minimum, then it is a unique and global minimum. The only requirement that needs to be fulfilled is relation (2.39).

2.5.2. Experimental Constraints

The following experimental constraints have to be taken into account:

- **The ρ parameter**
  The ρ parameter has been precisely measured [50] to be close to 1. In the SM the identity

  $$\rho = \frac{m_W^2}{m_Z^2 c_\mathrm{W}^2} = 1, \tag{2.41}$$

  holds at tree level [51], with m_W and m_Z being the Z and W boson mass, respectively, and c_W the cosine of the weak mixing angle.

  In models with extended scalar sectors, this relation can be generalized [46]. With n scalar multiplets in the theory the following identity holds,

  $$\rho = \frac{\sum_{i=1}^n \left(I_i(I_i+1) - \frac{1}{4}Y_i^2\right) v_i}{\sum_{i=1}^n \frac{1}{2} Y_i^2 v_i}, \tag{2.42}$$

  with the isospins I_i and hypercharges Y_i of the scalar fields ϕ_i. $SU(2)$ singlets do not contribute to this relation since their hypercharge and isospin are zero. For $SU(2)$ doublets also the relation

  $$I_i(I_i+1) = \frac{1}{2}Y_i^2, \tag{2.43}$$

holds so that the ρ parameter is 1 at tree level. Therefore this constraint is automatically fulfilled when introducing additional singlets or doublets into the SM.

- **No flavor changing neutral currents (FCNC)**
  FCNC are tightly constrained by experimental results [52, 53] and therefore give tight restrictions to extensions of the SM. These constraints also have to be met by the CxSM. However, the CxSM is also a flavor conserving model at tree level since the Yukawa sector is unchanged with respect to the SM and FCNC do not occur in the SM at tree level [54].

The following experimental constraints are implemented in ScannerS and used for the generation of parameter points. A brief review of the constraints is given here, for more information see Refs. [37, 44].

- **S, T, U precision parameters**
  The S,T and U precision parameters [55, 56] have to be considered to constrain the parameters in the model. When introducing additional scalar fields in the theory, the contributions from these fields can be calculated and the deviation with respect to the SM result can be obtained. These deviations have to be within experimental bounds, i.e. ScannerS uses a fit result to compare the model predictions with. Then the program applies a consistency check with $95\,\%$ confidence level to see if the constraints are fulfilled.
- **Searches for scalar particles and Higgs measurements**
  With the discovery of the $125\,\mathrm{GeV}$ Higgs Boson at the LHC and other measurements and searches for additional scalar particles, the scalar sector is already severely constrained by experimental bounds, which are imported in ScannerS from the program packages HiggsBounds [57–61] and HiggsSignals [62, 63]. Therefore, agreement of the signal rates of the SM-like Higgs boson of the CxSM with the observations at 2σ level is checked by HiggsSignals-2.6.1. Through HiggsBounds-5.9.0 the exclusion bounds from searches for extra scalars are taken into account.
- **DM searches and cosmological constraints**
  The CxSM contains a dark matter candidate and therefore DM constraints are applied as well. First of all, the predicted DM relic density of this model should not exceed the measured value. Smaller values are not excluded since they allow for additional contributions coming from other sources outside of the described model. ScannerS can be linked to the program package MicrOMEGAs [64–66] to include this constraint from the relic density. Moreover, direct detection searches for DM, c.f. e.g. [67], can be used to constrain the model parameters by calculating the spin-independent cross sections and comparing with current exclusion limits.

3. Renormalization of the CxSM

It is well established that divergences occur in quantum field theories, when calculating higher-order corrections [42]. The proper treatment of these divergent terms is necessary to obtain physical results which can be compared to experimental results. In order to apply the renormalization procedure, the divergences have to be isolated. This procedure is called regularization and there are several methods to obtain a regularized result. In this thesis, dimensional regularization is used [4, 5], which means that all integrals emerging from NLO calculations are treated in general D dimensions, with $D = 4 - 2\epsilon$ and $\epsilon \longrightarrow 0$. Now the divergences have the form

$$\Delta_\epsilon = \frac{1}{\epsilon} - \gamma_{\mathrm{E}} + \ln(4\pi), \tag{3.1}$$

where γ_{E} is the Euler-Mascheroni constant [42]. The cancellation of all divergences can be tested analytically as well as numerically after the successful renormalization of the theory. Also the gauge structure of the theory is preserved with this method of regularization.

Formally, in the renormalization procedure all physical quantities β obtain a shift

$$\beta_0 = \beta + \delta\beta\,, \tag{3.2}$$

with $\delta\beta$ being the respective counterterm of the physical quantity β and β_0 being the bare unrenormalized quantity. All fields ϕ in the theory are factorized as

$$\phi_0 = \sqrt{Z_\phi}\phi \approx \left(1 + \frac{\delta Z_\phi}{2}\right)\phi\,, \tag{3.3}$$

with the unrenormalized field ϕ_0 and the field strength renormalization constant Z_ϕ. The approximation holds at NLO. Inserting these relations into the bare Lagrangian of the theory gives rise to additional Feynman diagrams at NLO including counterterms. If the counterterms are properly defined via certain conditions, the overall amplitude of a given process will be free of any divergences (also called UV-finite) and can be used to make physical predictions. The procedure of regularization and renormalization is quite involved, but the renormalizability of the SM was proven in [5]. The CxSM can be seen as an extension of the SM by only introducing renormalizable terms. Therefore the CxSM is a renormalizable theory as well.

The main part of the renormalization is to define the conditions for the derivation of the counterterms and also calculate the renormalization constants. The procedures used in this thesis follow the work of [68], but are now applied to the CxSM.

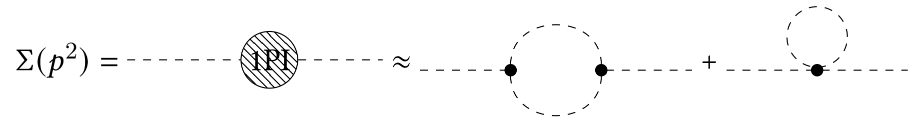

Figure 3.1.: Topologies of Feynman diagrams, which contribute to the self-energy of a scalar particle.The diagrams shown here and all following diagrams are created with [69].

3.1. On-Shell Renormalization of the Scalar Sector

One possible scheme to renormalize the theory and obtain physical amplitudes is the on-shell (OS) scheme [42]. The OS scheme is defined in a way that the given input parameters for masses of particles are the measured masses from experimental results. As a brief summary this means that all higher order corrections to the mass of a particle (i.e. the self-energy) are canceled by the respective mass counterterms to all orders of perturbation theory.

The OS scheme is introduced in the following way in the CxSM. First of all, when considering the field A, the field and the corresponding mass can be rewritten as

$$A_0 = \sqrt{Z_A} A \approx \left(1 + \frac{\delta Z_A}{2}\right) A,\ D^2_{A,0} = D^2_A + \delta D^2_A, \tag{3.4}$$

where the index 0 generally indicates the unrenormalized field, Z_A is the field strength renormalization constant and δD_A the corresponding counterterm for the mass term of A. These expressions can be put in relation with the renormalized self-energy, i.e. the self-energy combined with the propagator counterterm, which reads at NLO [42]

$$\hat{\Sigma}_A(p^2)) = \Sigma_A(p^2) - \delta D^2_A + \frac{\delta Z^*_A}{2}(p^2 - D^2_A) + (p^2 - D^2_A)\frac{\delta Z_A}{2}. \tag{3.5}$$

The unrenormalized self-energy Σ_A consists of all 1 particle-irreducible (PI) diagrams which contribute to the propagator of the particle at NLO. Diagrammatically, the self-energy of a scalar particle is determined by the diagrams given in Fig. 3.1.

The two mixing scalars h_1 and h_2 can be treated in the same way, but now the field strength renormalization constant is a matrix as well as the mass counterterm since the two fields can mix at NLO. The relations read

$$\begin{pmatrix} h_{1,0} \\ h_{2,0} \end{pmatrix} = \sqrt{Z_{hh}} \begin{pmatrix} h_1 \\ h_2 \end{pmatrix} \approx \left(1 + \frac{\delta Z_{hh}}{2}\right) \begin{pmatrix} h_1 \\ h_2 \end{pmatrix},\ D^2_{hh,0} = D^2_{hh} + \delta D^2_{hh}, \tag{3.6}$$

with the matrices

$$\delta Z_{hh} = \begin{pmatrix} \delta Z_{h_1 h_1} & \delta Z_{h_1 h_2} \\ \delta Z_{h_2 h_1} & \delta Z_{h_2 h_2} \end{pmatrix},\ \delta D^2_{hh} = \begin{pmatrix} \delta D^2_{h_1 h_1} & \delta D^2_{h_1 h_2} \\ \delta D^2_{h_1 h_2} & \delta D^2_{h_2 h_2} \end{pmatrix}. \tag{3.7}$$

As can be seen, the counterterm mass matrix is symmetric whereas the field strength renormalization matrix is, in general, not symmetric. These expressions can be again put into relation with the renormalized self-energies, which at NLO read

$$\begin{aligned}\hat{\Sigma}_{h_ih_j}(p^2) = \Sigma_{h_ih_j}(p^2) - \delta D^2_{h_ih_j} + \frac{\delta Z^\dagger_{h_ih_j}}{2}\left(p^2\delta_{h_ih_j} - D^2_{h_ih_j}\right) \\ + \left(p^2\delta_{h_ih_j} - D^2_{h_ih_j}\right)\frac{\delta Z_{h_ih_j}}{2}.\end{aligned} \tag{3.8}$$

Here and in all following equations, if nothing else is mentioned, $i, j \in \{1, 2\}$ holds.

With the above relations, the counterterms for all scalar fields can be defined by imposing certain conditions in order to achieve the goals of OS-renormalization. These corresponding equations read

$$\mathrm{Re}\left(\hat{\Sigma}_{h_1h_2}(m^2_{h_1})\right) = \mathrm{Re}\left(\hat{\Sigma}_{h_1h_2}(m^2_{h_2})\right) = 0, \tag{3.9a}$$

$$\mathrm{Re}\left(\hat{\Sigma}_{h_1h_1}(m^2_{h_1})\right) = \mathrm{Re}\left(\hat{\Sigma}_{h_2h_2}(m^2_{h_2})\right) = 0, \tag{3.9b}$$

$$\mathrm{Re}\left(\left.\frac{\partial\hat{\Sigma}_{h_1h_1}(p^2)}{\partial p^2}\right|_{(p^2=m^2_{h_1})}\right) = \mathrm{Re}\left(\left.\frac{\partial\hat{\Sigma}_{h_2h_2}(p^2)}{\partial p^2}\right|_{(p^2=m^2_{h_2})}\right) = 0. \tag{3.9c}$$

The first two conditions mean that the mixing of the two scalar particles vanishes on-shell, i.e. that the scalar particles cannot mix when the momentum is set to the respective masses of the particles. The next two conditions ensure that the poles of the propagators of the respective scalar particles remain at their masses, i.e. that the given input masses indeed match with the measured mass values. The last two conditions are used to ensure that the residuum of the propagator of the respective particle does not change and the field is properly normalized.

In the case of the scalar field A there exists no mixing with other scalar fields. The conditions on the renormalized self-energy of A simplify to

$$\mathrm{Re}\left(\hat{\Sigma}_A(m^2_A)\right) = 0, \tag{3.10a}$$

$$\mathrm{Re}\left(\left.\frac{\partial\hat{\Sigma}_A(p^2)}{\partial p^2}\right|_{(p^2=m^2_A)}\right) = 0. \tag{3.10b}$$

In all these conditions only the real part of the renormalized self-energies is used. This is due to the fact that only the real part of the amplitudes will later be considered. For a treatment of the imaginary part of the self-energies the complex mass scheme [70] can be used. In this thesis, however, the imaginary part does not need to be taken into account.

These imposed conditions can now be used to solve for the mass counterterms and field strength renormalization counterterms and lead to the expressions

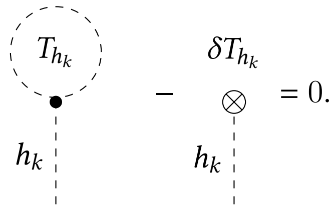

Figure 3.2.: Diagrammatic description of the tadpole renormalization condition in the mass basis.

$$\delta D^2_{h_ih_i} = \mathrm{Re}\left(\Sigma_{h_ih_i}(m^2_{h_i})\right), \tag{3.11a}$$

$$\delta Z_{h_ih_i} = -\mathrm{Re}\left(\left.\frac{\partial \Sigma_{h_ih_i}(p^2)}{\partial p^2}\right|_{p^2=m^2_{h_i}}\right), \tag{3.11b}$$

$$\delta Z_{h_ih_j} = \frac{2}{m^2_{h_i} - m^2_{h_j}}\mathrm{Re}\left(\Sigma_{h_ih_j}(m^2_{h_j}) - \delta D^2_{h_ih_j}\right)\ (i \neq j), \tag{3.11c}$$

for the counterterms of the scalar fields h_i. Similarly, the expressions for the field A read

$$\delta D^2_A = \mathrm{Re}\left(\Sigma_A(m^2_A)\right), \tag{3.12a}$$

$$\delta Z_A = -\mathrm{Re}\left(\left.\frac{\partial \Sigma_A(p^2)}{\partial p^2}\right|_{p^2=m^2_A}\right). \tag{3.12b}$$

With these expressions the counterterm δD^2_A and the mass counterterm matrix δD^2_{hh} need closer consideration. At the end the mass counterterms $\delta m^2_{h_i}$ and δm^2_A are the essential counterterms which are part of the diagonal elements of δD^2_{hh} or δD^2_A, respectively. The other parts of the diagonal and off-diagonal elements depend on the treatment of tadpole diagrams and is discussed in the next section.

3.2. Tadpole Renormalization

As already mentioned in Sec. 2.2, it is quite crucial how the tadpoles are treated [71]. The tadpole parameters in Eq. (2.8) are taken as bare parameters and at NLO they receive a shift which corresponds to a change of the vacuum state due to NLO contributions to the scalar potential. The tadpoles are then renormalized such that the vevs correspond to the same minimum as at tree level. Thus, the conditions

$$\hat{T}_1 = T_1 - \delta T_1 = 0\,,\ \hat{T}_2 = T_2 - \delta T_2 = 0, \tag{3.13a}$$

$$\Rightarrow T_1 = \delta T_1,\ T_2 = \delta T_2, \tag{3.13b}$$

are used, where T_i are the tadpoles of the respective fields H and S in the gauge basis and symbols with a circumflex indicate the renormalized quantities. From these conditions it follows that the renormalized tadpoles also have to vanish at NLO and therefore that the tree level minimum still is a minimum of the potential at NLO.

These tadpoles can also be transformed into the mass basis, which results in

$$\begin{pmatrix}\delta T_1\\ \delta T_2\end{pmatrix} = R_\alpha^{\mathrm{T}}\begin{pmatrix}\delta T_{h_1}\\ \delta T_{h_2}\end{pmatrix} = \begin{pmatrix}\delta T_{h_1}c_\alpha - \delta T_{h_2}s_\alpha\\ \delta T_{h_1}s_\alpha + \delta T_{h_2}c_\alpha\end{pmatrix}. \tag{3.14}$$

In the mass basis the conditions for the tadpole counterterms mean diagrammatically that the tadpole counterterms correspond to the tadpole contributions of the respective scalar particle (see also Fig. 3.2).

However, what the proper values of the vevs actually are and how the expressions in the mass counterterm matrix δD^2_{hh} exactly are defined have not yet been fixed by this definition. The investigation of these questions leads to two different schemes and is discussed in the following sections.

3.2.1. Standard Tadpole Scheme

The here called standard tadpole scheme is a possible way to renormalize the SM [71], and can also be used for the CxSM. The essence of this scheme is that the vev parameters are chosen such that the resulting masses from the tree level relations (2.7) and (2.8) are the proper physical masses. Therefore, all shifts coming from NLO corrections are already present in the mass counterterms and the vevs are not shifted and resemble the proper values.

For the definition of the δD^2_{hh} counterterm, Eq. (2.10) can be used to obtain the relation

$$\begin{aligned}\delta D^2_{hh} &\approx \begin{pmatrix}\delta m^2_{h_1} & 0\\ 0 & \delta m^2_{h_2}\end{pmatrix} + R_\alpha \begin{pmatrix}\frac{\delta T_1}{v} & 0\\ 0 & \frac{\delta T_2}{v_\mathrm{S}}\end{pmatrix} R_\alpha^{\mathrm{T}}\\ &\equiv \begin{pmatrix}\delta m^2_{h_1} & 0\\ 0 & \delta m^2_{h_2}\end{pmatrix} + \begin{pmatrix}\delta T_{h_1h_1} & \delta T_{h_1h_2}\\ \delta T_{h_1h_2} & \delta T_{h_2h_2}\end{pmatrix},\end{aligned} \tag{3.15}$$

where the resulting matrix from the tadpole counterterms is defined via the entries $\delta T_{h_ih_j}$. Using Eq. (3.14) to transform the tadpole counterterms into the mass basis results in

$$\delta T_{h_1h_1} = \delta T_{h_1}\frac{v_S c_\alpha^3 + v s_\alpha^3}{v v_S} + \delta T_{h_2}\frac{c_\alpha s_\alpha(v s_\alpha - v_S c_\alpha)}{v v_S}, \tag{3.16a}$$

$$\delta T_{h_1h_2} = \delta T_{h_1}\frac{c_\alpha s_\alpha(v s_\alpha - v_S c_\alpha)}{v v_S} + \delta T_{h_2}\frac{c_\alpha s_\alpha(v c_\alpha + v_S s_\alpha)}{v v_S}, \tag{3.16b}$$

$$\delta T_{h_2h_2} = \delta T_{h_1}\frac{c_\alpha s_\alpha(v c_\alpha + v_S s_\alpha)}{v v_S} + \delta T_{h_2}\frac{v c_\alpha^3 - v_S s_\alpha^3}{v v_S}. \tag{3.16c}$$

Now the mass counterterms for the fields h_i can be expressed with Eq. (3.11) as

$$\boxed{\begin{aligned} \delta m^2_{h_1} &= \mathrm{Re}\left(\Sigma_{h_1h_1}(m^2_{h_2})\right) - \delta T_{h_1h_1}, && \text{(3.17a)} \\ \delta m^2_{h_2} &= \mathrm{Re}\left(\Sigma_{h_2h_2}(m^2_{h_2})\right) - \delta T_{h_2h_2}, && \text{(3.17b)} \\ \delta D^2_{h_1h_2} &= \delta T_{h_1h_2}. && \text{(3.17c)} \end{aligned}}$$

The derivation for the field A is simpler. Using Eq. (2.11) the counterterm of D_A can be derived. Rotating the tadpole counterterms into the mass basis with Eq. (3.14) results in

$$\delta D^2_A = \delta m^2_A + \frac{\delta T_2}{v_S} = \delta m^2_A + \frac{s_\alpha T_{h_1} + c_\alpha T_{h_2}}{v_S}. \tag{3.18}$$

Using Eq. (3.12), δm^2_A can be expressed as

$$\boxed{\delta m^2_A = \mathrm{Re}\left(\Sigma_A(m^2_A)\right) - \frac{s_\alpha T_{h_1} + c_\alpha T_{h_2}}{v_S}. \qquad \text{(3.19)}}$$

The derived counterterms will lead to UV-finite results and are a viable option in this regard. However, the use of the standard tadpole scheme in combination with the renormalization of the mixing angle α in both the KOSY scheme (see Sec. 3.4.1) and the pinched scheme (see Sec. 3.4.2) will lead to gauge-dependent counterterms and also gauge-dependent amplitudes.

3.2.2. Alternative Tadpole Scheme

The alternative tadpole scheme follows the work of Fleischer and Jegerlehner [72] who introduced this scheme in the SM. Since then the alternative tadpole scheme was also applied to extended Higgs sectors, see e.g. [73, 74]. For the CxSM a description of it is given here.

In contrast to the standard tadpole scheme, in the alternative tadpole scheme, the vevs are no longer determined by their tree level values, but they also obtain a shift when considering NLO contributions. With this shift the vevs obtain their proper values since they are now also determined order by order in perturbation theory and this will lead to gauge-independent mass counterterms. Moreover, the technique will be useful later when introducing the pinch technique (see Sec. 3.4.2).

First, the additional shifts

$$\begin{aligned} v &\longrightarrow v + \Delta v, && \text{(3.20a)} \\ v_S &\longrightarrow v_S + \Delta v_S, && \text{(3.20b)} \end{aligned}$$

in the vev parameters are introduced. Using Eq. (2.8) and inserting the vev shifts leads to a relation between the tadpole counterterm and the shift in the vevs:

$$T_1 \longrightarrow T_1 + \frac{v^2\lambda}{2}\Delta v + \frac{\delta_2 v v_S}{2}\Delta v_S \equiv T_1 + \delta T_1, \tag{3.21a}$$

$$T_2 \longrightarrow T_2 + \frac{\delta_2 v v_S}{2}\Delta v + \frac{d_2 v_S^2}{2}\Delta v_S \equiv T_2 + \delta T_2. \tag{3.21b}$$

With further inspection it can be seen that this equation can be written with the help of the mass matrix (Eq. (2.7)) as

$$\Rightarrow \begin{pmatrix} \delta T_1 \\ \delta T_2 \end{pmatrix} = \mathcal{M}|_{T_i=0} \begin{pmatrix} \Delta v \\ \Delta v_S \end{pmatrix}, \tag{3.22}$$

where the tadpole parameters in the mass matrix are set to zero. Since both the mass matrix and the tadpole counterterms can be rotated with the same matrix R_α into the mass basis (see Eqs. (2.10) and (3.14)), the above equation in the mass basis results in

$$\begin{pmatrix} \Delta v_{h_1} \\ \Delta v_{h_2} \end{pmatrix} = \begin{pmatrix} \frac{\delta T_{h_1}}{m_{h_1}^2} \\ \frac{\delta T_{h_2}}{m_{h_2}^2} \end{pmatrix}. \tag{3.23}$$

This last relation can be viewed in terms of Feynman diagrams and reveals that the shift in the vev parameters corresponds to connected tadpole diagrams. This is the case since the tadpole counterterms δT_{h_i} are the respective tadpole diagrams of the given scalar particle and the inverse mass of the particle represents the corresponding propagator with zero momentum transfer (compare with Fig. 3.3).

Another useful relation is between the shift in the vevs in the gauge basis and the tadpole counterterms in the mass basis. Using Eq. (3.23) the desired relation is

$$\begin{pmatrix} \Delta v \\ \Delta v_S \end{pmatrix} = R_\alpha^{\mathrm{T}} \begin{pmatrix} \frac{\delta T_{h_1}}{m_{h_1}^2} \\ \frac{\delta T_{h_2}}{m_{h_2}^2} \end{pmatrix}. \tag{3.24}$$

The shift introduced in the vevs can now be applied to the mass matrix from Eq. (2.7). The addtional terms resulting from that shift read

$$\mathcal{M} \rightarrow \mathcal{M} + \begin{pmatrix} 2v\Delta v\lambda & \frac{\delta_2}{2}(\Delta v v_S + v\delta v_S) \\ \frac{\delta_2}{2}(\Delta v v_S + v\delta v_S) & d_2 v_S \Delta v_S \end{pmatrix} - \underbrace{\begin{pmatrix} \frac{T_1\Delta v}{v^2} & 0 \\ 0 & \frac{T_2\Delta v_S}{v_S^2} \end{pmatrix}}_{\text{vanishes}}. \tag{3.25}$$

The last term in Eq. (3.25) vanishes, because after the shift the tadpole conditions can be applied again, which means that $T_i = 0$ ($i = 1, 2$), canceling the terms. The mass matrix

$$(-i\lambda_{h_i h_j h_k})\frac{-i}{m_{h_k}^2} i\delta T_{h_k} =$$

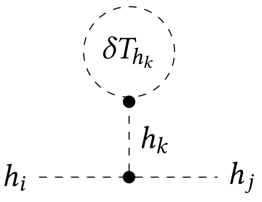

Figure 3.3.: Diagrammatic description of the additional terms appearing after the shift of the vev parameters.

can now be rotated into the mass basis and all counterterm shifts can be applied (i.e. the tadpole counterterms and mass counterterms). This leads to

$$\begin{aligned} D_{hh}^2 = R_\alpha \mathcal{M} R_\alpha^{\mathrm{T}} \;\rightarrow\; & D_{hh}^2 + \begin{pmatrix} \delta m_{h_1}^2 & 0 \\ 0 & \delta m_{h_2}^2 \end{pmatrix} \\ & + R_\alpha \begin{pmatrix} \frac{\delta T_1}{v} + 2v\Delta v\lambda & \frac{\delta_2}{2}(\Delta v v_S + v\delta v_S) \\ \frac{\delta_2}{2}(\Delta v v_S + v\delta v_S) & \frac{\delta T_2}{v_S} + d_2 v_S \Delta v_S \end{pmatrix} R_\alpha^{\mathrm{T}} \\ & \equiv D_{hh}^2 + \begin{pmatrix} \delta m_{h_1}^2 & 0 \\ 0 & \delta m_{h_2}^2 \end{pmatrix} + \begin{pmatrix} \Delta D_{h_1 h_1}^2 & \Delta D_{h_1 h_2}^2 \\ \Delta D_{h_1 h_2}^2 & \Delta D_{h_2 h_2}^2 \end{pmatrix} . \end{aligned} \tag{3.26}$$

Using Eqs. (3.14) and (3.24) to rotate all vev shifts and tadpole counterterms into the mass basis and using Eqs. (2.20) to express all parameters in terms of input parameters, ΔD_{hh}^2 can be brought into the form

$$\Delta D_{h_1 h_1}^2 = \delta T_{h_1} \left(\frac{3(v_S c_\alpha^3 + v s_\alpha^3)}{v v_S} \right) + \delta T_{h_2} \left(\frac{(2m_{h_1}^2 + m_{h_2}^2) c_\alpha s_\alpha (v s_\alpha - v_S c_\alpha)}{v v_S m_{h_2}^2} \right) , \tag{3.27a}$$

$$\begin{aligned} \Delta D_{h_1 h_2}^2 = \delta T_{h_1} & \left(\frac{(2m_{h_1}^2 + m_{h_2}^2) c_\alpha s_\alpha (v s_\alpha - v_S c_\alpha)}{v v_S m_{h_1}^2} \right) \\ + \delta T_{h_2} & \left(\frac{(m_{h_1}^2 + 2m_{h_2}^2) c_\alpha s_\alpha (v_S s_\alpha + v c_\alpha)}{v v_S m_{h_2}^2} \right) , \end{aligned} \tag{3.27b}$$

$$\Delta D_{h_2 h_2}^2 = \delta T_{h_1} \left(\frac{(m_{h_1}^2 + 2m_{h_2}^2) c_\alpha s_\alpha (v_S s_\alpha + v c_\alpha)}{v v_S m_{h_1}^2} \right) + \delta T_{h_2} \left(\frac{3(v c_\alpha^3 - v_S s_\alpha^3)}{v v_S} \right) . \tag{3.27c}$$

The interesting part now is to compare the entries with the trilinear Higgs self-couplings

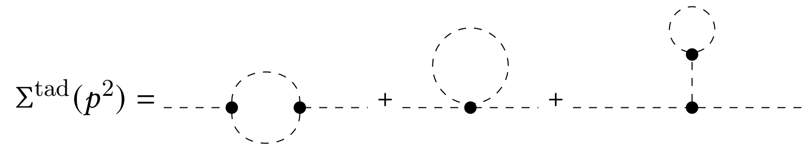

Figure 3.4.: Diagrammatic description of the self-energy including tadpole diagrams.

of the fields. These can be written as

$$\lambda_{h_1h_1h_1} = 3m_{h_1}^2 \frac{v_S c_\alpha^3 + v s_\alpha^3}{v v_S}, \tag{3.28a}$$

$$\lambda_{h_1h_1h_2} = \frac{(2m_{h_1}^2 + m_{h_2}^2) s_\alpha c_\alpha (v s_\alpha - v_S c_\alpha)}{v v_S}, \tag{3.28b}$$

$$\lambda_{h_1h_2h_2} = \frac{(m_{h_1}^2 + 2m_{h_2}^2) s_\alpha c_\alpha (v c_\alpha + v_S s_\alpha)}{v v_S}, \tag{3.28c}$$

$$\lambda_{h_2h_2h_2} = 3m_{h_2}^2 \frac{v c_\alpha^3 - v_S s_\alpha^3}{v v_S}. \tag{3.28d}$$

With these couplings the following holds:

$$\Delta D_{h_1h_1}^2 = i(-i\lambda_{h_1h_1h_1}) \frac{-i}{m_{h_1}^2} i\delta T_{h_1} + i(-i\lambda_{h_1h_1h_2}) \frac{-i}{m_{h_2}^2} i\delta T_{h_2}, \tag{3.29a}$$

$$\Delta D_{h_1h_2}^2 = i(-i\lambda_{h_1h_1h_2}) \frac{-i}{m_{h_1}^2} i\delta T_{h_1} + i(-i\lambda_{h_1h_2h_2}) \frac{-i}{m_{h_2}^2} i\delta T_{h_2}, \tag{3.29b}$$

$$\Delta D_{h_2h_2}^2 = i(-i\lambda_{h_1h_2h_2}) \frac{-i}{m_{h_1}^2} i\delta T_{h_1} + i(-i\lambda_{h_2h_2h_2}) \frac{-i}{m_{h_2}^2} i\delta T_{h_2}. \tag{3.29c}$$

In terms of Feynman diagrams this corresponds to the respective tadpole contributions (times a factor of i, at vanishing momentum transfer) to the propagators of h_1 and h_2, which so far have not been included into the definition of the self-energies. The diagrammatic expression can also be seen in Fig. 3.3.

With this diagrammatic interpretation in mind, the definition

$$i\Sigma_{h_ih_j}^{\text{tad}}(p^2) \equiv i\Sigma_{h_ih_j}(p^2) - i\Delta D_{h_ih_j}^2, \tag{3.30}$$

can be used so that the renormalized self-energy now reads

$$\begin{aligned}\hat{\Sigma}_{h_ih_j}(p^2) = \Sigma_{h_ih_j}^{\text{tad}}(p^2) - \begin{pmatrix} \delta m_{h_1}^2 & 0 \\ 0 & \delta m_{h_2}^2 \end{pmatrix} + \frac{\delta Z_{h_ih_j}^\dagger}{2} \left(p^2 \delta_{h_ih_j} - D_{h_ih_j}^2\right) \\ + \left(p^2 \delta_{h_ih_j} - D_{h_ih_j}^2\right) \frac{\delta Z_{h_ih_j}}{2}.\end{aligned} \tag{3.31}$$

This shifting of contributions from the mass counterterm matrix into the self-energy corresponds to the inclusion of the tadpole diagrams into the self-energy. Thus, the tadpole-included self-energies are defined diagrammatically as seen in Fig. 3.4.

With this change in the renormalized self-energy, the same procedure as in Sec. 3.1 can be applied to obtain the following results for the counterterms:

$$\boxed{\begin{aligned} \delta m_{h_i}^2 &= \mathrm{Re}\left(\Sigma_{h_ih_i}^{\mathrm{tad}}(m_{h_i}^2)\right), && (3.32\mathrm{a})\\ \delta Z_{h_ih_i} &= -\mathrm{Re}\left(\left.\frac{\partial\Sigma_{h_ih_i}^{\mathrm{tad}}(p^2)}{\partial p^2}\right|_{p^2=m_{h_i}^2}\right), && (3.32\mathrm{b})\\ \delta Z_{h_ih_j} &= \frac{2}{m_{h_i}^2-m_{h_j}^2}\mathrm{Re}\left(\Sigma_{h_ih_j}^{\mathrm{tad}}(m_{h_j}^2)\right)\ (i\neq j). && (3.32\mathrm{c})\end{aligned}}$$

The case for the field A is simpler. Introducing the shift of the vev parameters in the mass term D_A^2 leads to

$$D_A^2 = m_A^2 + \frac{T_2}{v_S} \longrightarrow m_A^2 + \frac{T_2}{v_S} - \underbrace{\frac{T_2\Delta v_S}{v_S^2}}_{\text{vanishes}}. \tag{3.33}$$

Again the last part vanishes due to the fact that the minimization conditions can be applied. Since the above relation is now independent of the vev parameter shifts, it follows that the shifts of the vev parameters do not change the prescription for the mass counterterm δm_A^2 with respect to the standard tadpole scheme. Thus, Eq. (3.19) gives already the correct prescription for δm_A^2 in the alternative tadpole scheme. Moreover, when considering the tree-level coupling constants between the scalars h_1, h_2 and A, which read

$$\lambda_{h_1AA} = \frac{s_\alpha m_{h_1}^2}{v_S}, \tag{3.34a}$$

$$\lambda_{h_2AA} = \frac{c_\alpha m_{h_2}^2}{v_S}. \tag{3.34b}$$

It can be seen that Eq. (3.19) can be written as

$$\delta D_A^2 = \delta m_A^2 + i(-i\lambda_{h_1AA})\frac{-i}{m_{h_1}^2}i\delta T_{h_1} + i(-i\lambda_{h_2AA})\frac{-i}{m_{h_2}^2}i\delta T_{h_1}. \tag{3.35}$$

The additional tadpole contributions again correspond diagrammatically to the inclusion of tadpole diagrams to the self-energy. Thus, the counterterms of the field A can be expressed as

$$\boxed{\begin{aligned} \delta m_A^2 &= \mathrm{Re}\left(\Sigma_A^{\mathrm{tad}}(m_A^2)\right), && (3.36)\\ \delta Z_A &= -\mathrm{Re}\left(\left.\frac{\partial\Sigma_A^{\mathrm{tad}}(p^2)}{\partial p^2}\right|_{p^2=m_A^2}\right). && (3.37)\end{aligned}}$$

$$(-i\lambda_{h_i h_k AA})\frac{-i}{m^2_{h_k}} i\delta T_{h_k} =$$

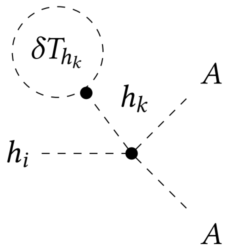

Figure 3.5.: The additional tadpole contribution to the vertex corrections at NLO after the shift of the vevs in the alternative tadpole scheme, here $k \in \{1, 2\}$.

The additional shifts in the vev parameters do not only appear in the mass counterterms, but they also introduce additional diagram contributions in the calculation of Feynman amplitudes.

As an example, the tree level diagram $h_1 \longrightarrow AA$ is considered (see also Fig. 4.3). The amplitude of this diagram is in essence the coupling constant $\lambda_{h_1 AA}$. When moving from leading order (LO) to NLO the shifts in the vev parameters now have to be included as well. The coupling constant shifts to

$$\begin{aligned}
\lambda_{h_1 AA} &= \frac{1}{2}(d_2 v_S s_\alpha + \delta_2 v c_\alpha) \longrightarrow \lambda_{h_1 AA} + \frac{1}{2}(d_2 \Delta v_S s_\alpha + \delta_2 \Delta v c_\alpha) \\
&= \lambda_{h_1 AA} + \frac{\delta T_{h_1}}{m^2_{h_1}} \left(\frac{1}{2}(d_2 s^2_\alpha + \delta_2 c^2_\alpha)\right) + \frac{\delta T_{h_2}}{m^2_{h_2}} \left(\frac{1}{2}(d_2 s_\alpha c_\alpha - \delta_2 s_\alpha c_\alpha)\right) \\
&\equiv \lambda_{h_1 AA} + \Delta\lambda_{h_1 AA}.
\end{aligned} \tag{3.38}$$

Here the coupling constant expressed with the potential parameters has to be used. After the vev shift is applied, the tadpole conditions (Eq. (2.8)) are used to express the parameters through the chosen input parameters. Using the coupling constants

$$\lambda_{h_1 h_1 AA} = \frac{1}{2}(d_2 s^2_\alpha + \delta_2 c^2_\alpha), \tag{3.39a}$$

$$\lambda_{h_1 h_2 AA} = \frac{1}{2}(d_2 s_\alpha c_\alpha - \delta_2 c_\alpha s_\alpha), \tag{3.39b}$$

the shift $\Delta\lambda_{h_1 AA}$ in the coupling constant can be written as

$$\Delta\lambda_{h_1 AA} = i(-i\lambda_{h_1 h_1 AA})\frac{-i}{m^2_{h_1}} i\delta T_{h_1} + i(-i\lambda_{h_1 h_2 AA})\frac{-i}{m^2_{h_2}} i\delta T_{h_2}, \tag{3.40}$$

which now corresponds diagrammatically to the diagrams seen in Fig. 3.5. Therefore, the shifts in the vev parameters introduce vertex corrections at NLO in the form of all possible tadpole diagrams which can be attached to the vertex.

To summarize this section: in the alternative tadpole scheme the introduction of additional shifts in the vev parameters leads to the inclusion of tadpole diagrams in various ways:

- Change all self-energies such that they also contain the tadpole contributions:

$$\Sigma(p^2) \longrightarrow \Sigma^{\text{tad}}(p^2). \tag{3.41}$$

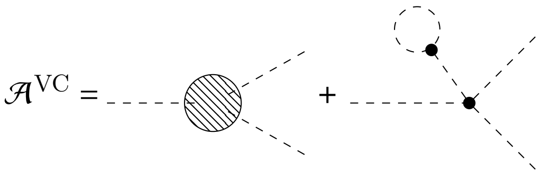

Figure 3.6.: Diagrammatic description of the addition of tadpole diagrams to the Feynman amplitude.

- Add to the virtual vertex corrections all possible tadpole corrections (see also Fig. 3.6):

$$\mathcal{A}_{\text{NLO}} \;\rightarrow\; \mathcal{A}_{\text{NLO}} + \mathcal{A}_{\text{tad}}. \tag{3.42}$$

3.3. Fermionic and Bosonic Sector

With the discussion of the renormalization of the scalar sector completed, the counterterms for the fermionic and bosonic fields are presented. Similar to the scalar fields, the shifts from the bare quantities to the renormalized quantities plus counterterms can be introduced as

$$f_0^{\text{L}} = \sqrt{Z_f^{\text{L}}} f_{\text{L}} \approx \left(1 + \frac{\delta Z_f^{\text{L}}}{2}\right) f_{\text{L}}\,, \tag{3.43a}$$

$$f_0^{\text{R}} = \sqrt{Z_f^{\text{R}}} f_{\text{R}} \approx \left(1 + \frac{\delta Z_f^{\text{R}}}{2}\right) f_{\text{R}}\,, \tag{3.43b}$$

$$m_{f,0} = m_f + \delta m_f\,, \tag{3.43c}$$

for the generic left- and right-handed fields f_{L} and f_{R}, respectively, of a fermion f with mass m_f, where for simplicity no mixing between different fermion states was assumed. In a similar manner, the counterterms of the gauge bosons for the fields and masses are introduced as

$$W^{\pm} \approx \left(1 + \frac{\delta Z_W}{2}\right) W^{\pm}, \tag{3.44a}$$

$$m_{W,0}^2 = m_W^2 + \delta m_W^2, \tag{3.44b}$$

$$\begin{pmatrix} Z_0 \\ \gamma_0 \end{pmatrix} \approx \begin{pmatrix} 1 + \frac{\delta Z_{ZZ}}{2} & \frac{\delta Z_{Z\gamma}}{2} \\ \frac{\delta Z_{\gamma Z}}{2} & 1 + \frac{\delta Z_{\gamma\gamma}}{2} \end{pmatrix} \begin{pmatrix} Z \\ \gamma \end{pmatrix}, \tag{3.44c}$$

$$m_{Z,0}^2 = m_Z^2 + \delta m_Z^2, \tag{3.44d}$$

where the mixing between the Z boson and the photon γ has to be taken into account. Moreover, the electromagnetic charge e also obtains a counterterm, which can be written at NLO as

$$e_0 = (1 + \delta Z_e)e. \tag{3.45}$$

The OS scheme can also be applied to the fermion and gauge boson sector to impose conditions on the renormalized self-energies of the respective fermions and gauge bosons. However, the additional Lorentz structure or polarization structure, respectively, of the considered fields plays an important role. Thus, the derivation of the counterterms is more involved than in the scalar sector. Additionally, the electromagnetic coupling constant e is renormalized through the Thomson limit, i.e. by fixing the value of the constant through Thomson scattering between an electron and a photon with vanishing photon momentum [42, 71].

Since the calculations made in this thesis do not depend on the renormalization of the fermion and gauge boson sector, the derivation of the counterterms for the respective fields is ommitted here. A detailed discussion can be found in e.g. [71].

3.4. Renormalization of α

After the renormalization of the fields and the corresponding masses, the remaining input parameters have to be treated carefully as well. One of the chosen input parameters is the mixing angle α, which rotates the fields H and S into the mass basis h_1 and h_2. It can also be split up as

$$\alpha_0 = \alpha + \delta\alpha, \tag{3.46}$$

where the index 0 again describes the unrenormalized bare quantity, and α is the renormalized parameter.

The mixing angle, however, is more subtle to renormalize since it is not a quantity that can be directly observed. There are various possible ways to renormalize α, e.g. the modified Minimal Subtraction ($\overline{\text{MS}}$) scheme [42, 68] or the process-dependent scheme (see Sec. 3.5.1), but they are not considered here. The $\overline{\text{MS}}$ scheme tends to be unstable, in the sense that the NLO corrections are unacceptably large, whereas for the process-dependent scheme there are not that many suitable processes in the CxSM model and it has its own limitations as well, so it is not chosen for the renormalization of α.

In this thesis two renormalization schemes for α are used, the KOSY scheme as well as the pinched scheme which are described in the following sections.

3.4.1. KOSY Scheme

The KOSY scheme is a renormalization procedure introduced by Kanemura et. al in [75] and is explained here for the CxSM.

The KOSY scheme starts with the rotation matrix R_α. By introducing the shift in α with Eq. (3.46), the mixing matrix R_α obtains a shift which can be expressed at NLO as

$$R_{\alpha,0} \approx R_{\delta\alpha} R_\alpha . \tag{3.47}$$

The mixing matrix relates the mass eigenstates of the scalar fields to the gauge eigenstates. Thus, the bare mass eigenstates can be rotated back into gauge eigenstates, then shifted to renormalized gauge eigenstates and rotated back into mass eigenstates with the renormalized mixing matrix. The resulting relation is given by

$$\begin{pmatrix} h_{1,0} \\ h_{2,0} \end{pmatrix} = R_{\alpha,0} \begin{pmatrix} h_0 \\ s_0 \end{pmatrix} \approx R_{\delta\alpha} R_\alpha \sqrt{Z_\mathrm{G}} \begin{pmatrix} h \\ s \end{pmatrix} = \sqrt{Z_{KOSY}} \begin{pmatrix} h_1 \\ h_2 \end{pmatrix}, \tag{3.48}$$

$$\sqrt{Z_{KOSY}} \equiv R_{\delta\alpha} R_\alpha \sqrt{Z_\mathrm{G}} R_\alpha^T, \tag{3.49}$$

where Eq. (3.47) was used. The matrix Z_G corresponds to the field strength renormalization matrix used to renormalize the gauge eigenstates. The matrix can be written at NLO as

$$\sqrt{Z_\mathrm{G}} \approx 1 + \frac{\delta Z_\mathrm{G}}{2}, \tag{3.50}$$

$$\frac{1}{2} R_\alpha \delta Z_\mathrm{G} R_\alpha^T \equiv \begin{pmatrix} \delta B & \delta C \\ \delta C & \delta B \end{pmatrix}, \tag{3.51}$$

with the additional counterterms δB and δC. Here the matrix δZ_G is assumed to be symmetric. The field strength renormalization matrix Z_KOSY now has to match with the field strength renormalization of the mass basis Z_{hh} (see Eq. (3.7)). At NLO this leads to

$$\begin{aligned} \sqrt{Z_\mathrm{KOSY}} &= R_{\delta\alpha} R_\alpha \sqrt{Z_\mathrm{G}} R_\alpha^T \\ &\approx R_{\delta\alpha} + \frac{1}{2} R_\alpha \delta Z_\mathrm{G} R_\alpha^T \approx \begin{pmatrix} 1+\delta B & \delta C + \delta\alpha \\ \delta C - \delta\alpha & 1 + \delta B \end{pmatrix} \overset{!}{=} 1 + \frac{\delta Z_{hh}}{2}. \end{aligned} \tag{3.52}$$

The off-diagonal elements are the important conditions and result in the equations

$$\frac{\delta Z_{h_1 h_2}}{2} = \delta C + \delta\alpha, \quad \frac{\delta Z_{h_2 h_1}}{2} = \delta C - \delta\alpha. \tag{3.53}$$

Thus, the counterterm for α reads

$$\delta\alpha = \frac{\delta Z_{h_1 h_2} - \delta Z_{h_2 h_1}}{4}. \tag{3.54}$$

With Eq. (3.32) $\delta\alpha$ can be expressed in terms of self-energies as

$$\boxed{\delta\alpha = \frac{1}{2(m_{h_1}^2 - m_{h_2}^2)} \mathrm{Re}\left(\Sigma_{h_1 h_2}^{tad}(m_{h_1}^2) + \Sigma_{h_1 h_2}^{tad}(m_{h_2}^2)\right).} \tag{3.55}$$

This equation holds for the alternative tadpole scheme. The same relation also is true for the standard tadpole scheme, but with normal self-energies instead of tadpole self-energies.

The issue now with this derivation is that the above combination of self-energies is not gauge-independent. Thus, $\delta\alpha$ will be gauge-dependent for both the standard and the alternative tadpole scheme . This is in itself not a problem as long as the overall amplitude of a given process and hence the physical observables are gauge-independent. However, as will be seen in Sec. 4.5, if there is a gauge-dependent counterterm of $\delta\alpha$, an overall gauge dependence will be introduced so that the overall amplitude and, accordingly, physical observables will be gauge-dependent. This is a problem since physical observables are per definition gauge-independent.

Upon closer inspection, the gauge problem in the KOSY scheme arises from the assumption that the matrix δZ_{G} has to be symmetric. Since the field strength renormalization matrix δZ_{hh} in the mass basis is not symmetric, δZ_{G} can also be, in general, asymmetric. Dropping this symmetry assumption leads to an additional degree of freedom and the Eqs. (3.53) change to

$$\frac{\delta Z_{h_1 h_2}}{2} = \delta C + \delta\alpha, \quad \frac{\delta Z_{h_2 h_1}}{2} = \delta G - \delta\alpha, \tag{3.56}$$

where δG is an additional counterterm, which does not appear in any calculations. These equations are now under determined and the counterterms $\delta\alpha$, δG and δC can be defined in a way that $\delta\alpha$ is gauge-independent by shifting all gauge-dependent parts into the other unphysical counterterms δG and δC.

With this procedure $\delta\alpha$ becomes gauge-independent and the above mentioned problem seems to be solved. However, since there is this additional freedom coming from the dropping of the symmetry requirement on δZ_{G}, it is not quite clear how exactly $\delta\alpha$ should be defined. Therefore, an additional scheme has to be introduced to exactly define $\delta\alpha$ in a gauge-independent way. This is the so called pinched scheme.

3.4.2. Pinched Scheme

The pinched scheme was already implemented in the 2-Higgs-Doublet Model (2HDM) [73] and the singlet extension of the 2HDM (N2HDM) [74] and the discussion here in the CxSM follows their implementation.

The pinched scheme is based on the pinch technique [76–80] which can be used to obtain expressions for gauge-independent self-energies. The pinch technique starts with considering a certain physical process, e.g. a 2 → 2 scattering process with external fermions. The overall amplitude $\mathcal{A}_{\mathrm{total}}$ can be split up into different contributions

$$\mathcal{A}_{\mathrm{total}} = \mathcal{A}_{\mathrm{box}}(\{\xi\}) + \mathcal{A}_{\mathrm{tri}}(\{\xi\}) + \mathcal{A}_{\mathrm{leg}}(\{\xi\}) + \mathcal{A}_{\mathrm{self}}(\{\xi\}), \tag{3.57}$$

with box, triangle, self-energy diagrams as well as external leg corrections, which all by themselves can be gauge-dependent (where the gauge parameters are abbreviated with $\{\xi\}$) but the combination of them is gauge-independent. Therefore it is possible to shift certain contributions in such a way that the different contributions are already gauge-independent by themselves and the relation

$$\mathcal{A}_{\mathrm{total}} = \hat{\mathcal{A}}_{\mathrm{box}} + \hat{\mathcal{A}}_{\mathrm{tri}} + \hat{\mathcal{A}}_{\mathrm{leg}} + \hat{\mathcal{A}}_{\mathrm{self}}, \tag{3.58}$$

holds, where the circumflex signals the different contributions after the pinch technique was applied. With this approach gauge-independent self-energies can be created. A more detailed description of the pinch technique is given in App. A.1.

After successfully applying the pinch technique, the pinched self-energies can be defined by adding the additional contributions to the self-energies from the Pinch technique. This results in

$$\begin{aligned} i\Sigma^{\text{pinch}}_{h_ih_j}(p^2) &= i\Sigma^{\text{tad}}_{h_ih_j}(p^2) + i\Sigma^{\text{add}}_{h_ih_j}(p^2) \\ &= i\Sigma^{\text{tad}}_{h_ih_j}(p^2)\Big|_{\{\xi=1\}} \\ &+ \frac{-ig^2}{32\pi^2 c_{\text{W}}^2}\left(p^2 - \frac{m^2_{h_i}+m^2_{h_j}}{2}\right) O_{ij} B_0(q^2, m_Z^2, m_Z^2) \\ &+ \frac{-ig^2}{16\pi^2}\left(p^2 - \frac{m^2_{h_i}+m^2_{h_j}}{2}\right) O_{ij} B_0(q^2, m_W^2, m_W^2). \end{aligned} \tag{3.59}$$

The integral B_0 and the factor O_{ij} as well as $\Sigma^{\text{add}}_{h_ih_j}(p^2)$ are defined in the App. A.1. The expression $\xi = 1$ does not mean that a specific gauge is chosen. The additional terms together with the tadpole self-energies result in a gauge-independent result which can be written in that way. Moreover, the cancellation of the gauge-dependent parts only happens with the inclusion of tadpole contributions, i.e. the pinched self-energies are only gauge-independent when using tadpole self-energies Σ^{tad}. This is the main reason why the alternative tadpole scheme was introduced.

With the pinched self-energies now a gauge-independent counterterm for α can be defined. But first, the scale at which the self-energies are evaluated have to be chosen. Two different scales are used in this thesis:

- Setting the external momenta to the respective OS masses, $p^2 = m^2_{h_i}$, here called OS pinched scheme.
- Setting the external momenta to the mean of the masses, $p^2 = p^2_* = \frac{m^2_{h_1}+m^2_{h_2}}{2}$, here called p^* pinched scheme.

The p^* pinched scheme is useful, because the additional gauge-independent terms from the pinch technique vanish.

At the end, when using the pinched self-energies instead of the tadpole self-energies in Eq. (3.55), the resulting counterterm for α in the p_* scheme and the OS pinched scheme, respectively, reads

$$\boxed{\begin{aligned} \delta\alpha_{p^*} &= \frac{1}{(m^2_{h_1} - m^2_{h_2})}\text{Re}\left(\Sigma^{tad}_{h_1h_2}(p^2_*)\Big|_{\{\xi=1\}}\right), && (3.60\text{a}) \\ \delta\alpha_{\text{OS}} &= \frac{1}{2(m^2_{h_1} - m^2_{h_2})}\text{Re}\left(\Sigma^{\text{pinch}}_{h_1h_2}(m^2_{h_1}) + \Sigma^{\text{pinch}}_{h_1h_2}(m^2_{h_2})\right). && (3.60\text{b}) \end{aligned}}$$

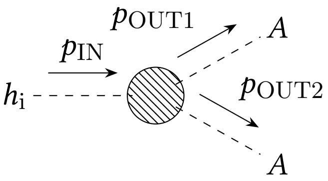

Figure 3.7.: The kinematics of the decay processes used in the process-dependent scheme.

It is clear that these definitions for $\delta\alpha$ are by construction gauge-independent and the problem with the gauge dependence is solved. Moreover, the UV divergencies in the additional terms vanish in the OS pinched scheme, whereas in the p^* pinched scheme the additional terms are even canceled totally. Therefore, both schemes have the same UV behavior for the counterterm of α, as it should be.

3.5. Renormalization of v_S

The only remaining input parameter that needs to be renormalized is the scalar singlet vev v_S. The shift of v_S in the alternative tadpole scheme is not to be confused with the renormalization counterterm δv_S, which also has to be determined. The vev can be split up as

$$v_{S,0} = v_S + \delta v_S, \tag{3.61}$$

where the index 0 again describes the bare unrenormalized parameter.

The renormalization of v_S is not covered by the OS scheme or any other scheme already implemented and discussed above. Therefore an additional procedure for v_S has to be found. Similar approaches were already made in other works [73, 74]. Here the same discussion is repeated for the CxSM.

3.5.1. Process-dependent Scheme

For the renormalization of v_S the process-dependent scheme is used. In the process-dependent scheme the input parameter is renormalized through a chosen physical process so that the value of this parameter can be defined and measured through this process. In this sense the process-dependent scheme is similar to the OS scheme as it links the model parameters through the renormalization to experimental results, i.e. the measurement of a certain process. By using a physical process, which has to be gauge-independent, the resulting counterterm is gauge-independent. However, certain kinematic constraints which are needed for the process to be physically allowed (for example in a decay process) have to be applied for the chosen set of model parameters as well.

To begin with, for the process-dependent scheme a suitable process is chosen. The chosen process has to depend on the parameter, which is renormalized, at LO in order to derive an expression for the counterterm of the parameter.

In the process-dependent scheme the counterterm which needs to be calculated is defined by demanding that the relation,

$$\Gamma^{\text{LO}}_{X\to YZ} = \Gamma^{\text{NLO}}_{X\to YZ}, \tag{3.62}$$

between the LO and NLO decay width for X decaying into the final state YZ holds. In order to use the process-dependent scheme for the renormalization of v_S a decay has to be chosen where v_S appears at LO since otherwise the counterterm δv_S would not appear at NLO and Eq. (3.62) cannot be used to solve for δv_S. Therefore, only decays involving scalar particles can be used. In the following, only the decays $h_1 \to AA$ and $h_2 \to AA$ are considered. The general topology of these decays, including the nomenclature for the kinematics, can be found in Fig. 3.7. Both decays are used in Sec. 4.5.

In order to derive the counterterm of v_S, the expressions for the LO and NLO decay width as well as the occurring counterterms in the NLO result are needed. They are derived in Sec. 4.5 but are already applied here. Using the Eqs. (4.5) and (4.6) for the processes $h_i \to AA$ to express the decay widths in Eq. (3.62), the relation can be simplified to

$$0 = \text{Re}\left(\left(\mathcal{A}^{\text{LO}}_{h_i\to AA}\right)^* \mathcal{A}^{\text{NLO}}_{h_i\to AA}\right), \tag{3.63}$$

where $\mathcal{A}^{\text{LO}}_{h_i\to AA}$ are all contributions to the process $h_i \to AA$ at LO and $\mathcal{A}^{\text{NLO}}_{h_i\to AA}$ are all contributions at NLO. At LO the amplitudes for the two processes only depend on the corresponding coupling constant and are therefore real and non-zero for valid input parameters (cf. Sec. 4.4). Thus, Eq. (3.63) further simplifies to

$$0 = \text{Re}\left(\mathcal{A}^{\text{NLO}}_{h_i\to AA}\right). \tag{3.64}$$

Next, the NLO contribution $\mathcal{A}^{\text{NLO}}_{h_i\to AA}$ can be expressed in terms of vertex corrections $\mathcal{A}^{\text{VC}}_{h_i\to AA}$ and the vertex counterterm (cf. Sec.4.5). The vertex counterterm can be further derived from the counterterm Lagrangian and Eq. (3.63) results in

$$\begin{aligned} 0 &= \text{Re}\left(\mathcal{A}^{\text{NLO}}_{h_i\to AA}\right) \\ &= \text{Re}\left(\mathcal{A}^{\text{VC}}_{h_i\to AA}\right) - \lambda_{h_iAA}\left(\frac{\delta\lambda_{h_iAA}}{\lambda_{h_iAA}} + \delta Z_A + \frac{\delta Z_{h_ih_i}}{2} + \frac{\lambda_{h_jAA}}{\lambda_{h_iAA}}\frac{\delta Z_{h_jh_i}}{2}\right), \end{aligned} \tag{3.65}$$

where $i, j \in \{1, 2\}$, but $i \neq j$. All counterterms appearing in the expression are already real.

Next, the expression for $\delta\lambda_{h_iAA}$ has to be determined. The coupling constants λ_{h_iAA} have already been given in Eq. (3.34) and the corresponding counterterm can be derived. The results read

$$\lambda_{h_1AA} = \frac{s_\alpha m_{h_1}^2}{v_S} \quad\longrightarrow\quad \delta\lambda_{h_1AA} = \frac{\delta m_{h_1}^2}{m_{h_1}^2}\lambda_{h_1AA} - \frac{\delta v_S}{v_S}\lambda_{h_1AA} + \cot(\alpha)\delta\alpha\lambda_{h_1AA}, \tag{3.66a}$$

$$\lambda_{h_2AA} = \frac{c_\alpha m_{h_2}^2}{v_S} \quad\longrightarrow\quad \delta\lambda_{h_2AA} = \frac{\delta m_{h_2}^2}{m_{h_2}^2}\lambda_{h_2AA} - \frac{\delta v_S}{v_S}\lambda_{h_2AA} - \tan(\alpha)\delta\alpha\lambda_{h_2AA}, \tag{3.66b}$$

$$\Rightarrow \frac{\delta\lambda_{h_iAA}}{\lambda_{h_iAA}} = \frac{\delta m_{h_i}^2}{m_{h_i}^2} - \frac{\delta v_S}{v_S} + T_i(\alpha)\delta\alpha, \tag{3.66c}$$

$$T_i(\alpha) \equiv \begin{cases} \cot(\alpha), i = 1 \\ -\tan(\alpha), i = 2 \end{cases} . \tag{3.66d}$$

Thus, Eq. (3.64) can be solved for v_S to obtain the results

$$\boxed{\begin{aligned} \delta v_S^{h_1\to AA} &= v_S\left(-\mathrm{Re}\left(\frac{\mathcal{A}^{\mathrm{VC}}_{h_1\to AA}}{\lambda_{h_1AA}}\right) + \frac{\delta m_{h_1}^2}{m_{h_1}^2} + \cot(\alpha)\delta\alpha + \delta Z_A \right. && (3.67\mathrm{a})\\ &\qquad\left. + \frac{\delta Z_{h_1h_1}}{2} + \frac{\lambda_{h_2AA}}{\lambda_{h_1AA}}\frac{\delta Z_{h_2h_1}}{2}\right), \\ \delta v_S^{h_2\to AA} &= v_S\left(-\mathrm{Re}\left(\frac{\mathcal{A}^{\mathrm{VC}}_{h_2\to AA}}{\lambda_{h_2AA}}\right) + \frac{\delta m_{h_2}^2}{m_{h_2}^2} - \tan(\alpha)\delta\alpha + \delta Z_A \right. && (3.67\mathrm{b})\\ &\qquad\left. + \frac{\delta Z_{h_2h_2}}{2} + \frac{\lambda_{h_1AA}}{\lambda_{h_2AA}}\frac{\delta Z_{h_1h_2}}{2}\right), \end{aligned}}$$

for the two processes. The thus defined counterterms are gauge-independent and will lead to UV-finite results.

The main drawback of the process-dependent scheme is that it can only be used if the kinematic constraints are fulfilled. For a decay process this means that the sum of the masses of the outgoing particles is smaller than the mass of the incoming particle, i.e. that for the usage of the process-dependent scheme one of the additional constraints

$$m_{h_i} > 2m_A, \tag{3.68}$$

has to be fulfilled by the chosen set of input parameters in addition to the theoretical and experimental constraints. A possible solution to this is discussed in the next section.

3.5.2. ZEM Scheme

The Zero External Momentum (ZEM) scheme was introduced in [81] to get rid of the additional kinematic constraint from the process-dependent scheme. In the following it is discussed for the CxSM model.

The ZEM scheme uses the same approach as the process-dependent scheme, namely requiring that the LO and NLO results for the decay width of a chosen process are equal. The counterterm δv_S then is derived from the relation (3.62). The key difference to the process-dependent scheme is that in the ZEM scheme, as the name suggests, all external momenta are set to zero. More precisely, when the process with the kinematics described as in Fig. 3.7 is used, the relations

$$p_{\text{IN}}^2 = p_{\text{OUT1}}^2 = p_{\text{OUT2}}^2 = 0, \tag{3.69}$$

are required, hence all squared external momenta are not set to their on-shell mass values but to zero instead. This has the desired effect that the kinematic constraint on the described decay is eliminated and the process can now be used for the renormalization of v_S for all generated parameter points that pass the applied theoretical and experimental constraints. No additional kinematic constraint has to be applied on the input parameters. This should, however, not be confused with setting the masses of the particles, i.e. the input parameters to zero. Only the terms with squared external momenta in the calculation of the amplitude are set to zero.

For the ZEM scheme, the same processes are chosen as for the process-dependent scheme (see Sec. 3.5.1). Thus, the LO contribution of the processes are again real and the starting point of the derivation of the counterterm for δv_S is

$$0 = \text{Re}\left(\mathcal{A}^{\text{NLO}}_{h_i \to AA}(\{p^2 = 0\})\right), \tag{3.70}$$

where $p^2 = 0$ means that all squared external momenta are set to zero. The next key difference to the process-dependent scheme is that the leg corrections of the process at NLO do not get canceled by the respective leg counterterms, since the leg counterterms are defined through the OS scheme, meaning that this cancellation only happens when the squared external momenta are set to the respective on-shell mass values. Therefore, these contributions have to be included as well (see also App. A.2).

In principle it is possible to consider the idea of altering the counterterms for δm and δZ of the external particles of the chosen decay process in the ZEM scheme such that the cancellation of leg corrections and leg counterterms takes place at $p^2 = 0$. But this would lead to problems with the cancellation of the UV divergences in the fully renormalized amplitudes, which are then renormalized with the normal OS scheme and a δv_S counterterm derived in this way. A more detailed discussion of this can be found in App. A.2.

With all this preparation, the counterterm of v_S in the ZEM scheme can be derived. The NLO contribution in Eq. (3.70) can again be expressed as the vertex correction and vertex counterterm, but now the leg corrections $\mathcal{A}_{\text{Leg}}$ have to considered as well. Thus, with the help of Eq. (A.37), the relation (3.70) can be written as

$$\begin{aligned} 0 = {} & \text{Re}\left(\mathcal{A}^{h_i \to AA}_{\text{VC}}(\{p^2 = 0\}) + \mathcal{A}^{h_i \to AA}_{\text{Leg}}(\{p^2 = 0\})\right), \\ & + \lambda_{h_iAA}\left(-\frac{\delta\lambda_{h_iAA}}{\lambda_{h_iAA}} + \delta Z_A + \frac{\delta Z_{h_ih_i}}{2} + \frac{\delta m_{h_i}^2}{m_{h_i}^2} + \frac{2\delta m_A^2}{m_A^2} + \frac{\lambda_{h_jAA}}{\lambda_{h_iAA}}\frac{m_{h_i}^2}{m_{h_j}^2}\frac{\delta Z_{h_ih_j}}{2}\right). \end{aligned} \tag{3.71}$$

Again, this equation can be solved for the two processes $h_1 \longrightarrow AA$ and $h_2 \longrightarrow AA$ to obtain the counterterms

$$\boxed{\begin{aligned}
\delta v_S^{\text{ZEM},h_1\to AA} &= v_S \left(-\text{Re}\left(\frac{\mathcal{A}_{\text{VC}}^{h_1\to AA}(\{p^2=0\}) + \mathcal{A}_{\text{Leg}}^{h_1\to AA}(\{p^2=0\})}{\lambda_{h_1AA}} \right)\right. \\
&\qquad \left. + \cot(\alpha)\delta\alpha - \delta Z_A - \frac{2\delta m_A^2}{m_A^2} - \frac{\delta Z_{h_1h_1}}{2} - \cot(\alpha)\frac{\delta Z_{h_1h_2}}{2} \right) \qquad (3.72a) \\
\delta v_S^{\text{ZEM},h_2\to AA} &= v_S \left(-\text{Re}\left(\frac{\mathcal{A}_{\text{VC}}^{h_2\to AA}(\{p^2=0\}) + \mathcal{A}_{\text{Leg}}^{h_2\to AA}(\{p^2=0\})}{\lambda_{h_2AA}} \right)\right. \\
&\qquad \left. - \tan(\alpha)\delta\alpha - \delta Z_A - \frac{2\delta m_A^2}{m_A^2} - \frac{\delta Z_{h_2h_2}}{2} - \tan(\alpha)\frac{\delta Z_{h_2h_1}}{2} \right). \qquad (3.72b)
\end{aligned}}$$

With this result there are two major questions: Do these counterterms lead to a UV-finite and gauge-independent amplitude overall? Both questions are quite subtle and need careful examinations.

First of all, the gauge dependence is addressed. As already mentioned, the overall renormalized amplitude should be gauge-independent and with the process-dependent scheme used for δv_S this is achieved. Furthermore, in the process-dependent scheme δv_S is by itself already gauge-independent. If for the v_S counterterm now the ZEM scheme is used and nothing else is changed, the v_S counterterm derived by the ZEM scheme also has to be gauge-independent by itself. Otherwise a gauge dependence in the overall amplitude would be introduced. Therefore a careful consideration of all contributions to δv_S has to be made.

Looking at Eq. (3.72) different contributions and counterterms have to be examined with respect to their gauge dependence. First of all, it was found that the combination of $\mathcal{A}_{\text{VC}}^{h_i\to AA}(\{p^2=0\}) + \mathcal{A}_{\text{Leg}}^{h_i\to AA}(\{p^2=0\})$ is by itself gauge-independent, i.e. the combination of vertex corrections and leg corrections of the two chosen processes with squared external momenta set to zero does not introduce a gauge dependence in Eq. (3.72). Next, the usage of the pinched scheme for $\delta\alpha$ results in a gauge-independent counterterm of α. Furthermore, the overall tadpole self-energy of the field A is already by itself gauge-independent and thus the derived quantities δm_A^2 and δZ_A are gauge-independent.

Thus, the only terms which might introduce a gauge dependence in δv_S are

$$\frac{\delta Z_{h_ih_i}}{2} + \frac{\lambda_j}{\lambda_i}\frac{m_{h_i}^2}{m_{h_j}^2}\frac{\delta Z_{h_ih_j}}{2}, \qquad (3.73)$$

for the respective processes $h_i \longrightarrow AA$. It was found that this combination is gauge-dependent. The ZEM scheme implemented in this way will lead to a gauge-dependent δv_S

and to a gauge-dependent overall amplitude of the desired decay process calculated in this thesis.

Several approaches have been considered to circumvent this problem (for a more detailed discussion, see App. A.2) but so far only one solution was found, namely changing the appearing field strength renormalization constants δZ in the Eqs. (3.72) by using pinched self-energies for their derivation instead of tadpole self-energies. By doing this, the field strength renormalization constants are already gauge-independent by themselves and the overall counterterm for δv_S is gauge-independent as well. This change in the $\delta Z_{h_i h_j}$, however, is only applied to terms appearing in the defining Eqs. (3.72) of the ZEM counterterms of v_S, not anywhere else. Otherwise, a gauge dependence in the overall amplitude of the renormalized process considered in this thesis might be reintroduced. Therefore, the resulting counterterms for v_S in this modified ZEM scheme read

$$\begin{aligned}\delta v_S^{\mathrm{ZEMGI},h_1\to AA} &= v_S \Bigg(-\mathrm{Re}\left(\frac{\mathcal{A}_{\mathrm{VC}}^{h_1\to AA}(\{p^2=0\}) + \mathcal{A}_{\mathrm{Leg}}^{h_1\to AA}(\{p^2=0\})}{\lambda_{h_1 AA}} \right) \\ &\qquad + \cot(\alpha)\delta\alpha - \delta Z_A - \frac{2\delta m_A^2}{m_A^2} - \frac{\delta Z_{h_1 h_1}^{\mathrm{pinched}}}{2} - \tan(\alpha)\frac{\delta Z_{h_1 h_2}^{\mathrm{pinched}}}{2} \Bigg) \end{aligned} \tag{3.74a}$$

$$\begin{aligned}\delta v_S^{\mathrm{ZEMGI},h_2\to AA} &= v_S \Bigg(-\mathrm{Re}\left(\frac{\mathcal{A}_{\mathrm{VC}}^{h_2\to AA}(\{p^2=0\}) + \mathcal{A}_{\mathrm{Leg}}^{h_2\to AA}(\{p^2=0\})}{\lambda_{h_2 AA}} \right) \\ &\qquad - \tan(\alpha)\delta\alpha - \delta Z_A - \frac{2\delta m_A^2}{m_A^2} - \frac{\delta Z_{h_2 h_2}^{\mathrm{pinched}}}{2} - \tan(\alpha)\frac{\delta Z_{h_2 h_1}^{\mathrm{pinched}}}{2} \Bigg) . \end{aligned} \tag{3.74b}$$

It is clear that this solution of the problem is somewhat unsatisfying, as it is a ‘by hand’ solution of the problem only after the problem was discovered. It would be preferable in the future that an optimized version of the ZEM scheme would be found such that both the kinematic constraints from the process-dependent scheme and this additional gauge dependence can be avoided in a more elegant way.

4. Higgs Decay into Dark Matter

In this chapter the computation of the decay of the $125\,\mathrm{GeV}$ Higgs boson (h_{125}) into two dark matter particles A is presented in detail. This process is especially interesting since it it is probed for at the LHC [40]. Since the generated DM particles are stable and do not interact with the other SM particles, they would leave the experiment undetected and therefore result in e.g missing total energy. Thus, the theoretically obtained result can be compared with current experimental limits. To obtain an even better result the total EW NLO decay width of the $125\,\mathrm{GeV}$ Higgs in the CxSM would be required. This calculation, however would exceed the scope of this thesis but may be calculated in future works.

For the computation of the decay width, first of all the contributing diagrams have to be derived and then calculated. In the next section the program tools used to calculate the Feynman diagrams of the process $h_{125} \to AA$ are introduced. The kinematics of the process and the general formula for the decay width of a given process are are discussed (Sec. 4.2) and the two different scenarios, with the h_{125} Higgs boson being either the lighter or the heavier particle of the two mixing scalars are presented (Sec. 4.3). Then, the LO calculation (Sec. 4.4) and the NLO calculation (Sec. 4.5) are discussed in detail to obtain the final analytic result. The numerical analysis of this result is given in Chapter 5.

4.1. Calculation Procedure

In this part the general procedure to obtain the analytic result for the LO and NLO decay width is discussed. Since the amount of Feynman diagrams in a NLO calculation can become quite large, computational tools are used to obtain and calculate all contributing diagrams. A general overview of the used programs is given in Fig. 4.1.

First of all, a model file is needed, which describes the used model with all interactions and input parameters. There are a number of programs which allow to create a model file. For this thesis, however, the Mathematica package SARAH was used [82–85]. SARAH is specifically designed for the task to extend the scalar sector of the SM, both with supersymmetric (SUSY) and non-super-symmetric models. Using the SM model file as an input template, all additional symmetries of the scalar potential have to be given and the additional scalar fields have to be defined. SARAH then calculates all possible interactions and generates a model file which can then be used by other programs.

With the model file of SARAH, all contributing Feynman diagrams can be obtained. For this step the Mathematica package FeynArts was used [86]. FeynArts uses the generated model file as input and generates all Feynman diagrams, which contribute to a chosen

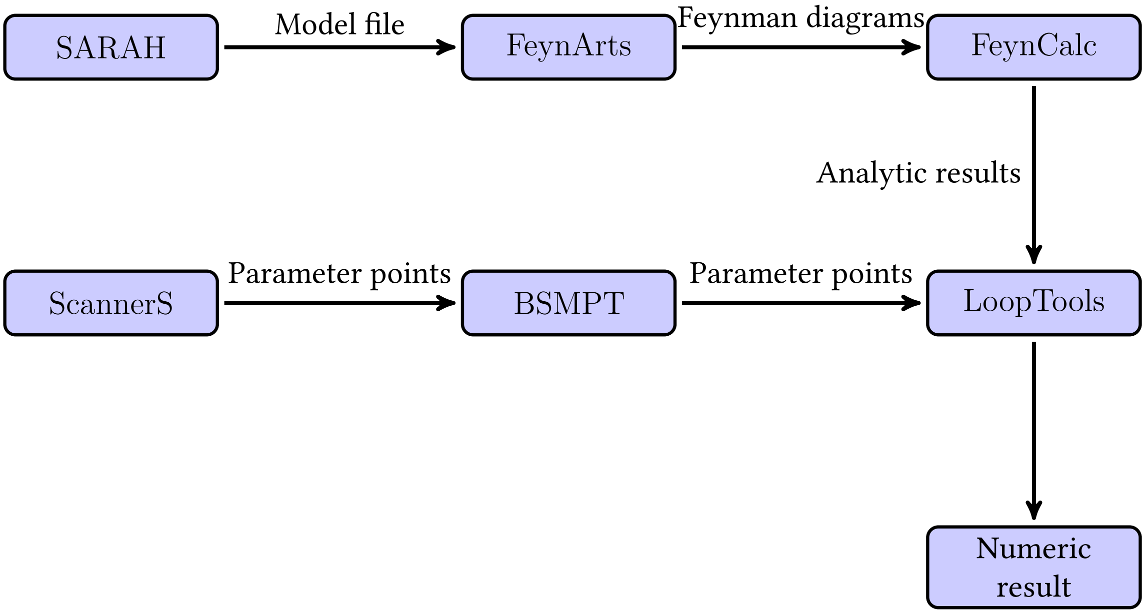

Figure 4.1.: Program chain to calculate the Feynman diagrams and obtain numeric results.

process. The used gauge parameters also have to be set in FeynArts (the model file of SARAH is provided in the general R_ξ gauge), but since the overall result at the end was checked to be gauge-independent no specific gauge was set (otherwise FeynArts would use Feynman gauge). At the end, FeynArts also translates the generated diagrams into general amplitudes, which then need further steps to obtain an analytic result.

The next Mathematica package, FeynCalc [87–89], takes the generated amplitudes from FeynArts and further simplifies them. The integrals in the amplitudes can be reduced to the Passarino-Veltman basis [90] and possible Lorentz and polarization structures of the amplitudes can be evaluated. Finally, a complete analytic result is obtained.

The analytic result can also be turned into a numeric result with the help of the Mathematica package LoopTools [91], where the integrals in the analytic results can be evaluated numerically. Moreover, LoopTools uses a finite value for the divergent term Δ_ϵ which can be set to different values. At the end, the UV-finite result should be independent of the value for this term. Thus, by choosing different values and checking if the result changes, the numeric result can be checked for UV-finiteness. The same procedure can also be applied for the gauge parameters and the numeric result can be checked for gauge independence.

To obtain numeric results, however, input parameters have to be chosen. They are generated and checked with the programs ScannerS [37, 39, 44] and BSMPT [92, 93], which are described in Sec. 5.2. For all generated parameter points the numeric result can then be calculated and discussed. The presentation of these results is given in Sec. 5.4.

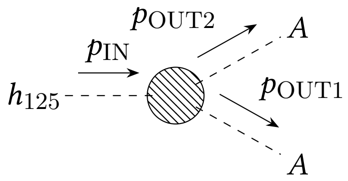

Figure 4.2.: Kinematics of the process $h_{125} \longrightarrow AA$.

4.2. Kinematics

In this section the kinematics of the process $h_{125} \longrightarrow AA$ and the general formula for the decay width are given. In Fig. 4.2 the general description of the external momenta of all particles in the decay $h_{125} \longrightarrow AA$ is given. First of all, the process is considered to be on-shell, i.e. all external momenta obey the relations

$$p_{\mathrm{IN}}^2 = m_{h_{125}}^2,\ p_{\mathrm{OUT1}}^2 = p_{\mathrm{OUT2}}^2 = m_A^2, \tag{4.1}$$

where $m_{h_{125}}^2$ is mass squared of the $125\,\mathrm{GeV}$ Higgs boson. Moreover, since energy-momentum conservation has to hold, i.e.

$$p_{\mathrm{IN}} = p_{\mathrm{OUT1}} + p_{\mathrm{OUT2}}, \tag{4.2}$$

all scalar products of combinations of external momenta can be determined. They read

$$p_{\mathrm{IN}} \cdot p_{\mathrm{OUT1}} = \frac{m_{h_{125}}^2}{2}, \tag{4.3a}$$

$$p_{\mathrm{IN}} \cdot p_{\mathrm{OUT2}} = \frac{m_{h_{125}}^2}{2}, \tag{4.3b}$$

$$p_{\mathrm{OUT1}} \cdot p_{\mathrm{OUT2}} = \frac{m_{h_{125}}^2 - 2m_A^2}{2}. \tag{4.3c}$$

With the general kinematics determined, the question arises how the decay width of a certain process is determined. The general formula for the decay width up to NLO of a general process $f_1 \longrightarrow f_2 f_3$ can be taken from literature, e.g. [42, 94], and reads

$$\Gamma^{\mathrm{NLO}}_{f_1\to f_2 f_3} = S\frac{\lambda(m_1^2, m_2^2, m_3^2)}{16\pi m_1^3} \sum_{\mathrm{d.o.f}} \left(|\mathcal{A}^{\mathrm{LO}}_{f_1\to f_2 f_3}|^2 + 2\mathrm{Re}\left[\left(\mathcal{A}^{\mathrm{LO}}_{f_1\to f_2 f_3}\right)^* \mathcal{A}^{\mathrm{NLO}}_{f_1\to f_2 f_3} \right] \right), \tag{4.4}$$

where $\mathcal{A}^{\mathrm{LO}}_{f_1\to f_2 f_3}$ denotes the overall amplitude of all Feynman diagrams contributing to the process at LO and $\mathcal{A}^{\mathrm{NLO}}_{f_1\to f_2 f_3}$ all Feynman diagrams contributing at NLO. These contributions have to be summed over all degrees of freedom (d.o.f.), i.e. the different polarization and chirality states of the external particles (if this is not measured in the experiment), and multiplied with the given pre-factor, where λ is the Källén-function [95], the m_i are the masses of the respective particles f_i and S is the symmetry factor of the chosen process. In the case of the process $h_{125} \to AA$ the decay width simplifies to

$$\Gamma^{\mathrm{NLO}}_{h_{125}\to AA} = \frac{\lambda(m^2_{h_{125}}, m^2_A, m^2_A)}{32\pi m^3_{h_{125}}} \left(\left| \mathcal{A}^{\mathrm{LO}}_{h_{125}\to AA} \right|^2 + 2\mathrm{Re}\left(\left(\mathcal{A}^{\mathrm{LO}}_{h_{125}\to AA} \right)^* \mathcal{A}^{\mathrm{NLO}}_{h_{125}\to AA} \right) \right), \tag{4.5}$$

since all external particles are scalars without additional polarization or chirality structure and the final particles are identical, thus $S = \frac{1}{2}$.

The LO decay width is the same expression but without the NLO contribution and therefore reads

$$\Gamma^{\mathrm{LO}}_{h_{125}\to AA} = \frac{\lambda(m^2_{h_{125}}, m^2_A, m^2_A)}{32\pi m^3_{h_{125}}} \left| \mathcal{A}^{\mathrm{LO}}_{h_{125}\to AA} \right|^2 . \tag{4.6}$$

4.3. Mass Ordering

Before the actual calculation of the LO and NLO contributions to the decay $h_{125} \to AA$ can take place, the implementation of the 125 GeV Higgs boson into the CxSM has to be specified.

In the CxSM, depending on the input values, either the lighter or the heavier of the two mixing scalars, h_1 or h_2, resembles the 125 GeV Higgs boson that behaves SM-like. The question now is how the fields and their respective masses are ordered in the CxSM. In general, the mass matrix and the corresponding rotation matrix with the mixing angle α are chosen such that m_{h_1} is always the lighter mass, i.e. that the relation

$$m_{h_1} < m_{h_2}, \tag{4.7}$$

holds. Therefore, there are two distinct scenarios, which have to be considered:

- $m_{h_1} = m_{h_{125}}$ (scenario I):
  The lighter of the 2 Higgs particles is the 125 GeV Higgs boson and therefore the process $h_1 \to AA$ for the calculation of the SM-like Higgs decay into DM particles has to be considered. Moreover, the process $h_2 \to AA$ will be chosen for the renormalization of v_S (cf. Sec. 3.5).

- $m_{h_2} = m_{h_{125}}$ (scenario II):
  The heavier of the 2 Higgs particles is the 125 GeV Higgs boson and therefore the process $h_2 \to AA$ for the calculation of the SM-like Higgs decay into DM particles has to be considered. Moreover, the process $h_1 \to AA$ will be chosen for the renormalization of v_S (cf. Sec. 3.5).

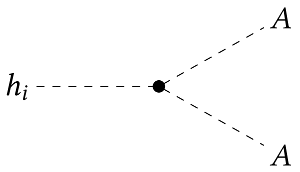

Figure 4.3.: The only diagram that contributes to the process $h_i \to AA$ at LO.

4.4. LO Calculation

With all the preparatory steps from the above sections taken, the calculation of the process $h_{125} \to AA$ can finally be discussed. First of all, the LO contribution of the process is calculated. At LO this is fairly simple as only one diagram contributes to the process, which can be seen in Fig. 4.3. The calculation of the amplitude is also straightforward. The amplitude simply consists of the respective coupling constant, which can be taken from Eq. (3.34), and reads

$$i\mathcal{A}^{\mathrm{LO}}_{h_i \to AA} = -i\lambda_{h_i AA}. \tag{4.8}$$

Thus, using Eq. (4.6), the decay widths for the processes $h_1 \to AA$ and $h_2 \to AA$ read

$$\boxed{\begin{aligned} \Gamma^{\mathrm{LO}}_{h_1 \to AA} &= \frac{s_\alpha^2 m_{h_{125}} \lambda(m^2_{h_{125}}, m_A^2, m_A^2)}{32\pi v_S^2}, & \text{(4.9a)} \\ \Gamma^{\mathrm{LO}}_{h_2 \to AA} &= \frac{c_\alpha^2 m_{h_{125}} \lambda(m^2_{h_{125}}, m_A^2, m_A^2)}{32\pi v_S^2}. & \text{(4.9b)} \end{aligned}}$$

In the LO calculation, the overall result is by itself already UV-finite as the divergences only occur in higher order corrections. Moreover, the result is obviously gauge-independent.

4.5. NLO Calculation

With the LO calculation finished, the NLO calculation can now be discussed. First of all, it is necessary to obtain all necessary contributions to the overall amplitude at NLO. As can be seen in Fig. 4.4, in general at NLO, there are vertex corrections, leg corrections, the vertex counterterm and the leg counterterms which have to be considered. However, since all external particles are considered to be on-shell, i.e. their squared momenta equals their squared masses, the leg corrections ($\mathcal{A}^{\mathrm{Leg,IN}}_{h_i \to AA}$ and $\mathcal{A}^{\mathrm{Leg,OUT}}_{h_i \to AA}$ in Fig. 4.4) are canceled by the leg counterterms ($\mathcal{A}^{\mathrm{LegCT,IN}}_{h_i \to AA}$ and $\mathcal{A}^{\mathrm{LegCT,OUT}}_{h_i \to AA}$). Therefore, only the vertex corrections ($\mathcal{A}^{\mathrm{VC}}_{h_i \to AA}$) and the vertex counterterm ($\mathcal{A}^{\mathrm{CT}}_{h_i \to AA}$) are of interest.

For the vertex corrections, all possible Feynman diagrams that contribute to the given process have to be generated and calculated. The corrections for the here discussed

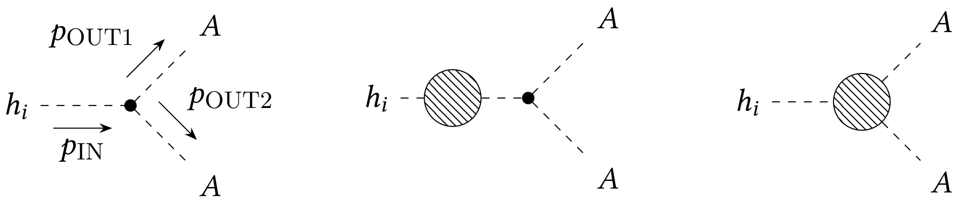

(a) Kinematics (b) $\mathcal{A}^{\text{Leg,IN}}_{h_i \to AA}$ (c) $\mathcal{A}^{\text{VC}}_{h_i \to AA}$

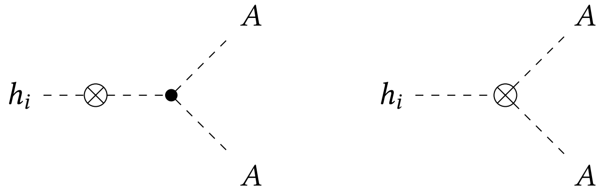

(d) $\mathcal{A}^{\text{LegCT,IN}}_{h_i \to AA}$ (e) $\mathcal{A}^{\text{CT}}_{h_i \to AA}$

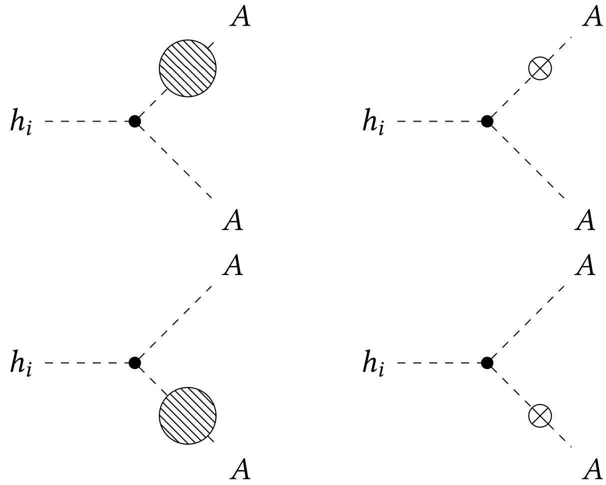

(f) $\mathcal{A}^{\text{Leg,OUT}}_{h_i \to AA}$ (g) $\mathcal{A}^{\text{LegCT,OUT}}_{h_i \to AA}$

Figure 4.4.: Generic diagrams contributing to the NLO decay width of $h_i \to AA$.

processes $h_i \to AA$ consist of the diagrams in Fig. 4.5. Next, the amplitudes of the diagrams have to be calculated and summed up. Moreover, the alternative tadpole scheme is used. Thus, all possible tadpole diagrams, which are given in Fig. 4.6, have to be added to the vertex corrections as well. This computation was done with the help of the programs already discussed in Sec. 4.1. At the end an analytical result for the vertex corrections $\mathcal{A}^{\text{VC}}_{h_i \to AA}$ is obtained.

The second part which needs closer consideration is the contribution of the vertex counterterm $\mathcal{A}^{\text{CT}}_{h_i \to AA}$. It can be derived as follows. Starting from the unrenormalized Lagrangian $\mathcal{L}_0$ with unrenormalized quantities, the Eqs. (3.4) and (3.6) for the fields and Eq. (3.2) for

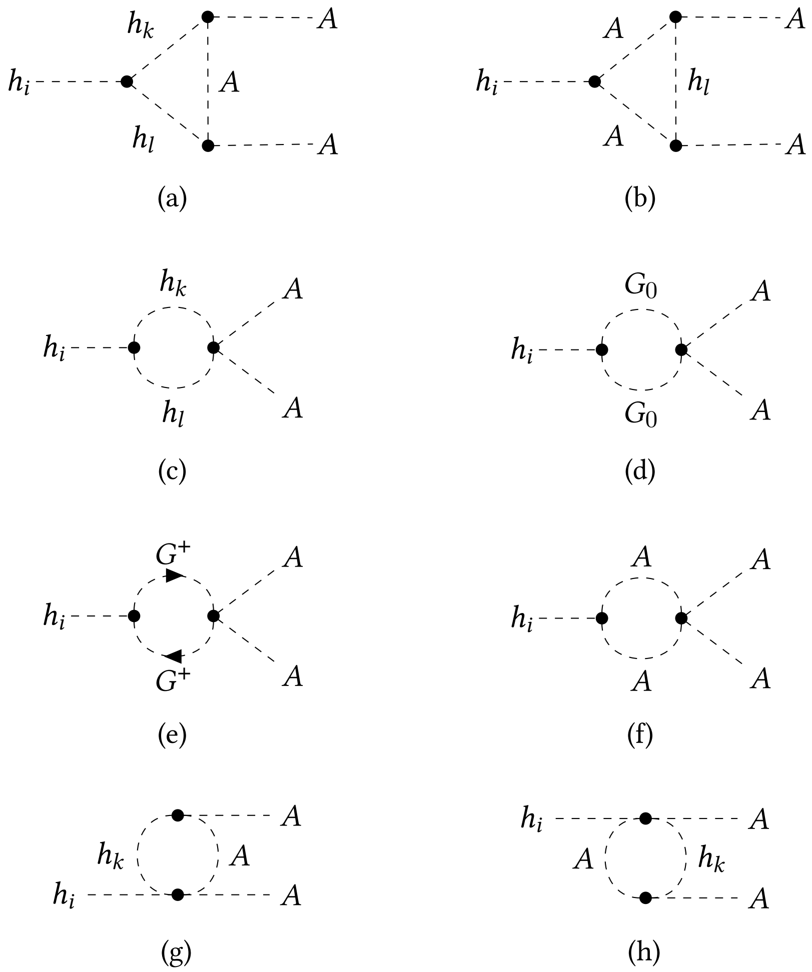

(a) (b) (c) (d) (e) (f) (g) (h)

Figure 4.5.: All Feynman diagrams contributing to the NLO vertex correction $\mathcal{A}^{\text{VC}}_{h_i \to AA}$, where $l, k \in \{1, 2\}$.

the coupling constant λ_{h_iAA} can be inserted,

$$\begin{aligned}
\mathcal{L}_0 \propto &- \lambda_{h_iAA,0} h_{i,0} A_0 A_0 - \lambda_{h_jAA,0} h_{j,0} A_0 A_0 \\
= &- (\lambda_{h_iAA} + \delta\lambda_{h_iAA}) \left(h_i + \frac{\delta Z_{h_ih_i}}{2} h_i + \frac{\delta Z_{h_ih_j}}{2} h_j \right) \left(A + \frac{\delta Z_A}{2} A \right) \left(A + \frac{\delta Z_A}{2} A \right) \\
&- (\lambda_{h_jAA} + \delta\lambda_{h_jAA}) \left(h_j + \frac{\delta Z_{h_jh_j}}{2} h_j + \frac{\delta Z_{h_jh_i}}{2} h_i \right) \left(A + \frac{\delta Z_A}{2} A \right) \left(A + \frac{\delta Z_A}{2} A \right) ,
\end{aligned} \tag{4.10}$$

where $i, j \in \{1, 2\}$ but $i \neq j$. Thus, the counterterm Lagrangian $\mathcal{L}^{\text{CT}}$ can be read of at NLO (i.e. terms with multiple counterterms are ignored) and is given by

$$\mathcal{L}^{\text{CT}} \propto -h_i A A \lambda_{h_iAA} \left(\frac{\delta\lambda_{h_iAA}}{\lambda_{h_iAA}} + \frac{\delta Z_{h_ih_i}}{2} + \delta Z_A + \frac{\lambda_{h_jAA}}{\lambda_{h_iAA}} \frac{\delta Z h_j h_i}{2} \right) . \tag{4.11}$$

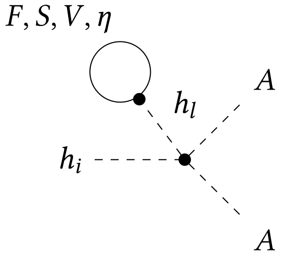

Figure 4.6.: All tadpole contributions that have to be added to the vertex corrections of the process $h_i \longrightarrow AA$ in the alternative tadpole scheme at NLO, with the index $l = 1, 2$. F denotes all fermions in the model, S the scalars h_1, h_2, A , as well as the Goldstone bosons G^0 and $G^{\pm}$. V denotes the massive gauge bosons Z and $W^{\pm}$, respectively and η denotes all ghosts η_Z and $\eta^{\pm}$.

Here only terms where the fields h_i and two times A occur, are selected. Thus, the vertex counterterm can be read off the Lagrangian and is given by

$$\mathcal{A}^{\mathrm{CT}}_{h_i \to AA} = -\lambda_{h_i AA} \left(\frac{\delta \lambda_{h_i AA}}{\lambda_{h_i AA}} + \delta Z_A + \frac{\delta Z_{h_i h_i}}{2} + \frac{\lambda_{h_j AA}}{\lambda_{h_i AA}} \frac{\delta Z_{h_j h_i}}{2} \right), \tag{4.12}$$

where $i, j \in \{1, 2\}$ but $i \neq j$. The counterterms for the coupling constants $\lambda_{h_i AA}$ have already been determined in Eq. (3.66). Thus, the overall NLO contributions for the processes $h_i \longrightarrow AA$ result in

$$\begin{aligned} \mathcal{A}^{\mathrm{NLO}}_{h_1 \to AA} = \mathcal{A}^{\mathrm{VC}}_{h_1 \to AA} - \lambda_{h_1 AA} \Bigg(& \frac{\delta m^2_{h_1}}{m^2_{h_1}} - \frac{\delta v_S}{v_S} + \cot(\alpha) \delta \alpha \\ & + \delta Z_A + \frac{\delta Z_{h_1 h_1}}{2} + \cot(\alpha) \frac{m^2_{h_2}}{m^2_{h_1}} \frac{\delta Z_{h_2 h_1}}{2} \Bigg), \end{aligned} \tag{4.13a}$$

$$\begin{aligned} \mathcal{A}^{\mathrm{NLO}}_{h_2 \to AA} = \mathcal{A}^{\mathrm{VC}}_{h_2 \to AA} - \lambda_{h_2 AA} \Bigg(& \frac{\delta m^2_{h_2}}{m^2_{h_2}} - \frac{\delta v_S}{v_S} + \cot(\alpha) \delta \alpha \\ & + \delta Z_A + \frac{\delta Z_{h_2 h_2}}{2} + \tan(\alpha) \frac{m^2_{h_1}}{m^2_{h_2}} \frac{\delta Z_{h_1 h_2}}{2} \Bigg). \end{aligned} \tag{4.13b}$$

With the NLO amplitude determined, the decay width of the respective processes can then be calculated with the help of Eq. (4.5). The exact analytic result now depends on the chosen renormalization schemes for the respective counterterms. First of all, only the alternative tadpole scheme (see Sec. 3.2.2) is used for the counterterms $\delta m^2_{h_i}$, $\delta Z_{h_i h_j}$ and $\delta Z_{h_i h_i}$. The usage of the standard tadpole scheme (see Sec. 3.2.1) does not lead to a gauge-independent overall amplitude. Only the alternative tadpole scheme in combination with the pinched scheme (see Sec. 3.4.2) results in a gauge-independent counterterm for α and moreover a gauge-independent result for the amplitude. Furthermore, in this thesis the process-dependent scheme (see Sec. 3.5.1) or the ZEM scheme (see Sec. 3.5.2) can be chosen for the renormalization of v_S as well as the p^* pinched scheme or the OS pinched scheme for the renormalization of α. All results are checked for their gauge-dependence and UV-finiteness analytically as well as numerically. The change in the scheme of $\delta\alpha$, however, does not change the result in these checks. In both schemes $\delta\alpha$ is already gauge-independent by construction and the UV-behavior does not change between the schemes, as it should be.

The analytical check for gauge dependence is quite straightforward. The decay width (or equivalently the NLO amplitude, since it is the only term with a potential gauge dependence) is calculated and all gauge-dependent terms are collected from the overall result, summed up and checked if the gauge dependence cancels. For both the process-dependent scheme and the modified ZEM scheme the overall result is gauge-independent.

The analytical check for the UV-finiteness of the result is more involved. The divergent parts of the given integrals have to be derived and inserted to check if at the end the overall sum of all divergent parts cancels. For this, the divergent parts of the integrals

$$\mathrm{Div}\left(A_0(m^2)\right) = m^2\Delta_\epsilon, \tag{4.14a}$$

$$\mathrm{Div}\left(B_0(p^2, m_1^2, m_2^2)\right) = \Delta_\epsilon, \tag{4.14b}$$

$$\mathrm{Div}\left(C_0(p_1^2, p_2^2, p_3^2, m_1^2, m_2^2, m_3^2)\right) = 0, \tag{4.14c}$$

$$\mathrm{Div}\left(DB_0(p^2, m_1^2, m_2^2)\right) = 0, \tag{4.14d}$$

have been used [71], where A_0, B_0, and C_0 are the respective 1-point, 2-point and 3-point functions, and DB_0 is the derivation of B_0 with respect to the momentum p^2. The expression for Δ_ϵ can be seen in Eq. (3.1). These equations can be implemented to obtain the UV-divergent parts of the overall amplitude. Again, this was checked for both the process-dependent scheme and the ZEM scheme derivation of δv_S and in both cases the overall result for the calculated NLO amplitude from Eq. (4.13) was UV-finite.

5. Numerical Evaluation

In this chapter the impact of the NLO corrections to the decay width of the process $h_{125} \to AA$, calculated in the previous chapter, is analyzed in detail. First, the used SM input parameters are listed (Sec. 5.1). Next, the generation of viable parameter points respecting theoretical and experimental constraints is explained (Sec. 5.2) and the generated parameter points are presented in several distributions (Sec. 5.3). Finally, the numeric result is calculated for all generated parameter points and further interpreted (Sec. 5.4).

5.1. Input Parameters

As a first step towards the numerical calculation, the input parameters have to be specified. Since OS renormalization is used to renormalize the CxSM, the fermion and gauge boson masses are part of the chosen input parameters. Furthermore, the electric charge e is needed to express the SM vev v together with mass parameters, see Eq. (2.21). All SM parameters have been taken from [96] and their values are given in Tab. 5.1. For simplicity, one generation of fermions is used in the calculation. The numerical impact of the fermions of the first two generations is negligible. The elementary charge can be obtained from the fine structure constant α_{EM}, which results in

$$\alpha_{\mathrm{EM}} = \frac{1}{137.035999084}, \tag{5.1a}$$

$$e = \sqrt{4\pi\alpha_{\mathrm{EM}}} = 0.3028221. \tag{5.1b}$$

The other free parameters of the model are generated and with the help of ScannerS as described in the next section.

Table 5.1.: All SM parameter values used in the numerical evaluation taken from [96].

SM parameter	Value
m_Z	91.1876 GeV
m_W	80.379 GeV
$m_{h_{125}}$	125.09 GeV
m_τ	1.777 GeV
m_b	4.7 GeV
m_t	172.5 GeV

Table 5.2.: The scanning range used for the generation of parameter points with ScannerS.

Parameter	Range	
	Lower	Upper
m_s	30 GeV	1000 GeV
m_A	10 GeV	62 GeV
v_S	1 GeV	1000 GeV
α	−1.57	1.57

5.2. Generation of Viable Parameter Points

In order to obtain physical results, viable parameter points are generated. These points have to obey certain theoretical and experimental constraints, as described in Sec. 2.5. In order to generate parameter points, the program ScannerS [37, 39, 44] is used. The CxSM model is already implemented in ScannerS. Points can be generated randomly (up to a starting seed) within a selected range for all given input parameters. ScannerS then checks if the model with the sampled input parameters obeys all theoretical and experimental constraints. Only parameter points that obey all criteria are saved. With this procedure about 1×10^6 parameter points have been sampled. The ranges for the input parameters can be seen in Tab. 5.2. The DM mass only ranges up to 62 GeV since the decay process $h_{125} \to AA$ has to be kinematically allowed.

The random selection of points has to be taken with caution. The absence of points in a certain region may have a physical reason but can also be the result of the random selection of points. Therefore, to be able to have reasonable results, the amount of generated parameter points has to be high and the randomization seed for each generation of points has to differ in order to not generate the same points again.

ScannerS uses a mass ordering for the scalar masses and the mixing angle is defined accordingly. Therefore, it is suitable to differ between the two scenarios where the 125 GeV Higgs is the lighter (scenario I) or heavier scalar particle (scenario II), as described in Sec. 4.3. In the following, the scalar mass not denoting the 125 GeV Higgs mass is written as m_s. Moreover, since only one scan for all mass ranges was made, scenario I will obtain more parameter points, since here the scalar mass m_s can vary from about 125 GeV up to 1000 GeV, whereas in scenario II it only varies between 30 GeV up to about 125 GeV (see also Tab. 5.2).

Another program called BSMPT [92, 93] is used to further refine the generated parameter points. BSMPT can be used to check whether the parameter points obey further constraints, e.g. if the vacuum is NLO stable, i.e. whether the LO minimum and the NLO minimum of the Higgs potential at zero temperature coincide. Furthermore, it can be checked if a strong first order EW phase transition can be obtained with the given input parameters. The CxSM model is already implemented in BSMPT, but in a more general form of the model than described here in this thesis. Therefore, the program code of the model was modified to include the CxSM version considered in this thesis. For this the definition of the effective potential and the counterterms had to be altered and the reading of the input parameters had to be adjusted. With this altered model, all generated parameter points from ScannerS have been checked with BSMPT. As a result, about 1000 parameter points have been rejected because they are not NLO stable. All other points passed all constraints from BSMPT, but no parameter point resulted in a strong first order EW phase transition.

The last constraint applied to the parameter points is the kinematic constraint from the process-dependent scheme, i.e. that the decay used in the process-dependent scheme is kinematically allowed (see also Sec. 3.5.1). Therefore, all points that do not obey this additional kinematic constraint are discarded when using the process-dependent scheme. In the ZEM scheme, however, this constraint is no longer present and all generated points are used.

5.3. Distribution of the Generated Parameter Points

As a first observation, the distribution of the generated parameter points is shown by plotting certain input parameters against each other. The correlation between the parameters imposed by the theoretical and experimental constraints is then visible. Besides the mass of the 125 GeV Higgs boson, there are 4 input parameters,

$$m_s, m_A, \alpha, v_S, \tag{5.2}$$

where m_s denotes the scalar mass of the non-125 GeV Higgs boson. Together with the two scenarios where the 125 GeV Higgs is either the lighter (scenario I) or the heavier (scenario II) scalar particle, this results in 12 possible plots. Furthermore, the kinematic constraint from the process-dependent scheme can be applied or not, so overall 24 different combinations are possible.

To start with, in Fig. 5.1 a few selected correlations are shown between α, v_S and m_s with the additional kinematic constraint. Since this constraint from the process-dependent scheme does not directly relate these parameters, the plots without the constraint are essentially identical. What can be see in these plots is that first of all, depending on which mass scenario is considered, the plots differ considerably.

Next, as can be seen in the upper row of the plots in Fig. 5.1, the parameters α and v_S seem to be strongly correlated and α is quite small in scenario I and close to $\pm\frac{\pi}{2}$ in scenario II. This is to be expected since all SM couplings to the h_{125} Higgs boson obtain an additional c_α in scenario I or s_α in scenario II. These couplings are very well measured and only small deviations are allowed. Thus, the additional factor has to be close to 1 and α has to be close to 0 or $\pm\frac{\pi}{2}$, respectively. Moreover, the parameters α and v_S are connected through the decay width of the 125 GeV Higgs boson into DM particles. As can be seen in Eq. (4.9), the LO decay width in scenario I is proportional to

$$\Gamma^{\text{LO}}_{h_1\to AA} \propto \frac{s_\alpha^2}{v_S^2}. \tag{5.3}$$

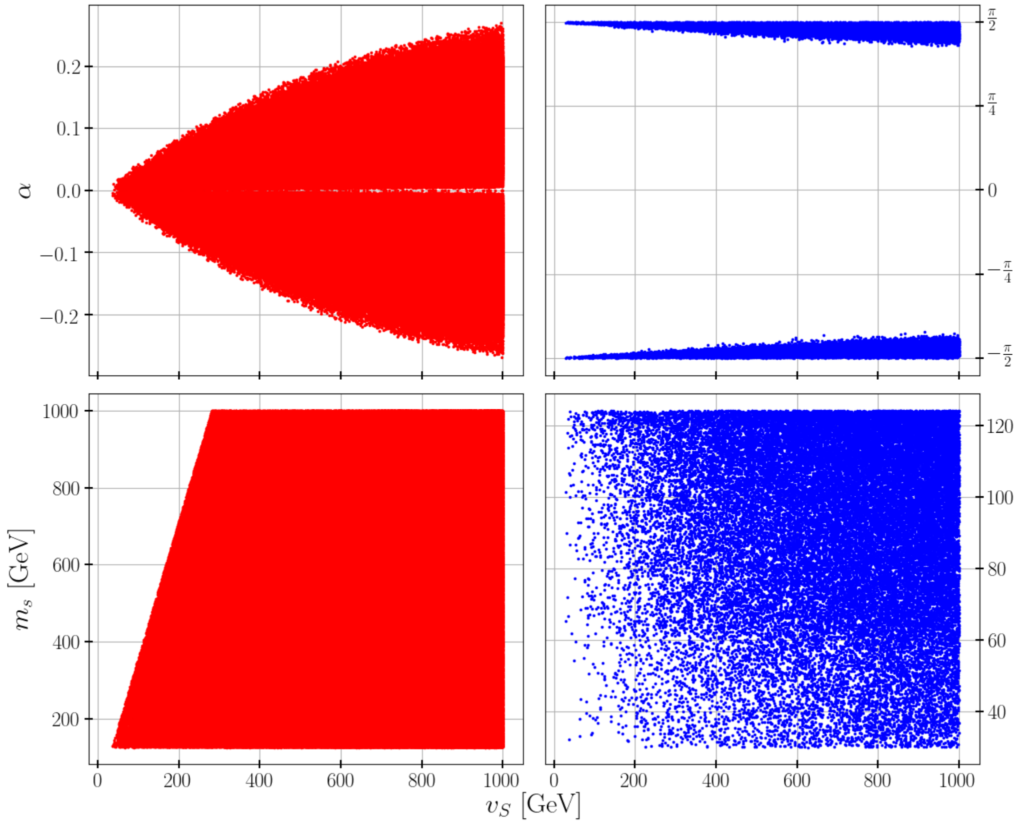

Figure 5.1.: The input parameters α plotted versus v_S in the upper row and m_s versus v_S in the lower row, where the red plots on the left side are the scenario where the 125 GeV Higgs is the lighter scalar particle and the blue plots on the right the heavier Higgs scenario. Here the process-dependent scheme constraint is also applied.

Thus, in order for the LO branching ratio of the 125 GeV Higgs into DM particles in the CxSM not to exceed experimental limits [40], this ratio has to be small. Therefore, if v_S is small, α has to be small. With increasing v_S, α can take up bigger values as well. This behavior can exactly be seen in Fig. 5.1.

In scenario II the LO decay width is proportional to

$$\Gamma^{\text{LO}}_{h_2\to AA} \propto \frac{c_\alpha^2}{v_S^2}. \tag{5.4}$$

Thus, for the same reasoning as in scenario II, this ratio has to be small. Therefore, if v_S is small, α has to be close to $\pm\frac{\pi}{2}$. This behavior can be seen in Fig. 5.1 as well.

The plots in the lower row in Fig. 5.1 show the relation between v_S and m_s in the two scenarios. In scenario I, as can be inferred from the plot, small values of v_S paired with large values of m_s are excluded, whereas in scenario II only the far left side of the plot is excluded. The relation in the scenarios can be explained as follows. The two parameters m_s and v_S can be related over the potential parameter d_2. in scenario I, m_s is equal to m_{h_2}. Furthermore, in this scenario α can be assumed to be close to zero. Thus, with the help of Eq. (2.20), d_2 can be written as

$$d_2 = \frac{m_{h_{125}}^2 + m_s^2 + \cos(2\alpha)(m_s^2 - m_{h_{125}}^2)}{v_S^2} \xrightarrow{\alpha \to 0} \frac{2m_s^2}{v_S^2}. \tag{5.5}$$

Next, the unitarity constraints from Sec. 2.5.1 are considered. More precisely, using again the small angle approximation in Eq. (2.20), λ and δ_2 can be expressed as

$$\lambda \xrightarrow{\alpha \to 0} \frac{m_{h_1}^2}{v_S^2} = \frac{m_{h_{125}}^2}{v_S^2}, \tag{5.6}$$

$$\delta_2 \xrightarrow{\alpha \to 0} 0. \tag{5.7}$$

With this simplified expressions the fourth constraint in Eq. (2.27) results in

$$\begin{aligned} \left|\frac{3}{2}\lambda + d_2 \pm \left(\frac{3}{2}\lambda - d_2\right)\right| &\leq 16\pi \\ \Rightarrow d_2 &\leq 8\pi. \end{aligned} \tag{5.8}$$

Here it is used that d_2 is positive. Inserting Eq. (5.5) for d_2 results in the relation

$$m_s \leq \sqrt{4\pi} v_S. \tag{5.9}$$

Thus, as it can be seen in Fig. 5.1 for scenario I, m_s and v_S are linearly related. Moreover, the prefactor given in the relation does indeed coincide with visual ratio given in Fig. 5.1.

The same calculation can be applied to scenario II. In this case, however m_s resembles the mass m_{h_1} and the angle α is close to $\pm\frac{\pi}{2}$. However, when both of these changes with respect to scenario I are applied, the same relation as in Eq. (5.9) is obtained. Therefore, m_s and v_S are again linearly related in scenario II. For example, setting m_s to the highest possible value in this scenario, i.e. about $125\,\mathrm{GeV}$, v_S has to be at least $35\,\mathrm{GeV}$. Therefore, only a small part of the parameter space is constrained by this result. Nevertheless, in Fig. 5.1 it can be seen that the far left side of the plot indeed contains no parameter points in scenario II.

Fig. 5.2 illustrates the parameter space spanned by m_s and m_A. Here all plots can be seen both with and without the additional constraints from the process-dependent scheme. Since these constraints directly relate the two masses, it is clear that the plots will differ considerably. In the points of scenario II, i.e. the blue points below $125\,\mathrm{GeV}$, the kinematic constraint on the masses is clearly visible. The upper left triangle is discarded if the constraint is used. However, the points in scenario I do not differ at all qualitatively. This

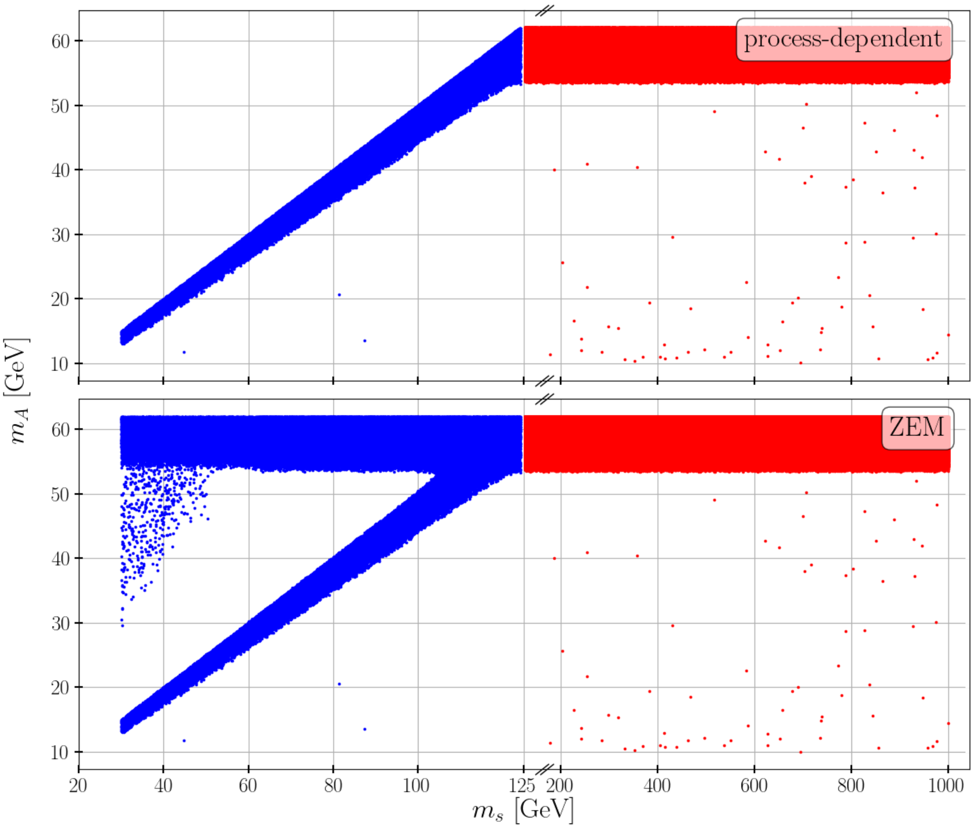

Figure 5.2.: The mass m_A plotted versus the other scalar mass m_s for $m_{h_{125}} \equiv m_{h_2}$ (the blue points on the left) and $m_{h_{125}} \equiv m_{h_1}$ (the red points on the right). Both plots with (upper) and without (lower) the additional constraint from the process-dependent scheme are shown.

is to be expected since in this case the scalar mass m_s is heavier than the 125 GeV Higgs boson mass and the additional constraint from the process-dependent scheme does not have an effect. The dark matter mass m_A always has to be 2 times smaller than the 125 GeV Higgs boson mass in order for the decay $h_{125} \to AA$ to be physically allowed.

Furthermore, it is interesting that in Fig. 5.2 in scenario I (red points) the DM mass m_A preferably has a mass value close to half of the 125 GeV mass is chosen for the parameter points, whereas in scenario II (blue points), m_A preferably has a value close to half of the other scalar mass m_s or close to half of $m_{h_{125}}$. This behavior, as will be seen, results from DM constraints applied on the DM mass m_A. To visualize the DM constraints, a test run to sample 2×10^5 parameter points has been performed, where the DM constraints were applied, but the parameter points which failed these constraints were also kept. The output can be seen in Fig. 5.3, where the points which do not obey the DM constraints are highlighted in green. Here, it can be clearly seen that the relations observed in Fig.

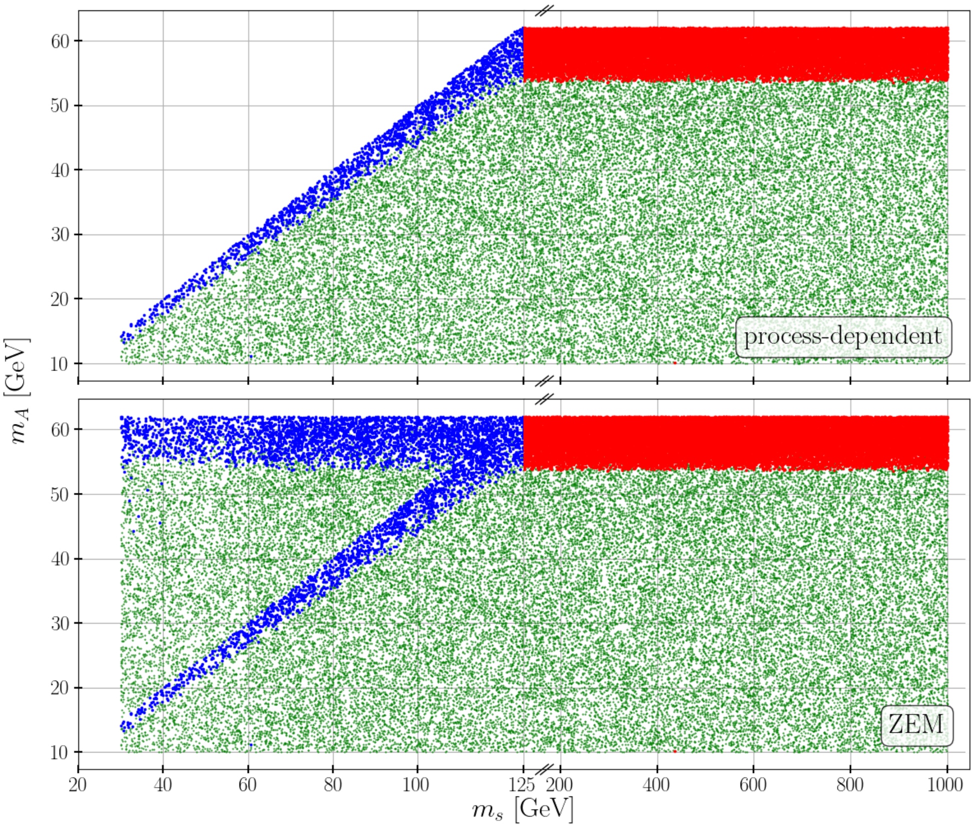

Figure 5.3.: The masses m_A and the other scalar mass m_s of the generated parameter points plotted against each other, where the red points indicate the scenario where the 125 GeV Higgs is the lighter scalar particle and the blue points the other scenario. The smaller green points are parameter points which would be rejected by DM constraints. For scenario I, only a fraction of the generated parameter points are shown for better visibility.

5.2 between the masses indeed are a result of the DM constraints. The reason for these constraints is the requirement that the relic density obtained in the CxSM must not exceed the observed value of the relic density. Therefore, the thermal annihilation processes of two DM particles A into one of the scalar particles h_i must be efficient enough (cf. [97]). This annihilation is enhanced close to the threshold, so that the DM mass m_A is preferably close to half of the 125 GeV mass or the other scalar mass m_s. Thus, the mentioned correlations can be seen in Fig. 5.2. However, there are still some points (although rare) where the processes involved in the computation of the relic density can be such that the relic density constraint is respected (cf. scattered points in 5.2 (lower)).

5.4. Numeric Results and Analysis

In the following, the numerical analysis of the process $h_{125} \to AA$ is performed, and the NLO decay width is calculated and presented for all generated parameter points. First, the analytically obtained result in Chapter 4 is also checked numerically in the following sense: Valid input parameters are inserted into the analytic result for the NLO decay width (Eq. (4.5)) and LoopTools is used to obtain a numeric result. The output can then be checked for its UV-finiteness and gauge dependence. LoopTools sets the parameter Δ_ϵ to a finite value. The overall result, however, should be independent of the chosen value in order for the expression to be UV-finite. Therefore by varying Δ_ϵ within LoopTools and comparing the different results the UV-finiteness of the given analytic result can be checked. The same procedure can be used for the check for gauge dependence. If the analytic result still has gauge parameters in it, they can be set to different values and compared whether the result changes. Thus, the NLO decay width is also checked in a numerical way and it is indeed found that the calculated expression is gauge-independent as well as UV-finite.

For all valid generated parameter points, the LO and NLO decay width is calculated (Eqs. (4.5) and (4.6)). The points are divided in two groups according to which mass ordering they belong (cf. Sec. 4.3), i.e. whether the $125\,\mathrm{GeV}$ Higgs is the heavier or lighter scalar particle. Moreover, for the counterterms $\delta\alpha$ and δv_S, two schemes can be chosen so that in total four different results can be obtained: the p^* pinched scheme with the process-dependent scheme, the p^* pinched scheme with the ZEM scheme, the OS pinched scheme with the process-dependent scheme, and the OS pinched scheme with the ZEM scheme. In all plots where the process-dependent scheme is chosen, the additional kinematic constraint from the scheme is also applied, whereas in the ZEM scheme this is not the case.

An interesting expression that is used in the following is the fraction between LO + NLO and LO decay width minus 1, which results in

$$\Delta\Gamma \equiv \frac{\Gamma^{\mathrm{NLO}}_{h_{125}\to AA}}{\Gamma^{\mathrm{LO}}_{h_{125}\to AA}} - 1 = \frac{2\mathrm{Re}\left(\mathcal{A}^{\mathrm{NLO}}_{h_{125}\to AA}\right)}{\mathcal{A}^{\mathrm{LO}}_{h_{125}\to AA}}. \tag{5.10}$$

Here it is used that the LO amplitude $\mathcal{A}^{\mathrm{LO}}_{h_{125}\to AA}$ is real (see Sec. 4.4). This quantity describes the relative contribution of the NLO contributions to the overall result with respect to the LO contributions and therefore measures how much the result for the decay width changes when going to NLO with respect to the LO result.

To start the numerical analysis, the relative contribution $\Delta\Gamma$ is plotted versus the LO decay width in Fig. 5.4 for scenario I, i.e. for the process $h_1 \to AA$. First of all, the LO decay width of course does not depend on the chosen renormalization scheme. The NLO decay width, however, and therefore $\Delta\Gamma$ can take different values for different renormalization schemes. The relative difference of the NLO decay widths between different renormalization schemes has been calculated and resulted in only a few percent. This result, however, has to be taken with caution. When the renormalization scheme is changed, the input parameters have to be properly converted as well. This is achieved by using the renormalization group

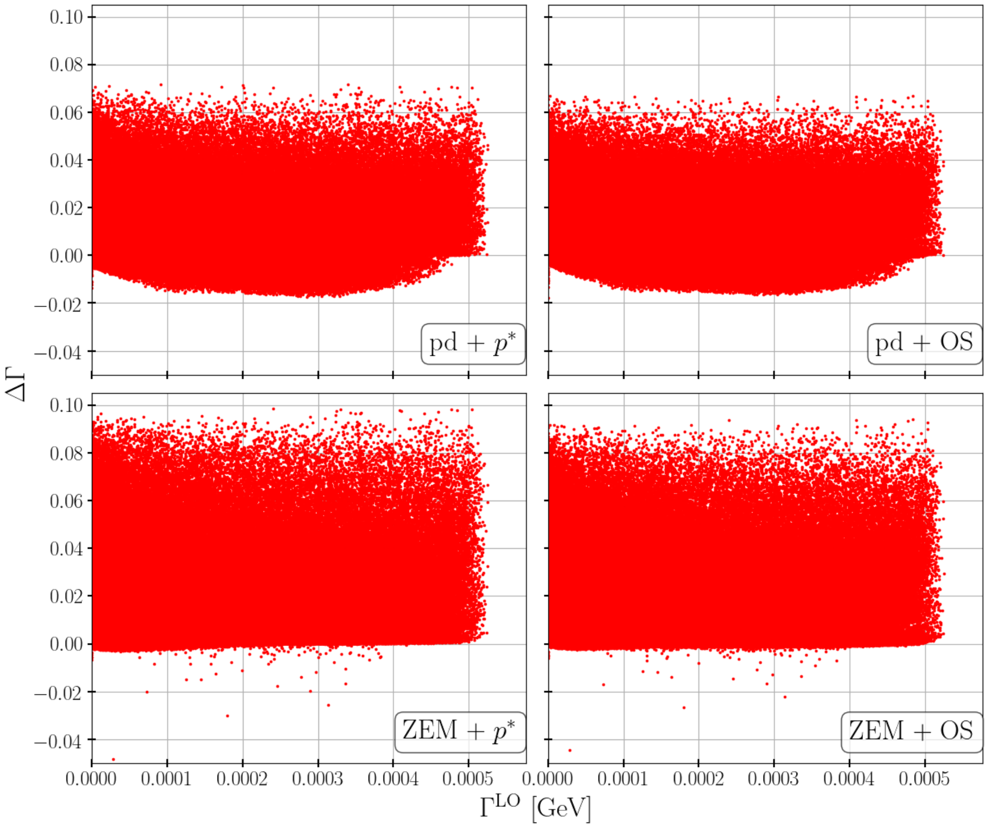

Figure 5.4.: $\Delta\Gamma$ (see Eq. (5.10)), plotted versus the LO decay width for the various renormalization schemes. Here only scenario I parameter points are shown, i.e. $h_1 \rightarrow AA$. In this and all following plots, pd, p^* and OS stand for the process-dependent, the p^* pinched and the OS pinched scheme.

equations (RGEs) [42], which need to be derived. This calculation would be beyond the scope of this thesis. Thus, only the rough approximation without parameter conversion was calculated. Moreover, the relative contribution of the NLO decay width to the overall result is quite small in all cases. Since the relative contribution in all schemes is always below $10\,\%$ in scenario I, all schemes can be seen as suitable in the context of a perturbative approach. Their NLO contributions do not become unacceptably large.

The same plots are also presented for scenario II in Fig. 5.5. The rough approximation, as mentioned in scenario I, has been calculated here as well and the relative difference between the renormalization schemes results in a few percent. Furthermore, as can be seen in Fig. 5.5, the relative contributions $\Delta\Gamma$ in the process-dependent scheme are again quite small. In the ZEM scheme, however, the relative contribution $\Delta\Gamma$ can go down to $-50\,\%$ and up to $10\,\%$, whereas in the process-dependent scheme, $\Delta\Gamma$ varies between about -3 to $3\,\%$. Thus, the ZEM scheme can result in relatively large corrections (in terms

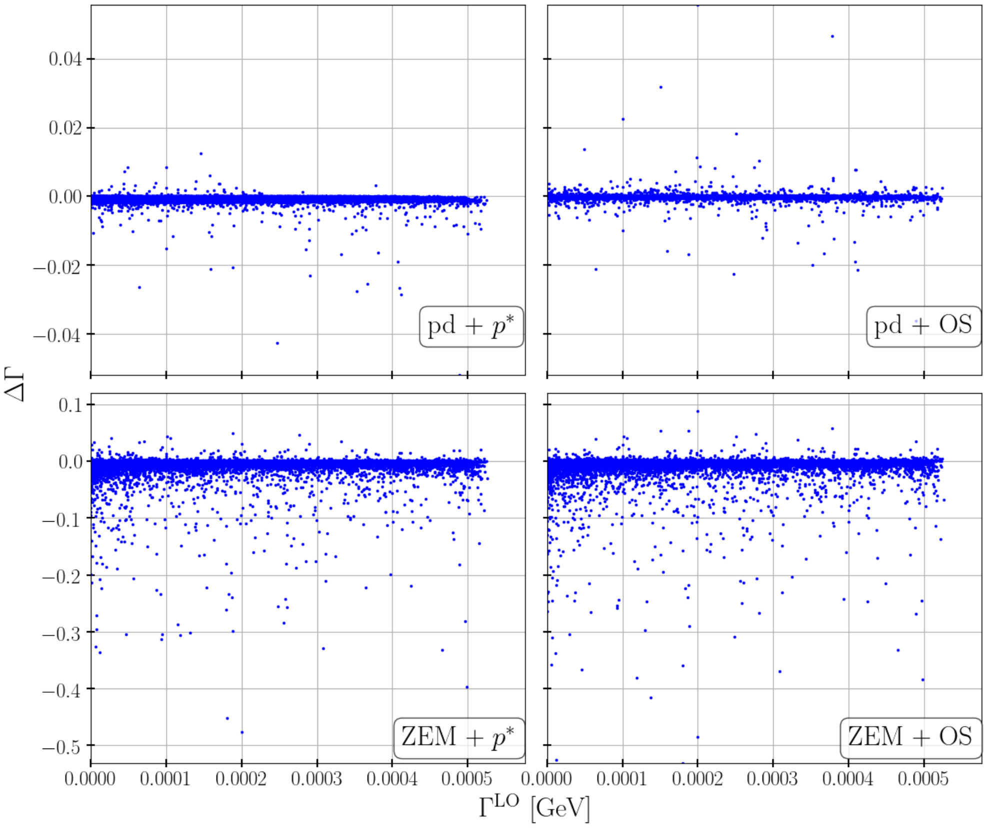

Figure 5.5.: $\Delta\Gamma$ (see Eq. (5.10)), plotted versus the LO decay width for the various renormalization schemes. Here only scenario II parameter points are shown, i.e. $h_2 \longrightarrow AA$.

of absolute values) at NLO. Thus, the numerical stability of the scheme can be doubted. These large corrections, however, only occur in a small amount of points. Thus, more generated parameter points would be necessary to come to a conclusion about the NLO stability of the ZEM scheme in this scenario. All other schemes are suitable schemes in scenario II, in the sense that they do not obtain unacceptably large NLO corrections.

Moreover, it is interesting that the difference between the renormalization schemes is only a few percent, whereas the value of the relative contributions $\Delta\Gamma$ strongly differ between ZEM and process-dependent scheme. In the calculation of the difference between the schemes, however, only points where the kinematic constraint of the process-dependent scheme was applied, have been used. Thus, it can be concluded that the ZEM scheme, in particular, can obtain quite large corrections $\Delta\Gamma$ with parameter points, which do not obey the kinematic constraint from the process-dependent scheme and are therefore only available in the ZEM scheme.

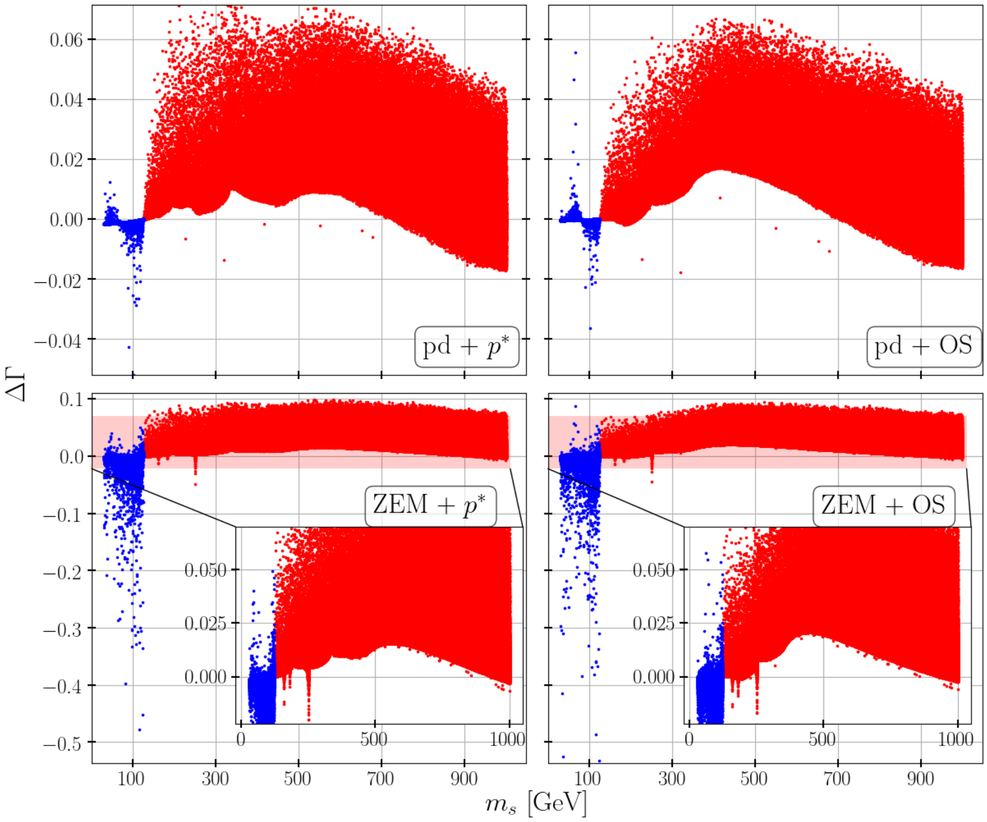

Figure 5.6.: ΔΓ (see Eq. (5.10)) plotted against the scalar mass m_s, where $h_{125} \equiv h_2$ (red points) and $h_{125} \equiv h_2$ (blue points). All different combinations of possible renormalization schemes are shown. Interesting sections (indicated by the red band) of the two plots in the second row are also shown in more detail.

Next, it can be seen by comparing the Figs. 5.4 and 5.5 that the majority of parameter points in scenario II, i.e. $h_2 \to AA$, when using the process-dependent scheme, result in a smaller relative contribution ΔΓ than the parameter points in scenario I. This difference can be further illustrated by plotting the relative contribution ΔΓ versus the varying mass m_s, as can be seen in Fig. 5.6. Here, several observations are made. First of all, the relative contributions in scenario II (blue points) are quite small in the process-dependent scheme, but become comparatively large in the ZEM scheme with respect to scenario I (red points). Moreover, the relative contribution with points from scenario I results in an interesting behavior, where several peaks at the bottom of the points can be seen. For this, in the plots of the ZEM scheme the important regions are also shown in more detail in Fig. 5.6 to visualize this behavior for the ZEM scheme as well. These peaks stem from the integrals occurring in the NLO result of the decay width. The scalar integrals, e.g. B_0 and C_0, have certain kinematic thresholds, which cause these sharp changes, when varying

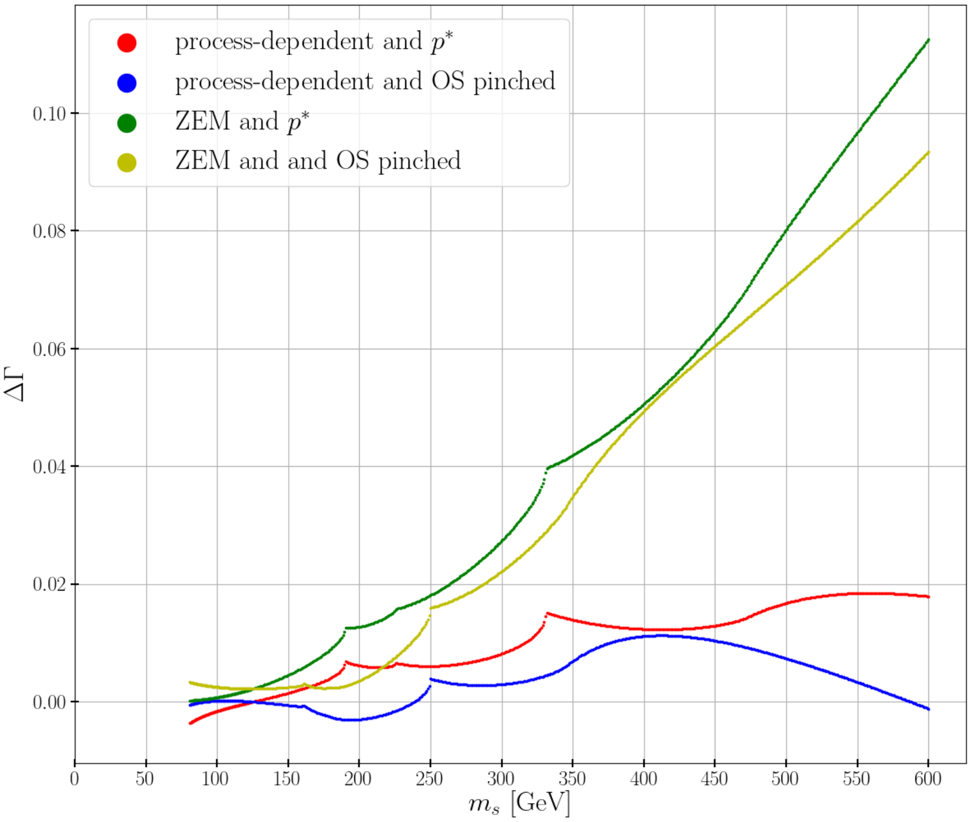

Figure 5.7.: $\Delta\Gamma$ (see Eq. (5.10)) plotted versus the scalar mass m_s, all other parameters have been set to fixed values, with $\alpha = 0.01$, $v_S = 100\,\text{GeV}$ and $m_A = 40\,\text{GeV}$. All possible combinations of renormalization schemes are shown.

the input scalar mass m_s. This observation can be illustrated, when plotting the relative contribution $\Delta\Gamma$ versus the scalar mass m_s, but leaving all other input parameters fixed, as can be seen in Fig. 5.7. The used parameters here, however, are not checked for theoretical or experimental constraints and are purely used for this illustration of the origin of the peaks. In Fig. 5.7 all possible renomalization schemes are shown and several peaks occur in all schemes. Moreover, when switching from the OS pinched scheme to the p^* pinched scheme the peaks shift as well. This is expected, since the self-energies in the two schemes used for the derivation of $\delta\alpha$ are evaluated at different scales, depending on which scheme is used. For example, a peak at around $250\,\text{GeV}$ can be seen in the OS scheme in Fig 5.7. This means that the according peak in the p^* pinched scheme can be calculated with

$$x_{\text{OS}} = 250\,\text{GeV},\; x_{\text{OS}}^2 = \frac{m_{h_{125}}^2 + x_{p^*}^2}{2}, \tag{5.11}$$

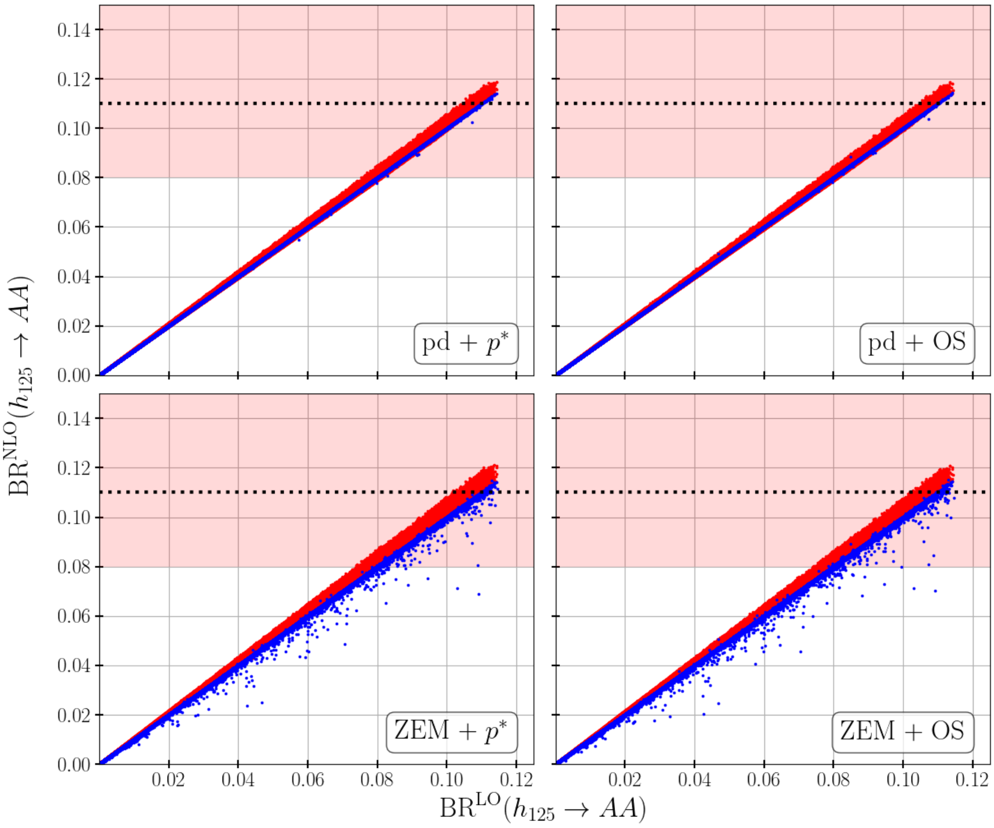

Figure 5.8.: The calculated branching ratios for the decay $h_{125} \longrightarrow AA$ at NLO versus LO for all generated parameter points and all renormalization schemes. The experimental limit is indicated by the dashed line with the uncertainty on the limit given with the red band (Eq. (5.12)). Red (blue) points correspond to scenario I (II).

since in the p^* pinched scheme the self-energies are evaluated at the mean of the scalar masses. This can be solved for x_{p^*} and results in about $330\,\mathrm{GeV}$, where indeed a peak in the p^* pinched scheme is visible in Fig. 5.7. They only occur in scenario I, because most of the SM masses occurring in the calculation (e.g. the W and Z boson mass) are of order $100\,\mathrm{GeV}$ and these thresholds of the integrals only occur at multiples of the input masses. Since in scenario I, m_s ranges up to $1000\,\mathrm{GeV}$ in the scans, these high masses can be reached.

As a final step in the numerical analysis, the obtained NLO result for the decay width of the process $h_{125} \longrightarrow AA$ is compared to experimental observations. The observed limit on the branching ratio of the $125\,\mathrm{GeV}$ Higgs decay into invisible particles is given by [40]

$$\mathrm{BR}(h_{125} \longrightarrow \text{invisible}) \lesssim 0.11^{+0.04}_{-0.03}, \tag{5.12}$$

at 95 % confidence level. This limit can now be used to further constrain the generated parameter points. In order to compare results, however, the calculated branching ratio is needed. Thus, the total decay width of the 125 GeV Higgs boson in the CxSM including NLO EW corrections has to be calculated. This may be achieved in future works, but for now an approximation is used. The total decay width of the 125 GeV Higgs boson in the SM without EW corrections[1] is taken from HDECAY [2] [98, 99] and is given by

$$\Gamma_{h_{125}}^{\text{SM,tot}} = 0.4068 \times 10^{-2}\,\text{GeV}. \tag{5.13}$$

In order to translate this decay width into the here used CxSM set-up it is multiplied with the appropriate squared angular factor k_i^2 (see Eq. (2.15)), that rescales all SM-like CxSM Higgs couplings to the SM particles (see Secs. 2.2 and 2.3), where the index i is chosen accordingly to the mass scenario. Moreover, to the translated decay width the additional decay that is possible in the CxSM, i.e. $h_{125} \to AA$, is added to obtain the total decay widths in the CxSM. The NLO value for this decay is added to obtain the approximate NLO expression for the branching ratio. Furthermore, in scenario II the 125 GeV Higgs boson is the heavier of the two scalar particles ($h_{125} \equiv h_2$). If the other scalar h_1 is light enough, the decay $h_2 \to h_1 h_1$ is also allowed and has to be added to the total decay width.

Thus, the LO and approximate NLO branching ratio of the decay $h_{125} \to AA$ is given by

$$\text{BR}_{\text{CxSM}}^{\text{NLO/LO}}(h_{125} \to AA) \approx \frac{\Gamma_{h_{125}\to AA}^{\text{NLO/LO}}}{k_i^2 \Gamma_{h_{125}}^{\text{SM,tot}} + \Gamma_{h_{125}\to AA}^{\text{NLO}} + \delta\,\Gamma_{h_{125}\to h_1 h_1}^{\text{LO}}}\,, \tag{5.14}$$

where δ is defined as

$$\delta = \begin{cases} 1, & m_{h_{125}} \geq 2m_s \\ 0, & m_{h_{125}} < 2m_s \end{cases} \,. \tag{5.15}$$

The factor δ ensures that the decay width of the process $h_{125} \to h_1 h_1$ is only added if it is kinematically allowed.

This expression is approximate in the sense that the NLO EW corrections are only included in the Higgs-to-invisible decay but not in the SM-like CxSM Higgs decays into SM particles. This approximation, however, is valid as long as the EW corrections to these decay widths are small enough compared to the EW corrections to $h_{125} \to AA$ [3]. Moreover, for a better approximation the NLO corrections to the decay $h_{125} \to h_1 h_1$ have to be included as well.

In Fig. 5.8 the calculated branching ratios for all generated parameter points can be seen. The experimental limit on the branching ratio is shown as well. However, the limit is only

---

[1] It includes, however, the relevant higher-order QCD corrections that can be taken over from the SM to the CxSM.

[2] In HDECAY the G_F scheme is used whereas in this thesis other input parameters have been chosen. This results in a small mismatch, but since an approximation in the calculation here is already applied, this can be neglected.

[3] From Ref. [100], where for the 2HDM and the N2HDM the EW corrections have been calculated for all the allowed parameter sets and in different renormalization schemes, it can be concluded that the EW corrections to the decay widths of the SM-like Higgs into SM particles amount up to a few percent only.

indicated for the NLO result, since the parameter points are generated with respect to the limit at LO. Thus, all LO results already fulfill this constraint.

Almost all parameter points result in a smaller value at NLO. Only about $0.2\,\%$ of the generated points result in a higher branching ratio than the experimental limit. The highest obtained branching ratio, however is around 0.121 and therefore still lies well within the experimental uncertainty. The relative change of the BR at NLO with respect to LO has been calculated and rises only up to 7-8 %. Thus, the NLO contributions to the branching ratio are too small to further constrain the model. Moreover, it is interesting to see that the points from scenario II result in smaller branching ratios, especially when using the ZEM scheme. This is to be expected, since many points in that scenario obtain negative relative NLO contributions to the decay width, see e.g. Fig. 5.5.

To conclude the numerical analysis: Including the NLO corrections to the decay width of the process $h_{125} \to AA$ does not further constrain the parameter space of the model with respect to current experimental limits. The calculated NLO branching ratios of all generated parameter points are within experimental bounds. Calculating the EW corrections to all decays of the SM-like CxSM Higgs boson into SM particles will improve the obtained result. Tighter experimental constraints, however, are needed to further constrain the CxSM model and may be obtained in the upcoming LHC run [41].

6. Conclusion

In this Master thesis, in the framework of the CxSM, the EW corrections to the decay process $h_{125} \rightarrow AA$ of the SM-like $125\,\mathrm{GeV}$ Higgs boson into two DM particles have been calculated and discussed. Despite the enormous success of the SM, there are still many unanswered questions in particle physics. The question about the nature of DM, in particular, has no suitable answer in form of a potential DM candidate within the SM. Therefore, BSM theories including a possible DM candidate are explored, with the CxSM being one of those theories. It is based on the extension of the SM by a complex singlet field, and in the version treated in this thesis exhibits one scalar particle representing the DM particle. Furthermore, the decay process of the $125\,\mathrm{GeV}$ Higgs into invisible particles is already probed at the LHC and experimental limits can be compared with theoretical precision results.

First, the CxSM model was presented. The scalar sector was thoroughly introduced and all differences with respect to the SM where mentioned. With the additional singlet and vev parameter in the model, minimization conditions of the scalar minimum were discussed. A set of parameters was presented that is mostly based on physical parameters. Additionally, the relevant theoretical and experimental constraints on the model were discussed.

After the description of the model, the renormalization of the CxSM was presented in great detail in the next chapter. A brief introduction into the general aspects of renormalization and regularization was given and the general OS scheme approach was introduced for the scalar fields. The importance of the treatment of tadpole contributions was clarified and two schemes were introduced to specify how the tadpole contributions have to be handled. With the standard tadpole scheme, however, no gauge-independent overall result could be achieved. Therefore, the alternative tadpole scheme, which was able to obtain gauge-independent results, was introduced, similar to earlier works. Next, the renormalization of the mixing angle α was covered. Here, two schemes were used, the KOSY scheme and the pinched scheme. The KOSY scheme would also lead to a gauge-dependent result, whereas the pinched scheme in combination with the alternative tadpole scheme would lead to an overall gauge-independent result. The last parameter to be renormalized was v_S, where the process-dependent scheme was used. In this scheme per definition a gauge-independent counterterm of v_S is obtained. In order to get rid of the additional kinematic constraints introduced by the process-dependent scheme, another scheme was implemented. The ZEM scheme does not introduce additional kinematic constraints, but will lead to gauge-dependent overall results. If modified accordingly it also allows to obtain an overall gauge-independent result.

After specifying the renormalization of the CxSM, the EW corrections to the decay process $h_{125} \rightarrow AA$ of the $125\,\mathrm{GeV}$ Higgs boson into two DM particles were calculated at NLO. The program tools used for the computation of the Feynman amplitudes as well as all relevant formulas were mentioned. The two scenarios for the mass-ordering of the scalar particles were introduced, i.e. whether the $125\,\mathrm{GeV}$ Higgs boson is the heavier or the lighter of the two scalar particles. Finally, the NLO calculation was presented and the relevant Feynman diagrams contributing to the LO and NLO processes were shown and computed. Some analytic tests were made, i.e. whether the overall result was gauge-independent and UV-finite.

The analytic result obtained for the LO and NLO decay widths of the process $h_{125} \to AA$ furthermore was evaluated numerically. For this task the program package LoopTools was used and the gauge independence and UV-finiteness of the result could also be checked numerically. For further analysis, the input parameters had to be specified. Roughly 1 Million parameter points were generated and checked with ScannerS and BSMPT, whether they obey the above mentioned theoretical and experimental constraints. The resulting correlation between the different input parameters was also visualized. Next, the decay width at LO and NLO was calculated for all generated parameter points and all different combinations of possible renormalization schemes were used. The obtained numerical results were presented and the differences between the renormalization schemes were discussed. Barring the uncertainty of the random generation of parameter points it can be concluded that all schemes lead to a numerically stable result in the sense that no unacceptably large corrections are obtained at NLO. The ZEM scheme can result in relatively large corrections, but only in a few of the generated points. Thus, to conclude the NLO stability in this regard, more generated points are needed to give a final answer. Furthermore, the resulting branching ratio for the decay process $h_{125} \to AA$ was compared to current experimental limits both at LO and NLO. All generated parameter points, however were not excluded by them, taking into account the current experimental limits.

In order to improve on the obtained results, the EW corrections to the total decay width of the $125\,\mathrm{GeV}$ Higgs boson in the CxSM at NLO can be computed by calculating the so far unknown EW corrections to the decay processes of the SM-like CxSM Higgs boson into SM particles. The improved result for the NLO EW branching ratio of the process $h_{125} \to AA$ can then be compared to the current experimental limits. Furthermore, the amount of generated parameter points can be further increased to obtain even better statistics and to look for points with a strong first order EW phase transition with BSMPT. Moreover, the ZEM scheme can be further improved to more elegantly obtain a gauge-independent result.

A. Appendix

A.1. The Pinch Technique in the CxSM

In order for the pinched scheme (see Sec. 3.4.2) to result in a gauge-independent counterterm of α, a gauge-independent form of the self-energies of the fields h_i, $i \in \{1, 2\}$, has to be obtained in an unambiguous way. This can be achieved with the pinch technique [76–80], which is described in the following for the CxSM. Similar derivations for other models have already been made and can be seen e.g. in [73, 74].

A short introduction into the general idea of the pinch technique is given, before the calculation for the CxSM is discussed. At first, a process has to be chosen from where the pinched self-energies can be extracted. The particles, in our case the scalars h_i, of whom the self-energies are to be pinched, have to be already present as internal particles at LO so that the self-energies will contribute at NLO. Therefore, a suitable process has to be chosen. Here the process $\mu^+\mu^- \longrightarrow \bar{b}b$ is considered, the annihilation of muons into a bottom-anti-bottom quark pair.

Next, the general approach is that the overall amplitude of that process is gauge-independent, i.e. that

$$\mathcal{A}^{\text{total}} = \mathcal{A}^{\text{box}}(\{\xi\}) + \mathcal{A}^{\text{tri}}(\{\xi\}) + \mathcal{A}^{\text{leg}}(\{\xi\}) + \mathcal{A}_{\text{self}}(\{\xi\}), \tag{A.1}$$

holds, with the respective box $\mathcal{A}^{\text{box}}$, triangle $\mathcal{A}^{\text{tri}}$, self-energy $\mathcal{A}^{\text{self}}$ diagrams as well as the external leg corrections $\mathcal{A}^{\text{leg}}$ and all occurring gauge parameters abbreviated with $\{\xi\}$. Since the overall amplitude is gauge-independent, the gauge dependence of the respective contributions have to cancel in total. Therefore, it is possible to rewrite them such that they can be attributed to other contributions, i.e. that the relation can be rewritten as

$$\mathcal{A}^{\text{total}} = \hat{\mathcal{A}}^{\text{box}} + \hat{\mathcal{A}}^{\text{tri}} + \hat{\mathcal{A}}^{\text{leg}} + \hat{\mathcal{A}}^{\text{self}}, \tag{A.2}$$

with adjusted contributions signaled by the hat, which are no longer gauge-dependent. Thus, gauge-independent self-energies can be generated.

The procedure in the pinch technique is now to rewrite the contributions from box and triangle diagrams as well as external leg contributions such that they are given in terms of self-energy contributions. This is achieved by 'pinching' out fermion propagators. More precisely, starting with a slashed loop momentum $\not{k}$ between fermion spinors in any of the calculation of the mentioned amplitudes, the momentum can be rewritten as

$$\not{k} = \not{k} + \not{p} - \not{p} + m - m = S^{-1}(k + p) - S^{-1}(p), \tag{A.3}$$

where $S^{-1}(p)$ is the inverse fermion propagator with momentum p (up to a factor i), defined as

$$S^{-1}(p) \equiv \not{p} - m. \tag{A.4}$$

Now the identities

$$S^{-1}(p)u(p) = 0, \tag{A.5a}$$

$$S^{-1}(-p)v(p) = 0, \tag{A.5b}$$

with the respective fermion spinors u and v, can be used so that the second propagator in Eq. (A.3) vanishes, whereas the first propagator cancels out with the inherent propagator of the considered amplitude. The fermion propagator thus is 'pinched' out. An example calculation is given later. This procedure has to be carried out consistently for all slashed loop momenta, which will result in gauge-independent pinched contributions. Moreover, the additional chirality structure from interactions with Z and W bosons further complicates the calculation.

Before the actual calculation can start, some useful definitions have to be mentioned. First of all, with the definition of

$$O_{ij} \equiv k_i k_j, \tag{A.6}$$

all couplings in the CxSM between scalar particles and SM particles can be described as

$$g_{XYh_i} = g^{\mathrm{SM}}_{XYH} k_i, \tag{A.7a}$$

$$g_{XYh_ih_j} = g^{\mathrm{SM}}_{XYHH} O_{ij}, \tag{A.7b}$$

where g^{SM}_{XYH} and g^{SM}_{XYHH} are the respective coupling constants between the SM particles X and Y and one or two SM Higgs particles and k_i is given in Eq. (2.15). Thus, using these expressions the SM Feynman rules can be taken, cf. e.g. Ref. [43]. Next the chirality projection operators are written as

$$P_{\mathrm{R/L}} = \frac{1 \pm \gamma_5}{2}, \tag{A.8}$$

with the Dirac matrix γ_5. In the following, also the notation

$$\int_k \equiv \int \mathrm{d}^4 k \tag{A.9}$$

is used, to denote the loop integrals. Here, the integrals are in 4 dimensions and are so far not yet regulated. The pinch technique can be applied before any regularization takes place. Next the integral definitions

$$\frac{i}{16\pi^2}A_0(m^2) \equiv \int_k \frac{1}{k^2 - m^2}, \tag{A.10a}$$

$$\frac{i}{16\pi^2}B_0(p^2, m_1^2, m_2^2) \equiv \int_k \frac{1}{(k^2 - m_1^2)((k+p)^2 - m_2^2)}, \tag{A.10b}$$

$$\frac{i}{16\pi^2}\alpha_V \equiv \int_k \frac{1}{(k^2 - m_V^2)(k^2 - \xi_V m_V^2)}, \tag{A.10c}$$

$$\frac{i}{16\pi^2}\beta_{V_1V_2}(p^2) \equiv \int_k \frac{1}{(k^2 - m_{V_1}^2)(k^2 - \xi_{V_1} m_{V_1}^2)((k+p)^2 - m_{V_2}^2)}, \tag{A.10d}$$

$$\frac{i}{16\pi^2}\beta_{V_1\xi_{V_2}V_2}(p^2) \equiv \int_k \frac{1}{(k^2 - m_{V_1}^2)(k^2 - \xi_{V_1} m_{V_1}^2)((k+p)^2 - \xi_{V_2} m_{V_2}^2)}, \tag{A.10e}$$

are useful, with ξ_V being the gauge parameter of the corresponding gauge boson V. Moreover, the integral relations

$$A_0(\xi_V m_V^2) = A_0(m_V^2) - \lambda_V m_V^2 \alpha_V, \tag{A.11a}$$

$$B_0(p^2, \xi_{V_1} m_{V_1}^2, m_{V_2}^2) = B_0(p^2, m_{V_1}^2, m_{V_2}^2) - \lambda_{V_1} m_{V_1}^2 \beta_{V_1V_2}(p^2), \tag{A.11b}$$

$$\lambda_V = 1 - \xi_V, \tag{A.11c}$$

as well as the integral simplifications

$$\begin{aligned} &\int_k \frac{k(k+2q)}{(k^2 - m_V^2)(k^2 - \xi_V m_V^2)((k+q)^2 - \xi_V m_V^2)} = \\ &\qquad \frac{i}{16\pi^2}\left((\xi_V m_V^2 - q^2)\beta_{V\xi_V V}(q^2) + \alpha_V\right), \end{aligned} \tag{A.12a}$$

$$\begin{aligned} &\int_k \frac{k(k+q)}{(k^2 - m_V^2)(k^2 - \xi_V m_V^2)((k+q)^2 - m_V^2)((k+q)^2 - \xi_V m_V^2)} = \\ &\qquad \frac{i}{16\pi^2}\frac{1}{\lambda_V m_V^2}\left(\left(m_V^2 - \frac{q^2}{2}\right)\beta_{VV}(q^2) - \left(\xi_V m_V^2 - \frac{q^2}{2}\right)\beta_{V\xi_V V}(q^2)\right), \end{aligned} \tag{A.12b}$$

have been used in the derivation of the pinch contributions. Furthermore, the relations

$$\frac{1}{(k^2 - m_V^2)(k^2 - \xi_V m_V^2)} = \frac{1}{\lambda_V m_V^2}\left(\frac{1}{k^2 - m_V^2} - \frac{1}{k^2 - \xi_V m_V^2}\right), \tag{A.13}$$

$$\sum_{i=1,2} \frac{O_{ii}}{q^2 - m_{h_i}^2} = \sum_{i,j=1,2} \frac{\left(q^2 - \frac{m_{h_i}^2 + m_{h_j}^2}{2}\right) O_{ij}^2}{(q^2 - m_{h_i}^2)(q^2 - m_{h_j^2})}, \tag{A.14}$$

can be applied in the calculation. With all the definitions and relations given, the actual calculation can be described.

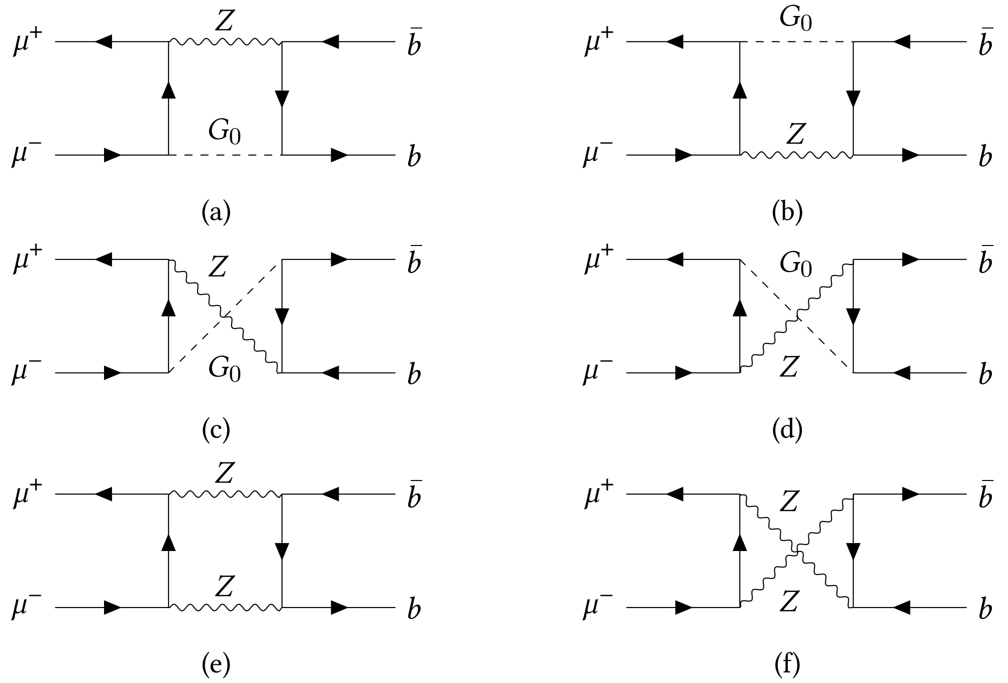

(a) (b)

(c) (d)

(e) (f)

Figure A.1.: All box diagrams with Z bosons that need to be considered in the pinch technique for the CxSM, where the G_0 is the Goldstone boson of Z.

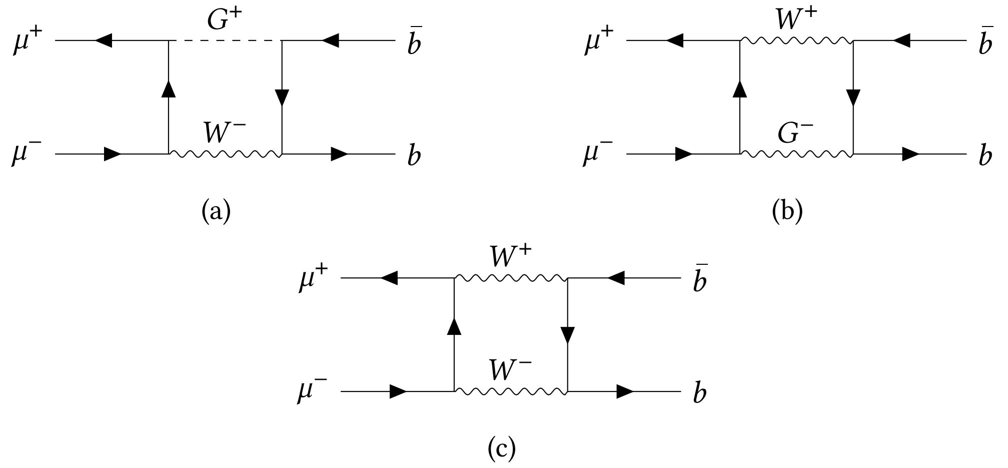

(a) (b)

(c)

Figure A.2.: All box diagrams with $W^\pm$ bosons that need to be considered in the pinch technique for the CxSM, where the $G^\pm$ are the Goldstone bosons of $W^\pm$.

A.1.1. Box Diagrams

First, all contributing box diagrams are considered, they can be seen in Figs. A.1 and A.2. No diagrams containing photons are listed, since the overall contribution of all photon box diagrams cancels. Moreover, no box diagrams containing Higgs particles are considered, since the pinch results of these diagrams do not contribute to the self-energies of the scalars h_i. They do not result in contributions to the scalar self-energies. Thus, only the

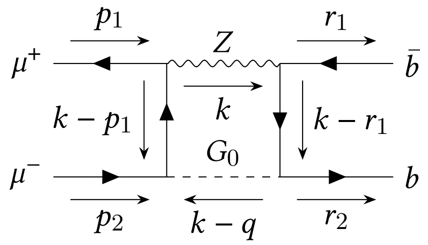

Figure A.3.: The kinematics in the box diagram used for the example calculation.

9 diagrams, given in Figs. A.1 and A.2, contribute to the pinch technique for the box diagrams. The pinching for the first diagram (see also Fig. A.3) is demonstrated in the following.

Before the presentation of the calculation the abbreviations

$$A_{\mathrm{L/R}} \equiv \left(-\frac{1}{2}P_{\mathrm{L/R}} + s_{\mathrm{W}}^2\right), \; A^b_{\mathrm{L/R}} \equiv \left(-\frac{1}{2}P_{\mathrm{L/R}} + \frac{1}{3}s_{\mathrm{W}}^2\right), \tag{A.15}$$

are introduced, which are part of the coupling between the Z boson and the muons or b quarks, respectively, the index on A indicating the quark coupling. Moreover, kinematics are used as seen in Fig. A.3 and the additional color factors of the quarks are ignored, since they are at the end counted to the Higgs-quark coupling and therefore do not contribute to the self-energy. Thus, the overall amplitude reads

$$\begin{aligned}
i\mathcal{A}^{ZG_0,1}_{\text{box}} =& \int_k \bar{v}(p_1)\frac{ig}{c_{\mathrm{W}}}\gamma^\mu A_{\mathrm{L}} iS(k-p_1)\frac{-m_\mu}{v}\gamma_5 u(p_2) && \text{(A.16a)}\\
& \bar{u}(r_2)\frac{-m_b}{v}\gamma_5 iS(k-r_1)\frac{ig}{c_{\mathrm{W}}}\gamma^\nu A^b_{\mathrm{L}} v(r_1) \\
& \frac{i}{(k-q)^2-\xi_Z m_Z^2}\frac{i}{k^2-m_Z^2}\left(-g_{\mu\nu}+\lambda_Z\frac{k_\mu k_\nu}{k^2-\xi_Z m_Z^2}\right) \\
\overset{\lambda_V}{\sim} & \int_k \frac{-\lambda_Z g^2 m_\mu m_b}{c_{\mathrm{W}}^2 v^2}\bar{v}(p_1)\not{k}A_{\mathrm{L}}S(k-p_1)\gamma_5 u(p_2)\bar{u}(r_2)\gamma_5 S(k-r_1)\not{k}A^b_{\mathrm{L}}v(r_1) \\
& \frac{1}{((k-q)^2-\xi_Z m_Z^2)(k^2-m_Z^2)(k^2-\xi_Z m_Z^2)} \\
\overset{\text{pinched}}{\sim} & \int_k \frac{-\lambda_Z g^2 m_\mu m_b}{c_{\mathrm{W}}^2 v^2}\bar{v}(p_1)A_{\mathrm{R}}\gamma_5 u(p_2)\bar{u}(r_2)\gamma_5 A^b_{\mathrm{L}}v(r_1) \\
& \frac{1}{((k-q)^2-\xi_Z m_Z^2)(k^2-m_Z^2)(k^2-\xi_Z m_Z^2)} \\
=& \frac{g^2 m_\mu m_b \lambda_Z}{c_{\mathrm{W}}^2 v^2}\frac{i}{16\pi^2}\beta_{Z\xi Z}(q^2)(\bar{v}(p_1)A_{\mathrm{R}}\gamma_5 u(p_2)\bar{u}(r_2)\gamma_5 A^b_{\mathrm{L}}v(r_1)), && \text{(A.16b)}
\end{aligned}$$

where in the pinching step Eqs. (A.3) and (A.5) where used and only parts with no remaining fermion propagator were kept. Furthermore, in the last step the transformation

$$i\Gamma^{\mu^-\mu^+h_i}\,\frac{i}{p^2-m_{h_i}^2}\,i\Sigma^{\text{add}}_{h_ih_j}\,\frac{i}{p^2-m_{h_j}^2}\,i\Gamma^{\bar{b}bh_j} =$$

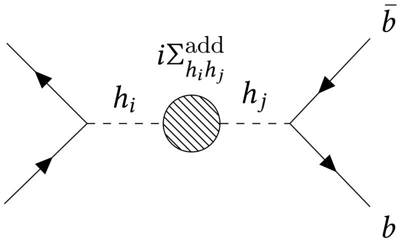

Figure A.4.: The pinched result rewritten in terms of self-energies compared to the diagrammatic expression.

$k \longrightarrow -k$ was made, which does not change anything except for the sign in the denominator. Combined with the other box diagrams with one Z boson and one G_0 Goldstone boson (see Fig. A.1 (b), (c) and (d)) the terms between the spinors simplify to unity up to an additional prefactor. The overall pinched amplitude results in

$$i\mathcal{A}^{ZG_0}_{\text{box,pinched}} = \frac{g^2 m_\mu m_b \lambda_Z}{c_{\text{W}}^2 v^2}\frac{i}{64\pi^2}\beta_{Z\xi Z}(q^2)\bar{v}(p_1)u(p_2)\bar{u}(r_2)v(r_1). \tag{A.17}$$

Using the identity $c_\alpha^2 + s_\alpha^2 = 1$ and $(-i)^2 = -1$ the result can be rewritten as

$$\begin{aligned}i\mathcal{A}^{ZG_0}_{\text{box,pinched}} =& \frac{-ig^2 m_\mu m_b \lambda_Z}{64\pi^2 c_{\text{W}}^2}\frac{1}{64\pi^2}\beta_{Z\xi Z}(q^2)\bar{v}(p_1)\frac{-im_\mu}{v}u(p_2)(c_\alpha^2+s_\alpha^2)^2\bar{u}(r_2)\frac{-im_b}{v}v(r_1)\\ =& \sum_{i,j=1,2}\left(i\Gamma^{\mu^-\mu^+h_i}\frac{i}{q^2-m_{h_i}^2}\left[(q^2-m_{h_i}^2)(q^2-m_{h_j}^2)\frac{ig^2\lambda_Z}{64\pi^2 c_{\text{W}}^2}\beta_{Z\xi Z}(q^2)O_{ij}\right]\right.\\ & \left.\frac{i}{q^2-m_{h_j}^2}i\Gamma^{\bar{b}bh_j}\right),\end{aligned} \tag{A.18}$$

with the respective $i\Gamma$ terms describing the couplings between the external fermions and the Higgs particles, written as

$$i\Gamma^{\mu^-\mu^+h_i} = \bar{v}(p_1)\frac{-im_\mu}{v}k_i u(p_2), \tag{A.19a}$$

$$i\Gamma^{\bar{b}bh_j} = \bar{u}(r_2)\frac{-im_b}{v}k_j v(r_1). \tag{A.19b}$$

Now the result is written as a self-energy contribution (compare with Fig. A.4) and the pinched contribution to the self-energies of h_i can be read of as

$$i\Sigma^{\text{add},ZG_0\,\text{box}}_{h_ih_j} = (q^2-m_{h_i}^2)(q^2-m_{h_j}^2)\frac{ig^2\lambda_Z}{64\pi^2 c_{\text{W}}^2}\beta_{Z\xi Z}(q^2)O_{ij}. \tag{A.20}$$

The other box diagrams are calculated analogously. The diagrams, however, with two gauge bosons are more involved. In these cases it might be useful to look at additional symmetries in the integrals, i.e. use the relation

$$\begin{aligned}
&\int_k \frac{k^\mu}{(k^2-m_V^2)(k^2-\xi_V m_V^2)((k+q)^2-m_V^2)((k+q)^2-m_V^2)} \\
\xrightarrow{k\to -k-q} &\int_k \frac{(-k-q)^\mu}{(k^2-m_V^2)(k^2-\xi_V m_V^2)((k+q)^2-m_V^2)((k+q)^2-m_V^2)} \\
\Rightarrow &\int_k \frac{k^\mu}{(k^2-m_V^2)(k^2-\xi_V m_V^2)((k+q)^2-m_V^2)((k+q)^2-m_V^2)} \\
= &-\frac{1}{2}\int_k \frac{q^\mu}{(k^2-m_V^2)(k^2-\xi_V m_V^2)((k+q)^2-m_V^2)((k+q)^2-m_V^2)},
\end{aligned} \tag{A.21}$$

after combining the results of both diagrams for the respective gauge boson.

At the end, the sum of all contributions from the box diagrams results in

$$\begin{aligned}
i\Sigma_{h_ih_j}^{\text{add,box}} = &(q^2-m_{h_i}^2)(q^2-m_{h_j}^2)\frac{ig^2\lambda_Z O_{ij}}{64c_\text{w}^2\pi^2}\frac{\beta_{ZZ}(q^2)+\beta_{Z\xi_Z Z}(q^2)}{2} \\
&+(q^2-m_{h_i}^2)(q^2-m_{h_j}^2)\frac{ig^2\lambda_W O_{ij}}{32\pi^2}\frac{\beta_{WW}(q^2)+\beta_{W\xi_W W}(q^2)}{2}.
\end{aligned} \tag{A.22}$$

A.1.2. External Leg Corrections

The derivation of the pinch contributions for the external leg corrections is similar to the derivation for the box diagrams. All contributing diagrams can be seen in Fig. A.5. A total of 12 diagrams has to be considered. However, a subtle problem arises, namely that in all leg corrections a fermion propagator $S(p)$ with external momentum p appears. Setting the momentum on-shell results in a divergence in the propagator. Since the pinch technique is to be applied before the actual regularization and renormalization, this creates a problem. But as it turns out, by carefully pinching out the fermion propagators, the pinched result contains no divergences at the end. To derive this contribution a careful handling of the divergent terms has to be applied. In principle, an additional shift in the momenta could be introduced to set the external particles slightly off-shell, apply the pinch technique and then set this shift to zero [101]. This avoids the problem of the divergent terms and a proper solution can be found. However, a more practical approach is to re-write all slashed loop momenta with Eq. (A.3), but not use the identities in Eq. (A.5). Then, all appearing fermion propagators and inverse propagators between two fermion spinors have to be simplified. Then, all divergent parts are canceled in the relevant pinched parts, the identities (A.5) can be again applied to obtain a final result. This is in the end the same procedure as shifting the momenta, since in both methods the straightforward usage of Eq. (A.5) is at first prohibited so that the divergent terms can be treated.

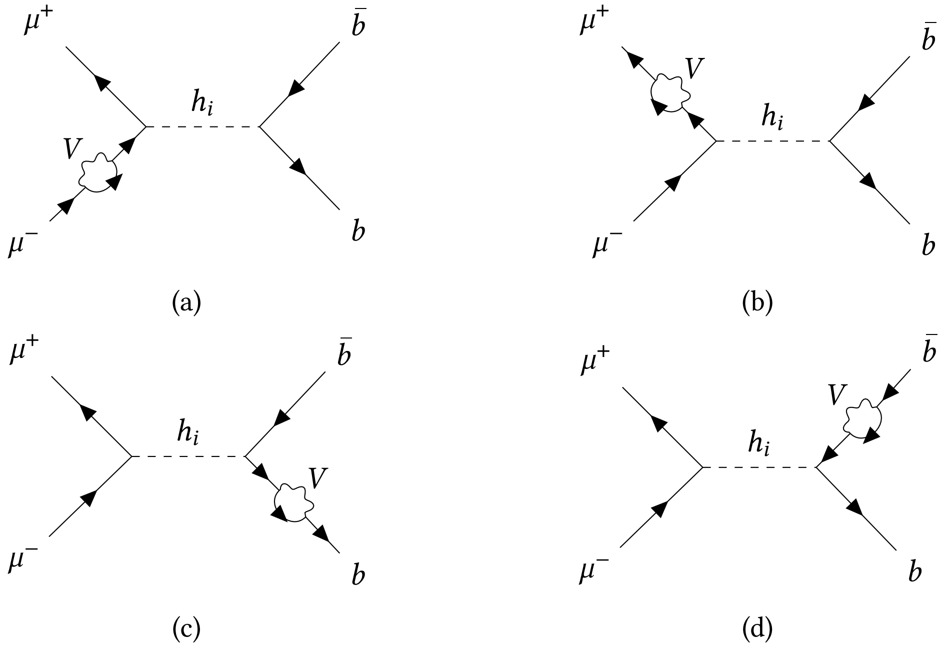

(a) (b)

(c) (d)

Figure A.5.: All external leg corrections that need to be considered in the pinch technique for the CxSM, where $V \in \{W, Z, \gamma\}$.

If the calculation of the pinched parts is then executed properly, the overall result reads

$$
\begin{aligned}
i\Sigma^{\text{add,leg}}_{h_i h_j} = & \frac{-i5\lambda_\gamma e^2}{72\pi^2} O_{ij} \left(q^2 - \frac{m^2_{h_i} + m^2_{h_j}}{2} \right) \alpha_\gamma \\
& + \frac{-i\lambda_W g^2}{32\pi^2} O_{ij} \left(q^2 - \frac{m^2_{h_i} + m^2_{h_j}}{2} \right) \alpha_W \\
& + \frac{-i\lambda_Z g^2}{64\pi^2 c^2_{\text{W}}} O_{ij} \left(q^2 - \frac{m^2_{h_i} + m^2_{h_j}}{2} \right) \alpha_Z \left(1 - \frac{8}{3} s^2_{\text{W}} + \frac{40}{9} s^4_{\text{W}} \right) .
\end{aligned}
\tag{A.23}
$$

Here an additional factor $\frac{1}{2}$ to the leg correction from the LSZ reduction has to be considered.

A.1.3. Triangle Diagrams

The last contributions that have to be considered are the triangle diagrams. They are quite straightforward to calculate, similar to the box diagrams. All diagrams can be seen in the Figs. A.6, A.7 and A.8, in total 16 diagrams. However, now the couplings between Higgs particles and gauge bosons, as well as Higgs particles, gauge bosons and goldstone bosons have to be considered. They can introduce additional momentum contributions, which also have to be pinched out. Therefore gauge-independent contributions to the

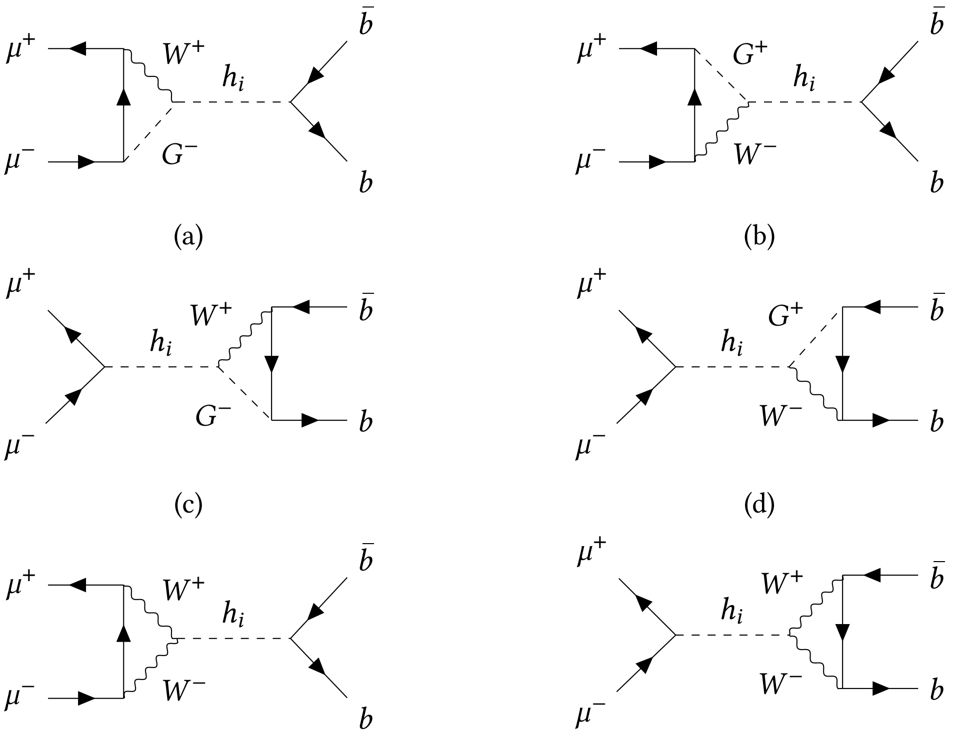

(a) (b)

(c) (d)

(e) (f)

Figure A.6.: All triangle diagrams with $W^\pm$ bosons, which need to be considered in the pinch technique for the CxSM.

self-energies arise. Moreover, the integral reductions in Eq. (A.12) might be helpful to simplify the results. At the end, the overall result of the triangle pinch contributions reads

$$\begin{aligned}
i\Sigma^{\text{add,tri}}_{h_ih_j} = {} & \frac{i5\lambda_\gamma e^2}{72\pi^2} O_{ij}\left(q^2 - \frac{m^2_{h_i}+m^2_{h_j}}{2}\right)\alpha_\gamma \\
& + \frac{-ig^2}{16\pi^2} O_{ij}\left(q^2 - \frac{m^2_{h_i}+m^2_{h_j}}{2}\right)\Bigg(B_0(q^2, m_W^2, m_W^2) \\
& +\lambda_W\left[q^2\frac{\beta_{WW}(q^2)+\beta_{W\xi_W W}(q^2)}{2} - \alpha_W\right]\Bigg) \\
& + \frac{-ig^2}{32\pi^2 c_{\text{w}}^2} O_{ij}\left(q^2 - \frac{m^2_{h_i}+m^2_{h_j}}{2}\right)\Bigg(B_0(q^2, m_Z^2, m_Z^2) \\
& + \lambda_Z\left[q^2\frac{\beta_{ZZ}(q^2)+\beta_{Z\xi_Z Z}(q^2)}{2} + \alpha_Z(-1+\frac{4}{3}s_{\text{w}}^2 - \frac{20}{9}s_{\text{w}}^4)\right]\Bigg)\,.
\end{aligned} \tag{A.24}$$

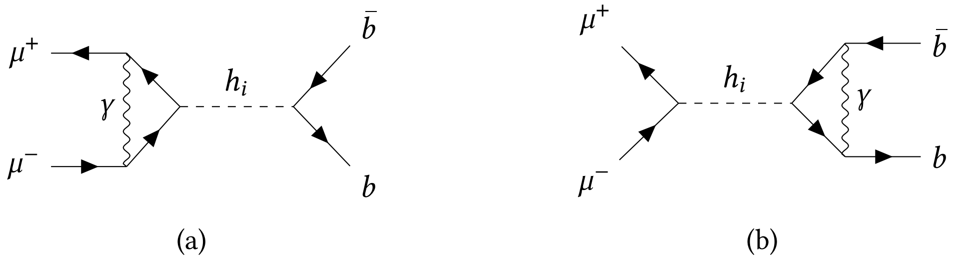

Figure A.7.: All triangle diagrams with photons, which need to be considered in the pinch technique for the CxSM.

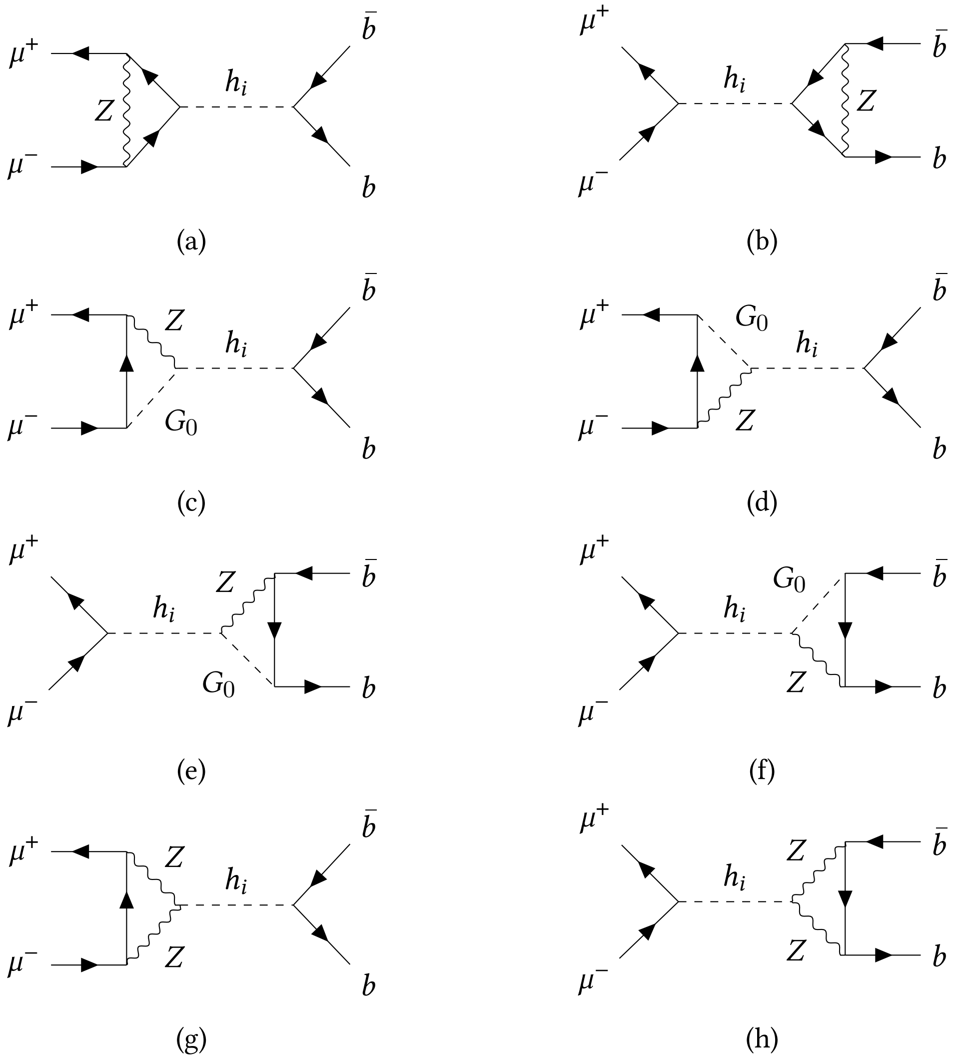

Figure A.8.: All triangle diagrams with Z bosons, which need to be considered in the pinch technique for the CxSM.

A.1.4. Final Result

After finishing all calculations, the final result can be put together by summing up all contributions. Thus, the overall pinch contributions to the self-energies of the h_i particles read

$$
\begin{aligned}
i\Sigma^{\text{add}}_{h_i h_j} &= i\Sigma^{\text{add, box}}_{h_i h_j} + i\Sigma^{\text{add, leg}}_{h_i h_j} + i\Sigma^{\text{add, tri}}_{h_i h_j} \\
&= \frac{-ig^2}{16\pi^2} O_{ij} \left(q^2 - \frac{m_{h_i}^2 + m_{h_j}^2}{2} \right) B_0(q^2, m_W^2, m_W^2) \\
&+ \frac{-ig^2}{32\pi^2 c_{\text{w}}^2} O_{ij} \left(q^2 - \frac{m_{h_i}^2 + m_{h_j}^2}{2} \right) B_0(q^2, m_Z^2, m_Z^2). \\
&+ \frac{ig^2 \lambda_W}{32\pi^2} O_{ij} \left(\left(q^2 - \frac{m_{h_i}^2 + m_{h_j}^2}{2} \right) \alpha_W - (q^4 - m_{h_i}^2 m_{h_j}^2) \frac{\beta_{WW}(q^2) + \beta_{W\xi_W W}(q^2)}{2} \right) \\
&+ \frac{ig^2 \lambda_Z}{64\pi^2 c_{\text{w}}^2} O_{ij} \left(\left(q^2 - \frac{m_{h_i}^2 + m_{h_j}^2}{2} \right) \alpha_Z - (q^4 - m_{h_i}^2 m_{h_j}^2) \frac{\beta_{ZZ}(q^2) + \beta_{Z\xi_Z Z}(q^2)}{2} \right).
\end{aligned}
\tag{A.25}
$$

This result can be compared with other works, e.g. [73, 74], but the different structure of the models has to be taken into account. Nevertheless, with this in mind the results are similar.

The gauge-dependent part of the self-energies of h_i has also been calculated and exactly cancels with the gauge-dependent parts of the additional contributions from the pinched technique. This however, only happens with the inclusion of tadpoles to the self-energies. Thus, the pinched self-energies as defined in Eq. (3.59) are indeed gauge-independent.

A.2. More on the ZEM Scheme

In this part of the appendix the ZEM scheme is discussed in detail, to see how the gauge dependence of the corresponding counterterm of v_S arises.

To start with, the generic NLO amplitude of the decay process $h_i \to AA$ is derived. The diagrams that contribute to the process at NLO are shown in Fig. 4.4. The leg corrections can be written as,

$$\begin{aligned} i\mathcal{A}^{\text{Leg,IN}}_{h_i\to AA} &= i\Sigma_{h_ih_i}(p^2_{\text{IN}})\frac{i}{p^2_{\text{IN}} - m^2_{h_i}}(-i\lambda_{h_iAA}) + i\Sigma_{h_ih_j}(p^2_{\text{IN}})\frac{i}{p^2_{\text{IN}} - m^2_{h_j}}(-i\lambda_{h_jAA}) \\ &= \frac{\lambda_{h_iAA}\Sigma_{h_ih_i}(p^2_{\text{IN}})}{p^2_{\text{IN}} - m^2_{h_i}} + \frac{\lambda_{h_jAA}\Sigma_{h_ih_j}(p^2_{\text{IN}})}{p^2_{\text{IN}} - m^2_{h_j}}, \end{aligned} \tag{A.26}$$

$$\begin{aligned} i\mathcal{A}^{\text{Leg,OUT}}_{h_i\to AA} &= i\Sigma_A(p^2_{\text{OUT1}})\frac{i}{p^2_{\text{OUT1}} - m^2_A}(-i\lambda_{h_iAA}) + i\Sigma_A(p^2_{\text{OUT2}})\frac{i}{p^2_{\text{OUT2}} - m^2_A}(-i\lambda_{h_iAA}) \\ &= i\lambda_{h_iAA}\left(\frac{\Sigma_A(p^2_{\text{OUT1}})}{p^2_{\text{OUT1}} - m^2_A} + \frac{\Sigma_A(p^2_{\text{OUT2}})}{p^2_{\text{OUT2}} - m^2_A}\right). \end{aligned} \tag{A.27}$$

The leg counterterms as well as the vertex counterterm are given as

$$\begin{aligned} i\mathcal{A}^{\text{LegCT,IN}}_{h_i\to AA} &= i\left((p^2_{\text{IN}} - m^2_{h_i})\delta Z_{h_ih_i} - \delta m^2_{h_i}\right)\frac{i}{p^2_{\text{IN}} - m^2_{h_i}}(-i\lambda_{h_iAA}) \\ &+ \frac{i}{2}\left(p^2_{\text{IN}}(\delta Z_{h_ih_j} + \delta Z_{h_jh_i}) - (m^2_{h_i}\delta Z_{h_ih_j} + m^2_{h_j}\delta Z_{h_jh_i})\right)\frac{i}{p^2_{\text{IN}} - m^2_{h_i}}(-i\lambda_{h_jAA}) \\ &= \frac{i\lambda_{h_iAA}}{p^2_{\text{IN}} - m^2_{h_i}}\left((p^2_{\text{IN}} - m^2_{h_i})\delta Z_{h_ih_i} - \delta m^2_{h_i}\right) \\ &+ \frac{i\lambda_{h_jAA}}{2(p^2_{\text{IN}} - m^2_{h_j})}\left(p^2_{\text{IN}}(\delta Z_{h_ih_j} + \delta Z_{h_jh_i}) - (m^2_{h_i}\delta Z_{h_ih_j} + m^2_{h_j}\delta Z_{h_jh_i})\right), \end{aligned} \tag{A.28}$$

$$\begin{aligned} i\mathcal{A}^{\text{LegCT,OUT}}_{h_i\to AA} &= i\left((p^2_{\text{OUT1}} - m^2_A)\delta Z_A - \delta m^2_A\right)\frac{i}{p^2_{\text{OUT1}} - m^2_A}(-i\lambda_{h_iAA}) \\ &+ i\left((p^2_{\text{OUT2}} - m^2_A)\delta Z_A - \delta m^2_A\right)\frac{i}{p^2_{\text{OUT2}} - m^2_A}(-i\lambda_{h_iAA}) \\ &= \frac{i\lambda_{h_iAA}}{p^2_{\text{OUT1}} - m^2_A}\left((p^2_{\text{OUT1}} - m^2_A)\delta Z_A - \delta m^2_A\right) \\ &+ \frac{i\lambda_{h_iAA}}{p^2_{\text{OUT2}} - m^2_A}\left((p^2_{\text{OUT2}} - m^2_A)\delta Z_A - \delta m^2_A\right). \end{aligned} \tag{A.29}$$

$$i\mathcal{A}^{\text{CT}}_{h_i\to AA} = -i\lambda_{h_iAA}\left(\frac{\delta\lambda_{h_iAA}}{\lambda_{h_iAA}} + \delta Z_A + \frac{\delta Z_{h_ih_i}}{2} + \frac{\lambda_{h_jAA}}{\lambda_{h_iAA}}\frac{\delta Z_{h_jh_i}}{2}\right), \tag{A.30}$$

The vertex counterterm $\mathcal{A}^{\text{CT}}_{h_i\to AA}$ has been derived in Sec. 4.5, whereas the expression for the leg counterterms can be taken from literature, e.g. [42].

The total sum of all contributions results in,

$$\begin{aligned}
i\mathcal{A}^{\text{Total}} &= \frac{i\lambda_{h_iAA}\Sigma_{h_ih_i}(p_{\text{IN}}^2)}{p_{\text{IN}}^2 - m_{h_i}^2} + \frac{i\lambda_{h_jAA}\Sigma_{h_ih_j}(p_{\text{IN}}^2)}{p_{\text{IN}}^2 - m_{h_j}^2} + i\mathcal{A}^{\text{VC}}_{h_i\to AA}(\{p\}) \\
&+ i\lambda_{h_iAA}\left(\frac{\Sigma_A(p_{\text{OUT1}}^2)}{p_{\text{OUT1}}^2 - m_A^2} + \frac{\Sigma_A(p_{\text{OUT2}}^2)}{p_{\text{OUT2}}^2 - m_A^2}\right) \\
&+ \frac{i\lambda_{h_iAA}}{p_{\text{IN}}^2 - m_{h_i}^2}\left((p_{\text{IN}}^2 - m_{h_i}^2)\delta Z_{h_ih_i} - \delta m_{h_i}^2\right) \\
&+ \frac{i\lambda_{h_jAA}}{2(p_{\text{IN}}^2 - m_{h_j}^2)}\left(p_{\text{IN}}^2(\delta Z_{h_ih_j} + \delta Z_{h_jh_i}) - (m_{h_i}^2\delta Z_{h_ih_j} + m_{h_j}^2\delta Z_{h_jh_i})\right) \\
&+ -i\lambda_{h_iAA}\left(\frac{\delta\lambda_{h_iAA}}{\lambda_{h_iAA}} + \delta Z_A + \frac{\delta Z_{h_ih_i}}{2} + \frac{\lambda_{h_jAA}}{\lambda_{h_iAA}}\frac{\delta Z_{h_jh_i}}{2}\right) \\
&+ \frac{i\lambda_{h_iAA}}{p_{\text{OUT1}}^2 - m_A^2}\left((p_{\text{OUT1}}^2 - m_A^2)\delta Z_A - \delta m_A^2\right) \\
&+ \frac{i\lambda_{h_iAA}}{p_{\text{OUT2}}^2 - m_A^2}\left((p_{\text{OUT2}}^2 - m_A^2)\delta Z_A - \delta m_A^2\right),
\end{aligned} \tag{A.31}$$

$$\begin{aligned}
&= \frac{i\lambda_{h_iAA}}{p_{\text{IN}}^2 - m_{h_i}^2}\left(\Sigma_{h_ih_i}(p_{\text{IN}}^2) - \delta m_{h_i}^2\right) \\
&+ \frac{i\lambda_{h_jAA}}{p_{\text{IN}}^2 - m_{h_j}^2}\left(\Sigma_{h_ih_j}(p_{\text{IN}}^2) + (p_{\text{IN}}^2 - m_{h_i}^2)\frac{\delta Z_{h_ih_j}}{2}\right) \\
&+ \frac{i\lambda_{h_iAA}}{p_{\text{OUT1}}^2 - m_A^2}\left(\Sigma_A(p_{\text{OUT1}}^2) - \delta m_A^2\right) \\
&+ \frac{i\lambda_{h_iAA}}{p_{\text{OUT2}}^2 - m_A^2}\left(\Sigma_A(p_{\text{OUT2}}^2) - \delta m_A^2\right) \\
&+ i\lambda_{h_iAA}\left(-\frac{\delta\lambda_{h_iAA}}{\lambda_{h_iAA}} + \delta Z_A + \frac{\delta Z_{h_ih_i}}{2}\right) \\
&+ i\mathcal{A}^{\text{VC}}_{h_i\to AA}(\{p\}),
\end{aligned} \tag{A.32}$$

where the external momenta are abbreviated with $\{p\}$. This is the most general result without choosing a specific renormalization scheme or specifying the external momenta. The limits for the momenta are discussed next. Moreover, since in the following the alternative tadpole scheme is always used, the tadpole contributions are implicitly added to the vertex corrections.

A.2.1. OS Limit

As a brief cross check, the OS conditions for the external momenta are used. Thus, the external squared momenta are set to the corresponding masses and the relations,

$$\Sigma(p^2) \approx \overbrace{\Sigma(m^2)}^{=\delta m^2} + (p^2 - m^2) \overbrace{\left.\frac{\partial \Sigma(p^2)}{\partial p^2}\right|_{p^2=m^2}}^{=-\delta Z} \tag{A.33a}$$

$$\Rightarrow \frac{1}{p^2 - m^2}\left(\Sigma(p^2) - \delta m^2\right) \xrightarrow{p^2 \to m^2} -\delta Z, \tag{A.33b}$$

can be used (compare with the definition of the counterterms, e.g. Eqs. (3.32) and (3.19)). Therefore the overall amplitude can be simplified to

$$\begin{aligned}
i\mathcal{A}^{\text{Total,OS}}_{h_i \to AA} =& - i\lambda_{h_iAA}\delta Z_{h_ih_i} + i\lambda_{h_jAA} \overbrace{\frac{1}{m^2_{h_i} - m^2_{h_j}}\Sigma_{h_ih_j}(m^2_{h_i}))}^{=-\frac{\delta Z_{h_jh_i}}{2}} \\
& - 2i\lambda_{h_iAA}\delta Z_A + i\lambda_{h_iAA}\left(\frac{\delta\lambda_{h_iAA}}{\lambda_{h_iAA}} + \delta Z_A + \frac{\delta Z_{h_ih_i}}{2}\right) + i\mathcal{A}^{\text{VC}}_{h_i \to AA}(\{p^2 = m^2\}) \\
=& i\mathcal{A}^{\text{VC}}_{h_i \to AA}(\{p^2 = m^2\}) \\
& \underbrace{- i\lambda_{h_iAA}\left(\frac{\delta\lambda_{h_iAA}}{\lambda_{h_iAA}} + \delta Z_A + \frac{\delta Z_{h_ih_i}}{2} + \frac{\lambda_{h_jAA}}{\lambda_{h_iAA}}\frac{\delta Z_{h_jh_i}}{2}\right)}_{=i\mathcal{A}^{\text{CT}}_{h_i \to AA}}.
\end{aligned} \tag{A.34}$$

This means that only the vertex corrections and the vertex counterterm contribute, which is to be expected since the leg corrections should be canceled by the leg counterterms. Thus, since the overall amplitude is gauge-independent (see Sec. 4.5), $\mathcal{A}^{\text{VC}}_{h_i \to AA}(\{p^2 = m^2\})$ and $\mathcal{A}^{\text{CT}}_{h_i \to AA}$ are gauge-independent in combination.

With the expressions for the counterterms of the couplings constants λ_{h_iAA}, determined in Eq. (3.66), the overall amplitude is given by

$$\begin{aligned}
i\mathcal{A}^{\text{Total,OS}}_{h_i \to AA} =& i\mathcal{A}^{\text{VC}}_{h_i \to AA}(\{p^2 = m^2\}) \\
& - i\lambda_{h_iAA}\left(\frac{\delta m^2_{h_i}}{m^2_{h_i}} - \frac{\delta v_S}{v_S} + T_i(\alpha)\delta\alpha + \delta Z_A + \frac{\delta Z_{h_ih_i}}{2} + \frac{\lambda_{h_jAA}}{\lambda_{h_iAA}}\frac{\delta Z_{h_jh_i}}{2}\right),
\end{aligned} \tag{A.35}$$

where $T_i(\alpha)$ is defined in Eq. (3.66). Next, the gauge dependence of the different contributions is discussed. The self-energy for A is by itself already gauge-independent. Therefore, all derived quantities are gauge-independent as well, e.g. δZ_A and δm^2_A. Moreover, the mass counterterms $\delta m^2_{h_i}$ are also gauge-independent but the field strength renormalization constants $\delta Z_{h_ih_j}$ are, in general, gauge-dependent.

If now the pinched self-energies are used for the renormalization of α, the resulting counterterm $\delta\alpha$ is gauge-independent as well. If the process-dependent scheme is chosen for the renormalization of v_S, the corresponding counterterm δv_S is also gauge-independent. Since the overall amplitude was already checked to be gauge-independent, this means that the combination

$$\mathcal{A}^{\text{VC}}_{h_i\to AA}(\{p^2=m^2\}) - i\lambda_{h_iAA}\left(+\frac{\delta Z_{h_ih_i}}{2}+\frac{\lambda_{h_jAA}}{\lambda_{h_iAA}}\frac{\delta Z_{h_jh_i}}{2}\right), \tag{A.36}$$

is gauge-independent.

A.2.2. ZEM Limit

In the last subsection it was shown that a gauge-independent counterterm of v_S leads to a gauge-independent overall result with the external momenta set to the corresponding masses. Thus, a new renormalization scheme for v_S has to result in a gauge-independent counterterm as well in order for the overall result to be gauge-independent. Therefore, a gauge-independent counterterm of v_S has to be derived in the ZEM scheme.

To derive the counterterm of v_S in the ZEM scheme, a different limit is taken, namely $p^2 \to 0$. Therefore, the overall amplitude used in the derivation of v_S can be written as

$$\begin{aligned}
i\mathcal{A}^{\text{Total,ZEM}}_{h_i\to AA} &= i\mathcal{A}^{\text{VC}}_{h_i\to AA}(\{p^2=0\}) \qquad\qquad (\text{A.37})\\
&\quad \overbrace{+\frac{-i\lambda_{h_iAA}}{m^2_{h_i}}\Sigma_{h_ih_i}(0)+\frac{-i\lambda_{h_jAA}}{m^2_{h_j}}\Sigma_{h_ih_j}(0)+\frac{-2i\lambda_{h_iAA}}{m^2_A}\Sigma_A(0)}^{\equiv i\mathcal{A}^{\text{Leg}}_{h_i\to AA}(\{p^2=0\})}\\
&\quad + i\lambda_{h_iAA}\left(-\frac{\delta\lambda_{h_iAA}}{\lambda_{h_iAA}}+\delta Z_A+\frac{\delta Z_{h_ih_i}}{2}+\frac{\delta m^2_{h_i}}{m^2_{h_i}}+\frac{2\delta m^2_A}{m^2_A}+\frac{\lambda_{h_jAA}}{\lambda_{h_iAA}}\frac{m^2_{h_i}}{m^2_{h_j}}\frac{\delta Z_{h_ih_j}}{2}\right)\\
&= i\mathcal{A}^{\text{VC}}_{h_i\to AA}(\{p^2=0\})+i\mathcal{A}^{\text{Leg}}_{h_i\to AA}(\{p^2=0\})\\
&\quad + i\lambda_{h_iAA}\left(\frac{\delta v_S}{v_S}-T_i(\alpha)\delta\alpha+\delta Z_A+\frac{2\delta m^2_A}{m^2_A}+\frac{\delta Z_{h_ih_i}}{2}+\frac{\lambda_{h_jAA}}{\lambda_{h_iAA}}\frac{m^2_{h_i}}{m^2_{h_j}}\frac{\delta Z_{h_ih_j}}{2}\right).
\end{aligned}$$

The leg correction now do not get canceled by the corresponding counterterms as it was the case in the OS scheme, because here the external momenta are set to zero, whereas the counterterms are defined with the momenta set to the OS masses.

The combination of $\mathcal{A}^{\text{VC}}_{h_i\to AA}(\{p^2=0\})$ and $\mathcal{A}^{\text{Leg}}_{h_i\to AA}(\{p^2=0\})$ has been found to be gauge-independent. Thus, the gauge dependence of the counterterms in combination has to cancel as well. More precisely the terms

$$\frac{\delta Z_{h_ih_i}}{2}+\frac{\lambda_{h_jAA}}{\lambda_{h_iAA}}\frac{m^2_{h_i}}{m^2_{h_j}}\frac{\delta Z_{h_ih_j}}{2}, \tag{A.38}$$

have to be in total gauge-independent to obtain a gauge-independent counterterm of v_S, since all other counterterms are already gauge-independent by themselves (if the pinched scheme is used for $\delta\alpha$). However, it was found that this combination is gauge-dependent. Therefore, the resulting counterterm for v_S in the ZEM scheme will be gauge-dependent defined in this way.

Another approach would be to use the KOSY-Scheme for $\delta\alpha$,

$$\delta\alpha = \frac{\delta Z_{h_1h_2} - \delta Z_{h_2h_1}}{4} \; (+\delta G \text{ if } Z_G \text{ is not symmetric}) \, , \tag{A.39}$$

which leads to a gauge-dependent α counterterm. This additional gauge-dependence could cancel the gauge dependence in the ZEM scheme. Thus, the terms

$$-T_i(\alpha)\frac{\delta Z_{h_1h_2} - \delta Z_{h_2h_1}}{4} + \frac{\delta Z_{h_ih_i}}{2} + \frac{\lambda_{h_jAA}}{\lambda_{h_iAA}}\frac{m_{h_i}^2}{m_{h_j}^2}\frac{\delta Z_{h_ih_j}}{2}, \tag{A.40}$$

have to be gauge-independent, but this was also not found to be the case. Therefore this method does not lead to a gauge-independent counterterm of v_S either. Furthermore it would be inconsistent to use different schemes for $\delta\alpha$ in different places.

It can also be checked whether the usage of the KOSY scheme everywhere in the renormalized amplitude would lead to a gauge-independent amplitude. Thus, as a test, δv_S is defined with the ZEM scheme via the process $h_2 \to AA$. This means that Eq. (A.37) is set to zero and solved for δv_S. The obtained result is

$$\begin{aligned} &\mathcal{A}^{\text{Total,ZEM}}_{h_2\to AA} \overset{!}{=} 0 \\ \Rightarrow \quad &\frac{\delta v_S^{\text{ZEM}}}{v_S} = -\frac{\mathcal{A}^{\text{VC}}_{h_2\to AA}(\{p^2=0\}) + \mathcal{A}^{\text{Leg}}_{h_2\to AA}(\{p^2=0\})}{\lambda_{h_2AA}} - \tan(\alpha)\delta\alpha \\ &\qquad - \delta Z_A - \frac{2\delta m_A^2}{m_A^2} - \frac{\delta Z_{h_2h_2}}{2} - \tan(\alpha)\frac{\delta Z_{h_2h_1}}{2}. \end{aligned} \tag{A.41}$$

This expression for δv_S can now be used to renormalize the process $h_1 \to AA$ amplitude and to check if a gauge-independent result can be obtained. Thus, the result from Eq. (A.34) is used since the overall amplitude at the end should resemble a physical process, i.e. with external momenta set to the masses of the external particles. Inserting the expression for δv_S^{ZEM} results in

$$\begin{aligned} i\mathcal{A}^{\text{Tot}}_{h_1\to AA} = i\mathcal{A}^{\text{VC}}_{h_1\to AA} - i\lambda_{h_1AA}\Bigg(&\frac{\delta m_{h_1}^2}{m_{h_1}^2} - \frac{\delta v_S^{\text{ZEM}}}{v_S} \\ &+ \cot(\alpha)\delta\alpha + \delta Z_A + \frac{\delta Z_{h_1h_1}}{2} + \cot(\alpha)\frac{m_{h_2}^2}{m_{h_1}^2}\frac{\delta Z_{h_2h_1}}{2}\Bigg) \, . \end{aligned} \tag{A.42}$$

Inserting the derived relations results in

$$\begin{aligned}\Rightarrow\ i\mathcal{A}^{\mathrm{Tot}}_{h_1\to AA} &= i\mathcal{A}^{\mathrm{VC}}_{h_1\to AA} - i\frac{\lambda_{h_1AA}}{\lambda_{h_2AA}}\overbrace{\left(\mathcal{A}^{\mathrm{VC}}_{h_2\to AA}(\{p^2=0\}) + \mathcal{A}^{\mathrm{Leg}}_{h_2\to AA}(\{p^2=0\})\right)}^{\text{gauge-independent}} \\ &- i\lambda_{h_1AA}\left(\frac{\delta m^2_{h_1}}{m^2_{h_1}} + \delta\alpha(\cot(\alpha)+\tan(\alpha)) + 2\delta Z_A + \frac{2\delta m^2_A}{m^2_A}\right. \\ &\left. + \frac{1}{2}\left(\delta Z_{h_1h_1} + \delta Z_{h_2h_2}\right) + \frac{\delta Z_{h_2h_1}}{2}\left(\tan(\alpha) + \cot(\alpha)\frac{m^2_{h_2}}{m^2_{h_1}}\right)\right).\end{aligned} \tag{A.43}$$

Since in the normal process-dependent scheme δv_S is gauge-independent, the combination

$$\mathcal{A}^{\mathrm{VC}}_{h_i\to AA} - \lambda_{h_1AA}\left(\frac{\delta Z_{h_1h_1}}{2} + \cot(\alpha)\frac{m^2_{h_2}}{m^2_{h_1}}\delta Z_{h_2h_1}\right), \tag{A.44}$$

has to be gauge-independent (cf. to Eq. (A.36)). The other occurring mass counterterms $\delta m^2_{h_1}$ and δm^2_A, as well as δZ_A are already gauge-independent. Thus, the remaining terms with a possible overall gauge dependence are

$$\delta\alpha(\cot(\alpha)+\tan(\alpha)) + \frac{1}{2}\delta Z_{h_2h_2} + \frac{\delta Z_{h_2h_1}}{2}\tan(\alpha). \tag{A.45}$$

If the pinched scheme is used to obtain a gauge-independent $\delta\alpha$, the remaining term is not gauge-independent as already seen above. If the KOSY scheme is used for $\delta\alpha$, the gauge dependence of this combination was checked, but it was also found to not be gauge-independent.

To conclude, the ZEM scheme results in a gauge-dependent counterterm for v_S unless in the definition of δv_S the pinched self-energies used for the definition of the $\delta Z_{h_ih_j}$ are applied as described in Sec. 3.5.2.

In principle the definition of the counterterms of δm^2 and δZ could be altered for the fields h_i and A such that in the ZEM scheme the leg contributions would again be canceled by the counterterms, i.e. that the counterterms would be defined with respect to the limit $p^2 \to 0$ instead of $p^2 \to m^2$. However, the UV divergences of the self-energies and thus of the derived counterterms such as δm^2 and δZ depend on the external momentum. Altering the definition with respect to the limit of setting the squared momenta to zero, the overall UV divergence of the counterterm of v_S is changed and the overall cancellation of UV divergences in the fully renormalized amplitude can no longer be guaranteed. Therefore this idea also does not lead to a suitable solution of a gauge-independent ZEM counterterm for v_S.

Acknowledgement

My special thanks go to Prof. Dr. M. Margarete Mühlleitner for providing me with the opportunity to work at her institute and for offering me this interesting topic. I really enjoyed our weekly meetings and discussions. Furthermore, the advice and help she gave me were truly helpful in understanding the topics of the thesis.

Next, I want to thank Prof. Dr. Rui Santos for agreeing to be my second referee of my master's thesis. Moreover, I really enjoyed the weekly meetings with him, João and Prof. Mühlleitner, not only because we had fruitful discussions and made good progress, but also on a personal level. I especially want to thank João for our detailed cross checks of results.

Moreover, I want to express my gratitude to Dr. Jonas Müller and Martin Gabelmann. They taught me everything I needed to know about the used computational tools and were always available for arising questions regarding all the technical details of a master thesis.

Furthermore, I want to thank Dr. Sophie Williamson and Lisa Biermann for proof reading my thesis and their suggestions. Furthermore, they were always available for a short talk about both physical and non-physical topics. I especially enjoyed our lunch breaks. Lisa, in particular, made my life in the institute so much better and easier. She helped me through every little problem or question that arose and I didn't know where to go to with.

Finally, I want to thank my family for supporting me throughout all these years.

Bibliography

[1] Paul Adrien Maurice Dirac and Ralph Howard Fowler. “The quantum theory of the electron”. In: *Proceedings of the Royal Society of London. Series A, Containing Papers of a Mathematical and Physical Character* 117.778 (1928), pp. 610–624. DOI: 10.1098/rspa.1928.0023. eprint: https://royalsocietypublishing.org/doi/pdf/10.1098/rspa.1928.0023.

[2] Paul Adrien Maurice Dirac. “Quantised singularities in the electromagnetic field,” in: *Proceedings of the Royal Society of London. Series A, Containing Papers of a Mathematical and Physical Character* 133.821 (1931), pp. 60–72. DOI: 10.1098/rspa.1931.0130. eprint: https://royalsocietypublishing.org/doi/pdf/10.1098/rspa.1931.0130.

[3] Carl D. Anderson. “The Positive Electron”. In: *Phys. Rev.* 43 (6 Mar. 1933), pp. 491–494. DOI: 10.1103/PhysRev.43.491.

[4] C. G. Bollini and J. J. Giambiagi. “Dimensional Renormalization: The Number of Dimensions as a Regularizing Parameter”. In: *Nuovo Cim.* B12 (1972), pp. 20–26. DOI: 10.1007/BF02895558.

[5] Gerard ’t Hooft and M. J. G. Veltman. “Regularization and Renormalization of Gauge Fields”. In: *Nucl. Phys.* B44 (1972), pp. 189–213. DOI: 10.1016/0550-3213(72)90279-9.

[6] Sheldon L. Glashow. “Partial-symmetries of weak interactions”. In: *Nuclear Physics* 22.4 (1961), pp. 579–588. ISSN: 0029-5582. DOI: http://dx.doi.org/10.1016/0029-5582(61)90469-2.

[7] Steven Weinberg. “A Model of Leptons”. In: *Phys. Rev. Lett.* 19 (21 Nov. 1967), pp. 1264–1266. DOI: 10.1103/PhysRevLett.19.1264.

[8] Abdus Salam. “Weak and Electromagnetic Interactions”. In: *Conf. Proc.* C680519 (1968), pp. 367–377.

[9] Peter W. Higgs. “Broken Symmetries and the Masses of Gauge Bosons”. In: *Phys. Rev. Lett.* 13 (16 Oct. 1964), pp. 508–509. DOI: 10.1103/PhysRevLett.13.508.

[10] P.W. Higgs. “Broken symmetries, massless particles and gauge fields”. In: *Physics Letters* 12.2 (1964), pp. 132–133. ISSN: 0031-9163. DOI: 10.1016/0031-9163(64)91136-9.

[11] F. Englert and R. Brout. “Broken Symmetry and the Mass of Gauge Vector Mesons”. In: *Phys. Rev. Lett.* 13 (9 Aug. 1964), pp. 321–323. DOI: 10.1103/PhysRevLett.13.321.

[12] G. S. Guralnik, C. R. Hagen, and T. W. B. Kibble. “Global Conservation Laws and Massless Particles”. In: *Phys. Rev. Lett.* 13 (20 Nov. 1964), pp. 585–587. doi: 10.1103/PhysRevLett.13.585.

[13] T. W. B. Kibble. “Symmetry Breaking in Non-Abelian Gauge Theories”. In: *Phys. Rev.* 155 (5 Mar. 1967), pp. 1554–1561. doi: 10.1103/PhysRev.155.1554.

[14] S. Chatrchyan et al. “Observation of a new boson at a mass of 125 GeV with the CMS experiment at the LHC”. In: *Physics Letters B* 716.1 (Sept. 2012), pp. 30–61. issn: 0370-2693. doi: 10.1016/j.physletb.2012.08.021.

[15] G. Aad et al. “Observation of a new particle in the search for the Standard Model Higgs boson with the ATLAS detector at the LHC”. In: *Physics Letters B* 716.1 (Sept. 2012), pp. 1–29. issn: 0370-2693. doi: 10.1016/j.physletb.2012.08.020.

[16] N. Aghanim et al. “Planck 2018 results”. In: *Astronomy & Astrophysics* 641 (Sept. 2020), A6. issn: 1432-0746. doi: 10.1051/0004-6361/201833910.

[17] Andrei D Sakharov. “Violation ofCPin variance,Casymmetry, and baryon asymmetry of the universe”. In: *Soviet Physics Uspekhi* 34.5 (May 1991), pp. 392–393. doi: 10.1070/pu1991v034n05abeh002497.

[18] K. Kajantie et al. “Is There a Hot Electroweak Phase Transition atmH⊠mW?” In: *Physical Review Letters* 77.14 (Sept. 1996), pp. 2887–2890. issn: 1079-7114. doi: 10.1103/physrevlett.77.2887.

[19] F. Csikor, Z. Fodor, and J. Heitger. “End Point of the Hot Electroweak Phase Transition”. In: *Physical Review Letters* 82.1 (Jan. 1999), pp. 21–24. issn: 1079-7114. doi: 10.1103/physrevlett.82.21.

[20] K. Kajantie, K. Rummukainen, and M. Shaposhnikov. “A lattice Monte Carlo study of the hot electroweak phase transition”. In: *Nuclear Physics B* 407.2 (Oct. 1993), pp. 356–372. issn: 0550-3213. doi: 10.1016/0550-3213(93)90062-t.

[21] K. Kanaya and S. Kaya. “Critical exponents of a three-dimensional O(4) spin model”. In: *Physical Review D* 51.5 (Mar. 1995), pp. 2404–2410. issn: 0556-2821. doi: 10.1103/physrevd.51.2404.

[22] K. Jansen. “Status of the finite temperature electroweak phase transition on the lattice”. In: *Nuclear Physics B - Proceedings Supplements* 47.1-3 (Mar. 1996), pp. 196–211. issn: 0920-5632. doi: 10.1016/0920-5632(96)00045-x.

[23] M. B. GAVELA et al. “STANDARD MODEL CP-VIOLATION AND BARYON ASYMMETRY”. In: *Modern Physics Letters A* 09.09 (Mar. 1994), pp. 795–809. issn: 1793-6632. doi: 10.1142/s0217732394000629.

[24] David E Morrissey and Michael J Ramsey-Musolf. “Electroweak baryogenesis”. In: *New Journal of Physics* 14.12 (Dec. 2012), p. 125003. issn: 1367-2630. doi: 10.1088/1367-2630/14/12/125003.

[25] T Konstandin. “Quantum transport and electroweak baryogenesis”. In: *Physics-Uspekhi* 56.8 (Aug. 2013), pp. 747–771. issn: 1468-4780. doi: 10.3367/ufne.0183.201308a.0785.

[26] Vanda Silveira and A. Zee. “Scalar Phantoms”. In: *Physics Letters B* 161.1 (1985), pp. 136–140. ISSN: 0370-2693. DOI: https://doi.org/10.1016/0370-2693(85)90624-0.

[27] John McDonald. “Gauge singlet scalars as cold dark matter”. In: *Physical Review D* 50.6 (Sept. 1994), pp. 3637–3649. ISSN: 0556-2821. DOI: 10.1103/physrevd.50.3637.

[28] M. C. Bento et al. “Self-interacting dark matter and the Higgs boson”. In: *Physical Review D* 62.4 (July 2000). ISSN: 1089-4918. DOI: 10.1103/physrevd.62.041302.

[29] C.P. Burgess, Maxim Pospelov, and Tonnis ter Veldhuis. “The Minimal Model of nonbaryonic dark matter: a singlet scalar”. In: *Nuclear Physics B* 619.1-3 (Dec. 2001), pp. 709–728. ISSN: 0550-3213. DOI: 10.1016/s0550-3213(01)00513-2.

[30] Hooman Davoudiasl et al. “The new Minimal Standard Model”. In: *Physics Letters B* 609.1-2 (Mar. 2005), pp. 117–123. ISSN: 0370-2693. DOI: 10.1016/j.physletb.2005.01.026.

[31] J.J. van der Bij. “The minimal non-minimal standard model”. In: *Physics Letters B* 636.1 (Apr. 2006), pp. 56–59. ISSN: 0370-2693. DOI: 10.1016/j.physletb.2006.03.018.

[32] Alexander Kusenko. “Sterile Neutrinos, Dark Matter, and Pulsar Velocities in Models with a Higgs Singlet”. In: *Physical Review Letters* 97.24 (Dec. 2006). ISSN: 1079-7114. DOI: 10.1103/physrevlett.97.241301.

[33] Xiao-Gang He et al. “Constraints on scalar dark matter from direct experimental searches”. In: *Physical Review D* 79.2 (Jan. 2009). ISSN: 1550-2368. DOI: 10.1103/physrevd.79.023521.

[34] Matthew Gonderinger et al. “Vacuum stability, perturbativity, and scalar singlet dark matter”. In: *Journal of High Energy Physics* 2010.1 (Jan. 2010). ISSN: 1029-8479. DOI: 10.1007/jhep01(2010)053.

[35] Yann Mambrini. “Higgs searches and singlet scalar dark matter: Combined constraints from XENON 100 and the LHC”. In: *Physical Review D* 84.11 (Dec. 2011). ISSN: 1550-2368. DOI: 10.1103/physrevd.84.115017.

[36] Xiao-Gang He, Bo Ren, and Jusak Tandean. “Hints of standard model Higgs boson at the LHC and light dark matter searches”. In: *Physical Review D* 85.9 (May 2012). ISSN: 1550-2368. DOI: 10.1103/physrevd.85.093019.

[37] Rita Coimbra, Marco O. P. Sampaio, and Rui Santos. “ScannerS: constraining the phase diagram of a complex scalar singlet at the LHC”. In: *The European Physical Journal C* 73.5 (May 2013). ISSN: 1434-6052. DOI: 10.1140/epjc/s10052-013-2428-4.

[38] Raul Costa et al. “Two-loop stability of a complex singlet extended standard model”. In: *Physical Review D* 92.2 (July 2015). ISSN: 1550-2368. DOI: 10.1103/physrevd.92.025024.

[39] Raul Costa et al. “Singlet extensions of the standard model at LHC Run 2: benchmarks and comparison with the NMSSM”. In: *Journal of High Energy Physics* 2016.6 (June 2016). ISSN: 1029-8479. DOI: 10.1007/jhep06(2016)034.

[40] "Combination of searches for invisible Higgs boson decays with the ATLAS experiment". In: *ATLAS-CONF-2020-052* (Oct. 2020).

[41] Andrea Dainese et al., eds. *Report on the Physics at the HL-LHC,and Perspectives for the HE-LHC*. Vol. 7/2019. CERN Yellow Reports: Monographs. Geneva, Switzerland: CERN, 2019. ISBN: 978-92-9083-549-3. DOI: 10.23731/CYRM-2019-007.

[42] Michael E. Peskin and Daniel V. Schroeder. *An Introduction to quantum field theory*. Advanced book program. Westview Press Reading (Mass.), 1995. ISBN: 9780201503975, 0201503972.

[43] JORGE C. ROMÃO and JOÃO P. SILVA. "A RESOURCE FOR SIGNS AND FEYNMAN DIAGRAMS OF THE STANDARD MODEL". In: *International Journal of Modern Physics A* 27.26 (Oct. 2012), p. 1230025. ISSN: 1793-656X. DOI: 10.1142/s0217751x12300256.

[44] Margarete Mühlleitner et al. *ScannerS: Parameter Scans in Extended Scalar Sectors*. 2020. arXiv: 2007.02985 [hep-ph].

[45] Kristjan Kannike. "Vacuum stability conditions from copositivity criteria". In: *The European Physical Journal C* 72.7 (July 2012). ISSN: 1434-6052. DOI: 10.1140/epjc/s10052-012-2093-z.

[46] John F. Gunion et al. "The Higgs Hunter's Guide". In: *Front. Phys.* 80 (2000), pp. 1–448.

[47] J. F. Gunion, H. E. Haber, and J. Wudka. "Sum rules for Higgs bosons". In: *Phys. Rev. D* 43 (3 Feb. 1991), pp. 904–912. DOI: 10.1103/PhysRevD.43.904.

[48] Benjamin W. Lee, C. Quigg, and H. B. Thacker. "Weak interactions at very high energies: The role of the Higgs-boson mass". In: *Phys. Rev. D* 16 (5 Sept. 1977), pp. 1519–1531. DOI: 10.1103/PhysRevD.16.1519.

[49] Wolfgang G. Hollik, Georg Weiglein, and Jonas Wittbrodt. "Impact of vacuum stability constraints on the phenomenology of supersymmetric models". In: *Journal of High Energy Physics* 2019.3 (Mar. 2019). ISSN: 1029-8479. DOI: 10.1007/jhep03(2019)109.

[50] K. A. Olive et al. "Review of Particle Physics". In: *Chin. Phys.* C38 (2014), p. 090001. DOI: 10.1088/1674-1137/38/9/090001.

[51] D.A. Ross and M. Veltman. "Neutral currents and the Higgs mechanism". In: *Nuclear Physics B* 95.1 (1975), pp. 135–147. ISSN: 0550-3213. DOI: http://dx.doi.org/10.1016/0550-3213(75)90485-X.

[52] Daniele Pedrini. "Search for the flavour-changing neutral current decay $D^0 \longrightarrow \mu^+\mu^-$ in pp collisions at $\sqrt{s} = 7$ TeV with CMS". In: *Proceedings, 5th International Workshop on Charm Physics (Charm 2012)*. 2012. arXiv: 1208.5908 [hep-ex].

[53] Efe Yazgan. "Flavor changing neutral currents in top quark production and decay". In: *6th International Workshop on Top Quark Physics (TOP2013) Durbach, Germany, September 14-19, 2013*. 2014, pp. 285–294. DOI: 10.3204/DESY-PROC-2014-02/34. arXiv: 1312.5435 [hep-ex].

[54] S. L. Glashow, J. Iliopoulos, and L. Maiani. “Weak Interactions with Lepton-Hadron Symmetry”. In: *Phys. Rev. D* 2 (7 Oct. 1970), pp. 1285–1292. DOI: 10.1103/PhysRevD.2.1285.

[55] Michael E. Peskin and Tatsu Takeuchi. “Estimation of oblique electroweak corrections”. In: *Phys. Rev. D* 46 (1 July 1992), pp. 381–409. DOI: 10.1103/PhysRevD.46.381.

[56] Ivan Maksymyk, C. P. Burgess, and David London. “BeyondS,T, andU”. In: *Physical Review D* 50.1 (July 1994), pp. 529–535. ISSN: 0556-2821. DOI: 10.1103/physrevd.50.529.

[57] P. Bechtle et al. “HiggsBounds: Confronting arbitrary Higgs sectors with exclusion bounds from LEP and the Tevatron”. In: *Computer Physics Communications* 181.1 (2010), pp. 138–167. ISSN: 0010-4655. DOI: 10.1016/j.cpc.2009.09.003.

[58] P. Bechtle et al. “HiggsBounds 2.0.0: Confronting neutral and charged Higgs sector predictions with exclusion bounds from LEP and the Tevatron”. In: *Computer Physics Communications* 182.12 (Dec. 2011), pp. 2605–2631. ISSN: 0010-4655. DOI: 10.1016/j.cpc.2011.07.015.

[59] Philip Bechtle et al. “HiggsBounds-4: improved tests of extended Higgs sectors against exclusion bounds from LEP, the Tevatron and the LHC”. In: *The European Physical Journal C* 74.3 (Mar. 2014). ISSN: 1434-6052. DOI: 10.1140/epjc/s10052-013-2693-2.

[60] Philip Bechtle et al. “Applying exclusion likelihoods from LHC searches to extended Higgs sectors”. In: *The European Physical Journal C* 75.9 (Sept. 2015). ISSN: 1434-6052. DOI: 10.1140/epjc/s10052-015-3650-z.

[61] Philip Bechtle et al. “HiggsBounds-5: testing Higgs sectors in the LHC 13 TeV Era”. In: *The European Physical Journal C* 80.12 (Dec. 2020). ISSN: 1434-6052. DOI: 10.1140/epjc/s10052-020-08557-9.

[62] Philip Bechtle et al. “HiggsSignals: Confronting arbitrary Higgs sectors with measurements at the Tevatron and the LHC”. In: *The European Physical Journal C* 74.2 (Feb. 2014). ISSN: 1434-6052. DOI: 10.1140/epjc/s10052-013-2711-4.

[63] Philip Bechtle et al. “HiggsSignals-2: probing new physics with precision Higgs measurements in the LHC 13 TeV era”. In: *The European Physical Journal C* 81.2 (Feb. 2021). ISSN: 1434-6052. DOI: 10.1140/epjc/s10052-021-08942-y.

[64] G. Bélanger et al. “micrOMEGAs 2.0: A program to calculate the relic density of dark matter in a generic model”. In: *Computer Physics Communications* 176.5 (Mar. 2007), pp. 367–382. ISSN: 0010-4655. DOI: 10.1016/j.cpc.2006.11.008.

[65] G. Bélanger et al. “Indirect search for dark matter with micrOMEGAs_2.4”. In: *Computer Physics Communications* 182.3 (Mar. 2011), pp. 842–856. ISSN: 0010-4655. DOI: 10.1016/j.cpc.2010.11.033.

[66] G. Bélanger, A. Mjallal, and A. Pukhov. "Recasting direct detection limits within micrOMEGAs and implication for non-standard dark matter scenarios". In: *The European Physical Journal C* 81.3 (Mar. 2021). ISSN: 1434-6052. DOI: 10.1140/epjc/s10052-021-09012-z.

[67] E. Aprile et al. "Dark Matter Search Results from a One Ton-Year Exposure of XENON1T". In: *Phys. Rev. Lett.* 121 (11 Sept. 2018), p. 111302. DOI: 10.1103/PhysRevLett.121.111302.

[68] Marcel Krause. "On the Renormalization of the Two-Higgs-Doublet Model". In: (May 2016).

[69] Joshua P. Ellis. "Ti k Z-Feynman: Feynman diagrams with Ti k Z". In: *Computer Physics Communications* 210 (Jan. 2017), pp. 103–123. ISSN: 0010-4655. DOI: 10.1016/j.cpc.2016.08.019.

[70] A. Denner and S. Dittmaier. "The complex-mass scheme for perturbative calculations with unstable particles". In: *Nuclear Physics B - Proceedings Supplements* 160 (Oct. 2006), pp. 22–26. ISSN: 0920-5632. DOI: 10.1016/j.nuclphysbps.2006.09.025.

[71] Ansgar Denner. *Techniques for the calculation of electroweak radiative corrections at the one-loop level and results for W-physics at LEP200.* 2007. arXiv: 0709.1075 [hep-ph].

[72] J. Fleischer and F. Jegerlehner. "Radiative corrections to Higgs-boson decays in the Weinberg-Salam model". In: *Phys. Rev. D* 23 (9 May 1981), pp. 2001–2026. DOI: 10.1103/PhysRevD.23.2001.

[73] Marcel Krause et al. "Gauge-independent renormalization of the 2-Higgs-doublet model". In: *Journal of High Energy Physics* 2016.9 (Sept. 2016). ISSN: 1029-8479. DOI: 10.1007/jhep09(2016)143.

[74] Marcel Krause et al. "Gauge-independent renormalization of the N2HDM". In: *Journal of High Energy Physics* 2017.12 (Dec. 2017). ISSN: 1029-8479. DOI: 10.1007/jhep12(2017)077.

[75] Shinya Kanemura et al. "Higgs coupling constants as a probe of new physics". In: *Physical Review D* 70.11 (Dec. 2004). ISSN: 1550-2368. DOI: 10.1103/physrevd.70.115002.

[76] John M. Cornwall and Joannis Papavassiliou. "Gauge Invariant Three Gluon Vertex in QCD". In: *Phys. Rev.* D40 (1989), p. 3474. DOI: 10.1103/PhysRevD.40.3474.

[77] Joannis Papavassiliou. "Gauge Invariant Proper Selfenergies and Vertices in Gauge Theories with Broken Symmetry". In: *Phys. Rev.* D41 (1990), p. 3179. DOI: 10.1103/PhysRevD.41.3179.

[78] Giuseppe Degrassi and Alberto Sirlin. "Gauge-invariant self-energies and vertex parts of the standard model in the pinch technique framework". In: *Phys. Rev. D* 46 (7 Oct. 1992), pp. 3104–3116. DOI: 10.1103/PhysRevD.46.3104.

[79] Joannis Papavassiliou. "Gauge independent transverse and longitudinal self-energies and vertices via the pinch technique". In: *Phys. Rev.* D50 (1994), pp. 5958–5970. DOI: 10.1103/PhysRevD.50.5958. arXiv: hep-ph/9406258 [hep-ph].

[80] Daniele Binosi and Joannis Papavassiliou. "Pinch technique: Theory and applications". In: *Physics Reports* 479.1-6 (Aug. 2009), pp. 1–152. ISSN: 0370-1573. DOI: 10.1016/j.physrep.2009.05.001.

[81] Duarte Azevedo et al. *One-loop Corrections to the Higgs Boson Invisible Decay in the Dark Doublet Phase of the N2HDM*. 2021. arXiv: 2104.03184 [hep-ph].

[82] Florian Staub. "From superpotential to model files for FeynArts and CalcHep/CompHep". In: *Computer Physics Communications* 181.6 (June 2010), pp. 1077–1086. ISSN: 0010-4655. DOI: 10.1016/j.cpc.2010.01.011.

[83] Florian Staub. "SARAH 3.2: Dirac gauginos, UFO output, and more". In: *Computer Physics Communications* 184.7 (July 2013), pp. 1792–1809. ISSN: 0010-4655. DOI: 10.1016/j.cpc.2013.02.019.

[84] Florian Staub. "SARAH 4: A tool for (not only SUSY) model builders". In: *Computer Physics Communications* 185.6 (June 2014), pp. 1773–1790. ISSN: 0010-4655. DOI: 10.1016/j.cpc.2014.02.018.

[85] Florian Staub. "Exploring New Models in All Detail withSARAH". In: *Advances in High Energy Physics* 2015 (2015), pp. 1–126. ISSN: 1687-7365. DOI: 10.1155/2015/840780.

[86] Thomas Hahn. "Generating Feynman diagrams and amplitudes with FeynArts 3". In: *Computer Physics Communications* 140.3 (2001), pp. 418–431. ISSN: 0010-4655. DOI: https://doi.org/10.1016/S0010-4655(01)00290-9.

[87] R. Mertig, M. Böhm, and A. Denner. "Feyn Calc - Computer-algebraic calculation of Feynman amplitudes". In: *Computer Physics Communications* 64.3 (1991), pp. 345–359. ISSN: 0010-4655. DOI: https://doi.org/10.1016/0010-4655(91)90130-D.

[88] Vladyslav Shtabovenko, Rolf Mertig, and Frederik Orellana. "New developments in FeynCalc 9.0". In: *Computer Physics Communications* 207 (Oct. 2016), pp. 432–444. ISSN: 0010-4655. DOI: 10.1016/j.cpc.2016.06.008.

[89] Vladyslav Shtabovenko, Rolf Mertig, and Frederik Orellana. "FeynCalc 9.3: New features and improvements". In: *Computer Physics Communications* 256 (Nov. 2020), p. 107478. ISSN: 0010-4655. DOI: 10.1016/j.cpc.2020.107478.

[90] G. 't Hooft and M. Veltman. "Scalar one-loop integrals". In: *Nuclear Physics B* 153 (1979), pp. 365–401. ISSN: 0550-3213. DOI: 10.1016/0550-3213(79)90605-9.

[91] T. Hahn and M. Pérez-Victoria. "Automated one-loop calculations in four and D dimensions". In: *Computer Physics Communications* 118.2 (1999), pp. 153–165. ISSN: 0010-4655. DOI: https://doi.org/10.1016/S0010-4655(98)00173-8.

[92] Philipp Basler and Margarete Mühlleitner. "BSMPT (Beyond the Standard Model Phase Transitions): A tool for the electroweak phase transition in extended Higgs sectors". In: *Computer Physics Communications* 237 (Apr. 2019), pp. 62–85. ISSN: 0010-4655. DOI: 10.1016/j.cpc.2018.11.006.

[93] Philipp Basler, Margarete Mühlleitner, and Jonas Müller. "BSMPT v2 a tool for the electroweak phase transition and the baryon asymmetry of the universe in extended Higgs Sectors". In: *Computer Physics Communications* 269 (Dec. 2021), p. 108124. ISSN: 0010-4655. DOI: 10.1016/j.cpc.2021.108124.

[94] A. Zee. *Quantum Field Theory in a Nutshell: (Second Edition).* In a Nutshell. Princeton University Press, 2010. ISBN: 9781400835324.

[95] G. Källén. *Elementary Particle Physics.* Massachusetts: Addison-Wesley, 1964.

[96] P.A. Zyla et al. "Review of Particle Physics". In: *PTEP* 2020.8 (2020), p. 083C01. DOI: 10.1093/ptep/ptaa104.

[97] Martin Bauer and Tilman Plehn. *Yet Another Introduction to Dark Matter.* 2018. arXiv: 1705.01987 [hep-ph].

[98] A. Djouadi, J. Kalinowski, and M. Spira. "HDECAY: a program for Higgs boson decays in the Standard Model and its supersymmetric extension". In: *Computer Physics Communications* 108.1 (Jan. 1998), pp. 56–74. ISSN: 0010-4655. DOI: 10.1016/s0010-4655(97)00123-9.

[99] Abdelhak Djouadi et al. "HDECAY: Twenty++ years after". In: *Computer Physics Communications* 238 (May 2019), pp. 214–231. ISSN: 0010-4655. DOI: 10.1016/j.cpc.2018.12.010.

[100] Marcel Krause and Margarete Mühlleitner. "Impact of electroweak corrections on neutral Higgs boson decays in extended Higgs sectors". In: *Journal of High Energy Physics* 2020.4 (Apr. 2020). ISSN: 1029-8479. DOI: 10.1007/jhep04(2020)083.

[101] Ruth Britto and Edoardo Mirabella. "External leg corrections in the unitarity method". In: *Journal of High Energy Physics* 2012.1 (Jan. 2012). ISSN: 1029-8479. DOI: 10.1007/jhep01(2012)045.